Experimental and Theoretical Studies on Size-Dependent Optical Responses of Free Silver Cluster Cations: Geometry Evolution and Emergence of Collective Excitation of Electrons

河野, 聖

Doctoral Dissertation

Experimental and Theoretical Studies on Size-Dependent Optical Responses of Free Silver Cluster Cations: Geometry Evolution and Emergence of Collective Excitation of Electrons

Satoshi Kono

Graduate School of Science

Kyushu University

2024

Abstract

Photoabsorption of size-selected free silver cluster cations, Ag_N^+ (N = 2–92), is studied by photodissociation action spectroscopy (PDS) and photoabsorption spectroscopy by means of a cavity ring-down technique (CRDS) in a spectral range of 2.8–5.0 eV. Emergence of collective excitation of electrons is discussed along with geometric structures in the course of cluster growth toward nanoparticles. Theoretical analysis on the photoabsorption was also carried out. To generate a wide range of cluster sizes, the cluster-growth process in a magnetron-sputtering cluster-ion source is first examined by optical emission spectroscopy characterizing the magnetron plasma as well as mass spectrometry. It is suggested that rarefaction of the sputtered atoms leads to smaller clusters, which implies that larger clusters are formed by reducing kinetic energies of sputtered atoms. Ag_N^+ thus generated are interrogated by PDS. Multiple-modal profiles are observed for $N \leq 14$. On the other hand, $N \geq 19$ show single-/double-band profiles in a specific energy range, which reflects their spherical/spheroidal structures. Such a change in geometric structures of Ag_N^+ is systematically examined. Photoabsorption cross sections measured by CRDS characterize oscillator strengths quantitatively. Theoretically, the effective number of electrons contributing to the excitation is estimated to be 40–50% of 5s electrons at larger sizes. To summarize these experimental/theorical considerations, the author concludes the collective excitation of electrons emerges above N = 19 in Ag_N^+. The present study reveals emergence of collective excitation of electrons in Ag_N^+ as the cluster changes its geometry during growth into the nanoparticle regime. The author believes that the present methodologies, including PDS, CRDS, and theoretical evaluation of collectivity indices, open the door to investigation of the essence of electronic excitations in metal clusters.

Table of Contents

1. General Introduction

1.1. Photoabsorption of metal nanoparticles

Metal nanoparticles are known to exhibit characteristic optical properties different from the bulk. Historically, human beings have utilized metal nanoparticles or colloids as color formers of, e.g., the Roman Lycurgus Cup and stained glasses [1–3] without understanding what actually exhibits the colors. Faraday's report in 1857 made a great step to understanding the phenomenon [4]; he revealed that the colloidal gold exhibits a ruby tint. It was subsequently shown that the origin of the optical absorption that gives these characteristic colors is the collective motion of electrons in the metallic colloids/nanoparticles. Many researchers have been investigating this phenomenon called plasmonic excitation or collective excitation of electrons, which attracts much attention today because of potential use in various applications such as optical sensing, energy harvesting, etc. [5]. In 1908, Mie established a theoretical framework describing photoabsorption of a small particle based on the classical electrodynamics [6], which predicts that the resonance energy is not size-dependent for particles much smaller than the wavelength of incident light. However, Charlé et al. reported a blue shift of the resonance as a diameter of a silver nanoparticle decreased below 10 nm in 1989 [7]. Scholl et al. also interrogated silver nanoparticles on carbon films by electron energy loss spectroscopy employing a scanning transmission electron microscope (STEM EELS) [8]; a blue shift of the plasmon peak was observed as the diameter of the nanoparticle decreased from 20 nm to less than two nanometers. They revealed the size-dependence of the plasmon energy and the significance of the quantum effect in the smaller silver nanoparticles by the experiments in combination with theoretical calculations: the nanoparticle was modeled by a dielectric material of which permittivity explicitly

involved transitions between energy levels of valence electrons.

1.2. History of spectroscopic studies on metal clusters

In contrast to the case of metal nanoparticles, it is not obvious whether metal particles show the collective excitation of electrons in the sub-nanometer scale. In this context, metal clusters, aggregates of several to several hundreds of metal atoms, have been investigated as intermediates between metal atoms and nanoparticles. Such a bottom-up approach in cluster science, in contrast to the top-down approach from bulk metal to nanoparticles, is necessary to elucidate the optical property and establish a theoretical framework describing the photoabsorption in the intermediate regime as a function of cluster size, N, i.e., the number of constituent atoms in a cluster.

Early work on photoabsorption of metal clusters was limited to smaller sizes, e.g., $Ag_{1–6}$ [9], Mn_2 [10], Fe_2 [10], $Ni_{1–3}$ [10, 11], Pb_2 [12], Mg_2 [13], Pt_2 [14], $Cr_{1–3}$ [15, 16], V_2 [17], $Mo_{1–3}$ [16], Na_3 [18–21], $Cu_{1–4}$ [22, 23], and $Li_{1–8}$ [24, 25]. Among them, for example, spectroscopic studies such as resonant two-photon ionization spectroscopy, on neutral lithium clusters were performed by Wöste's group [25]: rich transitions in the absorption spectrum of Li_4 were interpreted as molecular-type excitations, i.e., not collective.

Surprising reports were presented by Knight's group in 1987 and later [26–29]; they performed photodissociation spectroscopy on neutral sodium clusters with the sizes up to 40, where a cluster beam with multiple sizes was irradiated for dissociation, ionized and size-selected. Observed absorption bands accounted for ~60% of the oscillator strengths originating from valence electrons at N = 10. Especially, for N = 6–12, the photodissociation spectra were well explained by geometries of the clusters estimated by

an ellipsoidal-shell model [28]; collective motions of electrons along the three axes of an ellipsoidal cluster correspond to the resonance frequencies, which depend on the axis lengths. Because these features were in contrast to those of smaller clusters such as the trimer and the tetramer showing multiple narrow bands reminiscent of molecular photoabsorption spectra, they concluded that collective excitation of electrons emerges in neutral sodium clusters at $N = 3$–5. Emergence of collective (or plasmonic) behavior of electrons even in such small sizes is remarkable, as it is generally observed in nanoparticles. The reports from Knight's group have stimulated studies on collective excitation of electrons for various metal clusters, e.g., neutral sodium clusters [30–33], sodium cluster cations [34–36], potassium cluster cations [37], copper cluster cations [38], and neutral cesium clusters [39]. However, if one wishes to utilize the collective excitation of electrons in the cluster regime for various applications, alkaline metal clusters are not suitable for materials [5].

"Collective excitations of electrons" in silver cluster cations, Ag_N^+, and anions, Ag_N^-, were firstly reported by Tiggesbäumker et al. [40–44], where the discussion was in line with that presented on sodium clusters by Knight's group [26–29]. Ag_9^+ and Ag_{21}^+ showed intense single bands which carry 94% and 64% of oscillator strengths of valence electrons, respectively, in their photodissociation spectra. Moreover, the spectral profiles were explained by the ellipsoidal-shell model [28]. From a point of view of applications of the collective excitation, silver is advantageous compared with other elements. It is chemically more stable than alkaline metals. Moreover, silver clusters show more intense light absorption than other coinage-metal clusters, i.e., gold and copper [45–48]. Therefore, silver clusters have been attracting a great deal of interests from many researchers [5, 47–79] as shown in Table 1.1. Among the previous research,

Rayner et al. performed photodissociation spectroscopy employing a messenger-tagging technique [50, 51]; structured absorption bands were reported for Ag_9Kr^+, which was in contrast to a structureless profile of Ag_9^+ obtained by Tiggesbäumker et al. Photodissociation spectra of Ag_9^+ similar to Rayner et al.'s result were also reported by Ito [52] ,Terasaki et al. [53], and Lindinger et al. [47]. On the other hand, a series of systematic photoabsorption studies on size-selected neutral silver clusters, Ag_N (N = 1–120), in rare-gas metrices were performed by Harbich's group [49, 57–60], where a change in spectral profiles, i.e., from highly structured to a single broad band, was observed. However, they supposed that the single band was due to plasmon without any quantitative analysis. Aikens et al. carried out simulation of absorption spectra of neutral silver clusters with the sizes of 10, 20, 35, 56, 84, and 120 by assuming tetrahedral structures for all the sizes [64]. They mentioned that the predicted intense band at N = 20 is collective because the band originates from a sp ← sp intraband transition in analogy to plasmon. Shibuta et al. reported that Ag_N supported on C_{60} showed collective excitations of electrons above N = 9 in their time-resolved two-photon photoemission spectroscopy [79]; photoemission intensity upon laser irradiation was examined as a function of polarization direction of the laser, where the intensity increased from N = 3 to 9 and was leveled off at N = 9 and above. Shibuta et al.'s result is inconsistent with those in Rayner et al.'s report mentioned above. Campos et al. [80] performed STEM EELS on silver clusters embedded in silica. No signal originating from the plasmonic excitation was observed at the beginning of their experiments; the signal emerged and shifted by removing oxidized surface layers and the surrounding medium upon continuous electron irradiation. This result implies that photoabsorption of silver clusters is easily affected by surrounding media.

Table 1.1. Major studies on photoabsorption of silver clusters. The literatures are classified by the form of sample clusters (either gas phase, embedded or supported) for experiments and theoretical studies.

Year	Gas phase	Embedded/supported	Theory
1990s	$Ag_{9–21,\sim50,\sim70}^{+}$ [40, 42–44], $Ag_{5–19}^{-}$ [41, 42], Ag_9^{+} [47], $Ag_{4–12}^{0/+}Kr_{1–3}$ [50, 51], Ag_4^{+} [55]	$Ag_{2–39}$/Ar [58–60], $Ag_{7,21}$/Ar,Kr,Xe [59]	$Ag_{2–4}^{0/+}$ [66, 67], $Ag_{19–59}^{+/-}$ [76]
2000s	Ag_9^{+} [53]	$Ag_{4–22}$/Ar [68]	$Ag_{2–12}$ [75], $[Ag_{25}(SH)_{18}]^{-}$ [81]
2010s	$Ag_{8–14}^{+}$ [52], Ag_2^{+} [54]	$Ag_{5–11}$/Ar [49], $Ag_{1–120}$/Ne [57], $Ag_{20,55}$/BK7 [62], $Ag_{\sim37}$/BK7 [63], $Ag_{9–55}$/BK7 [84],	$Ag_{10–120}$ [5, 64], $Ag_{3–87}^{+}$ and Ag_{71}^{3-} [5, 65], Ag_8 [48], Ag_{20}, $Ag_{55}^{+/3-}$ [69], Ag_{20}/Ne,Ar,Kr,Xe [70], $Ag_{2–92}$, Ag_{147}^{+} [71–74], $Ag_{6–85}^{5+–5-}$ [82], Ag_{55} [83]
2020s	$Ag_{3–19}^{-}$ [56], Ag_{91}^{-} [61]	$Ag_{3–55}/C_{60}$ [79]	

1.3. Problems in the previous cluster studies

Although the photoabsorption of silver clusters has been investigated by many researchers as mentioned in Section 1.2, whether it is collective or not is still in debate because of two reasons: (a) embedded or supported clusters have been mainly investigated especially for larger clusters; surrounding media probably perturb the photoabsorption of the cluster [80], which makes it difficult to interpret the experimental data. To simplify the situation by removing the perturbations, investigation on the intrinsic optical property of *free* silver clusters is demanded. (b) The emergence of the collective excitation has been discussed only qualitatively in the previous studies. The author would like to emphasize that two pieces of evidence are necessary to prove emergence of the collective excitation by referring to Reference [78]: (1) concentration of oscillator strengths: intense absorption such as collective excitation should be characterized by a high density of oscillator strengths in a specific spectral region, because all the molecules show total oscillator strengths equal to the number of electrons over the entire photon-energy range based on the Thomas–Reiche–Kuhn sum rule (Figure 1.1). (2) Theoretical evaluation of the collectivity, i.e., contribution of multiple individual transitions; the contribution of the individual transitions in silver clusters has also been discussed only qualitatively by employing model structures [5, 65]. To discuss the collectivity in electronic excitations, a theoretical method of the quantitative collectivity is necessary. Moreover, we must measure absolute absorption cross sections experimentally to ensure the theoretical results in addition to tracing the concentration of oscillator strengths as a function of cluster size. However, there is no experimental study that evaluated photoabsorption spectra and oscillator strengths of size-selected free silver clusters quantitatively.

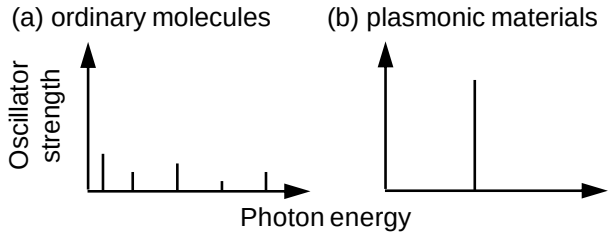

Figure 1.1. Illustration of concentration of oscillator strengths. (a) Ordinary molecules. (b) Plasmonic materials.

1.4. Objective of the present study

The background described in Section 1.3 motivated the author to investigate geometric structures and electronic excitations of size-selected free silver cluster cations, Ag_N^+, via their photoabsorption in a broad size range from the dimer ($N = 2$) toward the nanoparticle regime as large as $N = 92$. Specific focus is placed on their geometry evolution in the course of cluster growth and on emergence of collective excitation of electrons as a function of cluster size.

Prior to optical studies, a method for cluster formation in a broad size range, especially in large sizes, is established with the aid of analysis of cluster-growth processes employing optical emission spectroscopy. Based on this technique for cluster generation, photodissociation action spectroscopy is performed on size-selected free silver cluster cations. The author intends to extract information about size-dependent evolution in geometric structures of the clusters from spectral profiles measured by the photodissociation experiment. On the other hand, the spectral profile may be reflective of collective excitation modes. However, multi-photon dissociation processes would dominate in large cluster sizes, as discussed in detail in Chapter 4, a novel technique is required to obtain one-photon absorption cross sections without relying on the action spectroscopy of photodissociation, which is the key to quantitative characterization for

collectivity of electronic excitations.

To tackle this challenging issue, the author employs cavity ring-down spectroscopy [85], which enables *direct* measurement of absorption cross sections with extremely high sensitivity, in combination with a linear ion trap to prepare a high-density sample of size-selected cluster ions. In this manner, quantitative evaluation of oscillator strengths of photoabsorption will be accomplished for specific sizes up to $N = 92$.

To support these experimental results, theoretical studies are performed to evaluate collectivity of electronic excitation as well as to obtain geometric structures and optical excitation spectra. Density-functional and linear-response density-functional theories are employed for structure optimization and for simulating absorption spectra, respectively. A collectivity index, representing the number of effective excitations [78], is evaluated for discussion of collective behaviors of electronic excitation. In addition, a concept of an ideal plasmon state [86] is introduced to analyze the excited states.

The present thesis is organized as follows. An overview of the experimental setup is described in Chapter 2. Analysis on cluster-growth processes investigated by optical emission spectroscopy as well as mass spectrometry is presented in Chapter 3. Photodissociation action spectroscopy on silver cluster cations are described in Chapter 4, where size-dependence of geometric structures are investigated based on the spectral profiles of photodissociation. In Chapter 5, presented are photoabsorption spectra measured in a direct manner by employing cavity ring-down optical absorption spectroscopy, which enables us to evaluate oscillator strengths quantitatively. Chapter 6 presents theoretical investigation on the collectivity in the electronic excitations. Finally, concluding remarks are given in Chapter 7.

References

[1] I. Freestone, N. Meeks, M. Sax, C. Higgitt, *Gold Bull.* **2007**, *40*, 270.

[2] R. Antoine, M. Broyer, P. Dugourd, *Sci. Technol. Adv. Mater.* **2023**, *24*, 2222546.

[3] U. Kreibig, M. Vollmer, *Optical Properties of Metal Clusters*, Springer, Berlin, New York, **1995**, p. 275.

[4] M. Faraday, *Philos. Trans. R. Soc. Lond.* **1857**, *147*, 145.

[5] E. B. Guidez, C. M. Aikens, *Nanoscale* **2014**, *6*, 11512.

[6] G. Mie, *Ann. Phys.* **1908**, *25*, 377.

[7] K. P. Charlé, W. Schulze, B. Winter, *Z. Phys. D* **1989**, *12*, 471.

[8] J. A. Scholl, A. L. Koh, J. A. Dionne, *Nature* **2012**, *483*, 421.

[9] W. Schulze, H. U. Becker, H. Abe, *Chem. Phys.* **1978**, *35*, 177.

[10] T. C. De Vore, A. Ewing, H. F. Franzen, V. Calder, *Chem. Phys. Lett.* **1975**, *35*, 78.

[11] M. Moskovits, J. E. Hulse, *J. Chem. Phys.* **1977**, *66*, 3988.

[12] L. Brewer, C.-A. Chang, *J. Chem. Phys.* **1972**, *56*, 1728.

[13] L. B. Knight, M. A. Ebener, *J. Mol. Spectrosc.* **1976**, *61*, 412.

[14] K. Jansson, R. Scullman, *J. Mol. Spectrosc.* **1976**, *61*, 299.

[15] E. P. Kündig, M. Moskovits, G. A. Ozin, *Nature* **1975**, *254*, 503.

[16] W. E. Klotzbuecher, G. A. Ozin, *J. Am. Chem. Soc.* **1978**, *100*, 2262.

[17] T. A. Ford, H. Huber, W. Klotzbücher, E. P. Kündig, M. Moskovits, G. A. Ozin, *J. Chem. Phys.* **1977**, *66*, 524.

[18] M. Broyer, G. Delacrétaz, P. Labastie, R. L. Whetten, J. P. Wolf, L. Wöste, *Z. Phys. D* **1986**, *3*, 131.

[19] A. Hermann, M. Hoffmann, S. Leutwyler, E. Schumacher, L. Wöste, *Chem. Phys. Lett.* **1979**, *62*, 216.

[20] G. Delacrétaz, L. Wöste, *Surf. Sci.* **1985**, *156*, 770.

[21] M. Broyer, G. Delacrétaz, P. Labastie, J. P. Wolf, L. Wöste, *Phys. Rev. Lett.* **1986**, *57*, 1851.

[22] M. Moskovits, J. E. Hulse, *J. Chem. Phys.* **1977**, *67*, 4271.

[23] M. D. Morse, J. B. Hopkins, P. R. R. Langridge-Smith, R. E. Smalley, *J. Chem. Phys.* **1983**, *79*, 5316.

[24] L. Andrews, G. C. Pimentel, *J. Chem. Phys.* **1967**, *47*, 2905.

[25] J. Blanc, M. Broyer, J. Chevaleyre, P. Dugourd, H. Kühling, P. Labastie, M. Ulbricht, J. P. Wolf, L. Wöste, *Z. Phys. D* **1991**, *19*, 7.

[26] W. A. de Heer, K. Selby, V. Kresin, J. Masui, M. Vollmer, A. Châtelain, W. D. Knight, *Phys. Rev. Lett.* **1987**, *59*, 1805.

[27] K. Selby, V. Kresin, J. Masui, M. Volmer, W. A. de Heer, A. Scheidemann, W. D. Knight, *Phys. Rev. B* **1991**, *43*, 4565.

[28] K. Selby, M. Vollmer, J. Masui, V. Kresin, W. A. de Heer, W. D. Knight, *Phys. Rev. B* **1989**, *40*, 5417.

[29] K. Selby, M. Vollmer, J. Masui, V. Kresin, W. A. de Heer, W. D. Knight, *Z. Phys. D* **1989**, *12*, 477.

[30] C. R. C. Wang, S. Pollack, M. M. Kappes, *Chem. Phys. Lett.* **1990**, *166*, 26.

[31] S. Pollack, C. R. C. Wang, M. M. Kappes, *J. Chem. Phys.* **1991**, *94*, 2496.

[32] C. R. C. Wang, S. Pollack, D. Cameron, M. M. Kappes, *J. Chem. Phys.* **1990**, *93*, 3787.

[33] C. Yannouleas, R. A. Broglia, *Phys. Rev. A* **1991**, *44*, 5793.

[34] C. Bréchignac, P. Cahuzac, F. Carlier, M. de Frutos, J. Leygnier, *Chem. Phys. Lett.* **1992**, *189*, 28.

[35] M. Schmidt, H. Haberland, *Eur. Phys. J. D* **1999**, *6*, 109.

[36] C. Ellert, M. Schmidt, C. Schmitt, T. Reiners, H. Haberland, *Phys. Chem. Lett.* **1995**, *75*, 1731.

[37] C. Bréchignac, P. Cahuzac, F. Carlier, J. Leygnier, *Chem .Phys. Lett.* **1989**, *164*, 433.

[38] M. F. Jarrold, K. M. Creegan, *Chem. Phys. Lett.* **1990**, *166*, 116.

[39] H. Fallgren, T. P. Martin, *Chem. Phys. Lett.* **1990**, *168*, 233.

[40] J. Tiggesbäumker, L. Köller, H. O. Lutz, K. H. Meiwes-Broer, *Chem. Phys. Lett.* **1992**, *190*, 42.

[41] J. Tiggesbäumker, L. Köller, K. H. Meiwes-Broer, *Chem. Phys. Lett.* **1996**, *260*, 428.

[42] J. Tiggesbäumker, L. Köller, H. O. Lutz, K. H. Meiwes-Broer in Nuclear Physics Concepts in the Study of Atomic Cluster Physics, Lecture Notes in Physics Vol 404 (Eds.: R. Schmidt, H. O. Lutz, R. Dreizler), Springer, Berlin, Heidelberg, **1992**, p.244.

[43] J. Tiggesbäumker, L. Köller, H. O. Lutz, K. H. Meiwes-Broer in Physics and Chemistry of Finite Systems: From Clusters to Crystals, NATO ASI Series Vol. 374 (Eds.: P. Jena, S. N. Khanna, B. K. Rao), Springer, Dordrecht, **1992**, p. 1001.

[44] J. Tiggesbäumker, L. Köller, K.-H. Meiwes-Broer, A. Liebsch, *Phys. Rev. A* **1993**, *48*, R1749.

[45] J. C. Idrobo, W. Walkosz, S. F. Yip, S. Öğüt, J. Wang, J. Jellinek, *Phys. Rev. B* 2007, *76*, 205422.

[46] M. F. Jarrold, K. M. Creegan, *Int. J. Mass Spectrom. Ion Process.* **1990**, *102*, 161.

[47] M. Lindinger, K. Dasgupta, G. Dietrich, S. Krückeberg, S. Kuznetsov, K. Lützenkirchen, L. Schweikhard, C. Walther, J. Ziegler, *Z. Phys. D* **1997**, *40*, 347.

[48] T. Yasuike, K. Nobusada, *Phys. Chem. Chem. Phys.* **2013**, *15*, 5424.

[49] W. Harbich, S. Fedrigo, J. Buttet, *Chem. Phys. Lett.* **1992**, *195*, 613.

[50] D. M. Rayner, K. Athanassenas, B. A. Collings, S. A. Mitchell, P. A. Hackett in Theory of Atomic and Molecular Clusters: With a Glimpse at Experiments, Springer Series in Cluster Physics (Ed.: J. Jellinek), Springer, Berlin, Heidelberg, **1999**, p. 371.

[51] B. A. Collings, K. Athanassenas, D. M. Rayner, P. A. Hackett, *Chem. Phys. Lett.* **1994**, *227*, 490.

[52] T. Ito, PhD Thesis, Kyushu University (Japan), **2015**.

[53] A. Terasaki, T. Majima, C. Kasai, T. Kondow, *Eur. Phys. J. D* **2009**, *52*, 43.

[54] K. Egashira, C. Bartels, T. Kondow, A. Terasaki, *Eur. Phys. J. D* **2011**, *63*, 183.

[55] A. Terasaki, S. Minemoto, M. Iseda, T. Kondow, *Eur. Phys. J. D* **1999**, *9*, 163.

[56] S. Kawamura, M. Yamaguchi, S. Kono, M. Arakawa, T. Yasuike, T. Horio, A. Terasaki, *J. Phys. Chem. A* **2023**, *127*, 6063.

[57] C. Yu, R. Schira, H. Brune, B. von Issendorff, F. Rabilloud, W. Harbich, *Nanoscale* **2018**, *10*, 20821.

[58] S. Fedrigo, W. Harbich, J. Buttet, *Phys. Rev. B* **1993**, *47*, 10706.

[59] W. Harbich, S. Fedrigo, J. Buttet, *Z. Phys. D* **1993**, *26*, 138.

[60] S. Fedrigo, W. Harbich, J. Belyaev, J. Buttet, *Chem. Phys. Lett.* **1993**, 211, 166.

[61] N. Iwe, K. Raspe, F. Martinez, L. Schweikhard, K.-H. Meiwes-Broer, J. Tiggesbäumker, *Phys. Chem. Chem. Phys.* **2023**, *25*, 1677.

[62] T. Lünskens, A. von Weber, M. Jakob, T. Lelaidier, A. Kartouzian, U. Heiz, *J. Phys. Chem. C* **2017**, *121*, 9331.

[63] M. Thämer, A. Kartouzian, P. Heister, T. Lünskens, S. Gerlach, U. Heiz, *small* **2014**, *10*, 2340.

[64] C. M. Aikens, S. Li, G. C. Schatz, *J. Phys. Chem. C* **2008**, *112*, 11272.

[65] E. B. Guidez, C. M. Aikens, *J. Phys. Chem. C* **2013**, *117*, 12325.

[66] V. Bonačić-Koutecký, J. Pittner, M. Boiron, P. Fantucci, *J. Chem. Phys.* **1999**, *110*, 3876.

[67] V. Bonačić-Koutecký, M. Boiron, J. Pittner, P. Fantucci, J. Koutecký, *Eur. Phys. J. D* **1999**, *9*, 183.

[68] M. Harb, F. Rabilloud, D. Simon, A. Rydlo, S. Lecoultre, F. Conus, V. Rodrigues, C. Félix, *J. Chem. Phys.* **2008**, *129*, 194108.

[69] F. Rabilloud, *J. Chem. Phys.* **2014**, *141*, 144302.

[70] R. Schira, F. Rabilloud, *J. Phys. Chem. C* **2018**, *122*, 27656.

[71] F. Rabilloud, *Eur. Phys. J. D* **2013**, *67*, 18.

[72] B. Anak, M. Bencharif, F. Rabilloud, *RSC Adv.* **2014**, *4*, 13001.

[73] F. Rabilloud, *J. Phys. Chem. A* **2013**, *117*, 4267.

[74] R. Schira, F. Rabilloud, *J. Phys. Chem.* **2019**, *123*, 6205.

[75] M. Harb, F. Rabilloud, D. Simon, *Chem. Phys. Lett.* **2009**, *476*, 186.

[76] V. Kasperovich, V. V. Kresin, *Phil. Mag.* **1998**, *78*, 385.

[77] H. Haberland, *Nature* **2013**, *494*, E1.

[78] T. Yasuike, K. Nobusada, M. Hayashi, *Phys. Rev. A* **2011**, *83*, 013201.

[79] M. Shibuta, K. Yamamoto, T. Ohta, T. Inoue, K. Mizoguchi, M. Nakaya, T. Eguchi, A. Nakajima, *ACS Nano* **2021**, *15*, 1199.

[80] A. Campos, N. Troc, E. Cottancin, M. Pellarin, H.-C. Weissker, J. Lermé, M. Kociak, M. Hillenkamp, *Nat. Phys.* **2019**, *15*, 275.

[81] O. M. Bakr, V. Amendola, C. M. Aikens, W. Wenseleers, R. Li, L. D. Negro, G. C. Schatz, F. Stellacci, *Angew. Chem. Int. Ed.* **2009**, *48*, 5921.

[82] G.-T. Bae, C. M. Aikens, *J. Phys. Chem. C* **2012**, *116*, 10356.

[83] J. Ma, Z. Wang, L.-W. Wang, *Nat. Commun.* **2015**, *6*, 10107.

[84] T. Lünskens, P. Heister, M. Thämer, C. A. Walenta, A. Kartouzian, U. Heiz, *Phys. Chem. Chem. Phys.* **2015**, *17*, 17541.

[85] A. O'Keefe, D. A. G. Deacon, *Rev. Sci. Instrum.* **1988**, *59*, 2544.

[86] T. Yasuike, private communication.

2. Experimental Procedures

2.1. Overview

In the gas phase, conventional spectroscopy such as optical absorption spectroscopy based on transmission measurement is difficult because a decrease in light intensity is so small due to an extremely low density of the sample that it is undistinguishable from fluctuation in the light intensity. Therefore, two types of supersensitive measurements were performed in this study, i.e., photodissociation action spectroscopy and cavity ring-down spectroscopy. In the former, the photodissociation yield of the parent ion is normalized by the number of incident photons to derive a photodissociation cross section as a measure of optical absorption on the premise that photoabsorption leads definitely to dissociation of ions. On the other hand, a sample is placed between a pair of high-reflectivity mirrors in the latter, which is irradiated by a pulsed laser. Because the intensity of the incident pulse decays exponentially during multiple reflection between the mirrors plus additional losses by the sample, the decay-rate difference between with and without the sample becomes a measure of optical absorption when it is normalized by the density of the sample. In this section, a brief explanation of the experimental setup and procedures are given. Detailed descriptions of the apparatus and principles are presented in Chapters 4 and 5.

The two spectroscopic experiments were carried out in a vacuum by employing the same apparatus with two configurations shown in Figure 2.1. Silver cluster cations produced by magnetron sputtering were transported along the red arrows in Figure 2.1 by octopole ion guides and quadrupole ion deflectors. The generated clusters have both positive and negative charges and various sizes, i.e., the number of constituent atoms in the cluster. Only the cations were carried downstream by applying optimal voltages on

the first ion deflector. A size of the clusters of interest was selected by the first quadrupole mass filter. The size-selected ion beam was introduced into a temperature-controlled linear ion trap, where the loaded ions were interacted with incident photons. After laser irradiation, the trapped ions were ejected toward an ion-detector electrode connected to an ammeter (Picoammeter 6485, Keithley Instruments, Inc.) to measure the number of the ions. Note that only the parent ions were monitored through the second mass filter in front of the detector electrode in photodissociation spectroscopy. At the same time, the laser pulses were detected either by a photodiode for photodissociation spectroscopy or by a photomultiplier tube for cavity ring-down spectroscopy. The photodiode was calibrated beforehand by a laser-power meter to convert the resultant voltage to laser power. The photomultiplier tube was connected to an oscilloscope to record temporal profiles of the intensity of laser pulses.

2.2. Vacuum system

The experimental apparatus is composed of several vacuum chambers. The turbomolecular pumps were installed in six chambers containing the magnetron, ion deflectors, and mass filters. All the pumps were backed by rotary pumps. The base pressure inside the setup was ~ 10^{-5} Pa, which was sufficiently low to prevent the clusters from reacting with residual gases such as oxygen. An additional mechanical booster pump equipped behind the turbomolecular pump at the magnetron chamber was powered on during sputtering in the presence of buffer gases introduced for cluster generation. The working pressure in the magnetron chamber was typically ~ 10^{-1} Pa; pressures in the downstream chambers were kept sufficiently low by differential pumping, which enabled the present cluster study.

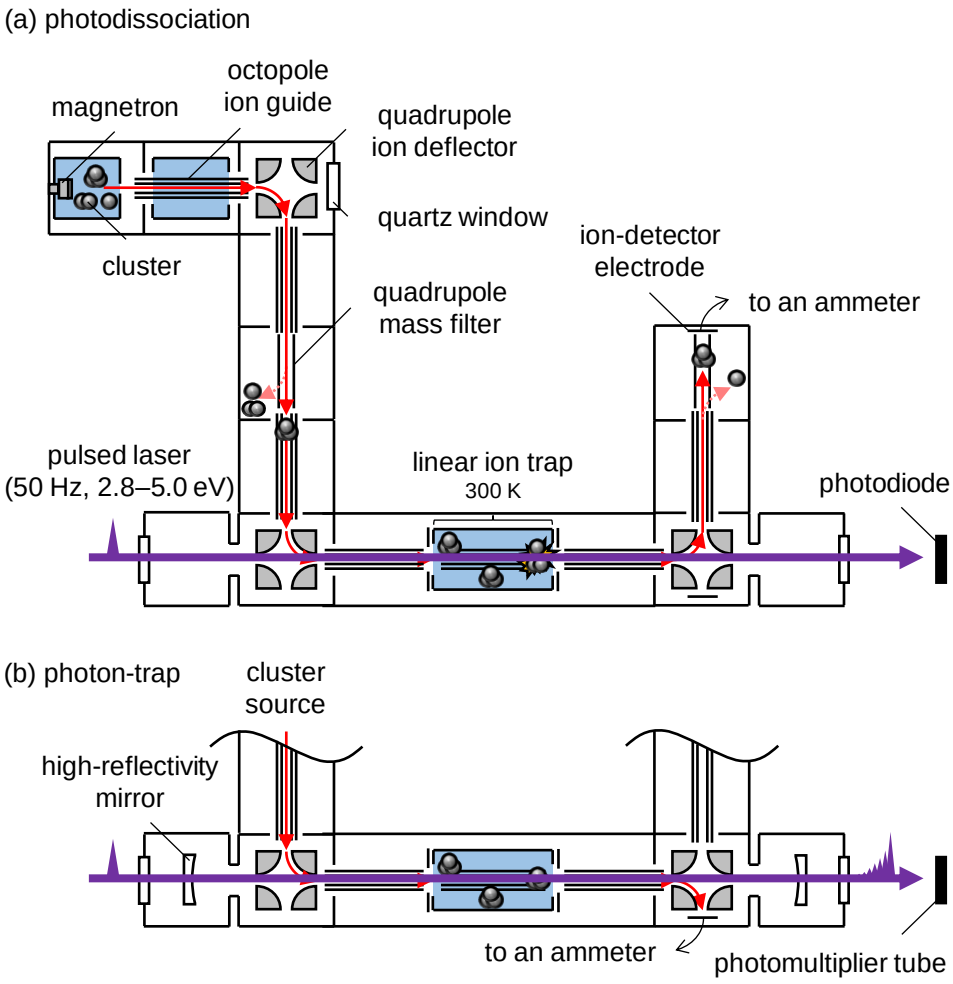

Figure 2.1. A schematic view of the experimental setup. Two configurations for photodissociation and cavity ring-down spectroscopies are depicted in (a) and (b), respectively.

2.3. Magnetron sputtering for cluster generation

Various methods have been utilized for cluster generation historically, e.g., metal-vapor gas aggregation [1] and laser vaporization [2, 3]. Amongst the methods, magnetron sputtering is known as a powerful method to produce an intense cluster-ion beam, which has originally been utilized for preparation of thin films since its development. It was first employed for cluster generation by Haberland et al. in 1992

[4]. Recently, the magnetron-sputtering cluster-ion source “nanojima®” was developed, which was reported to produce more than 1 nA of silver cluster anions after size selection [5].

The mechanism is illustrated in Figure 2.2. The magnetron-sputtering cluster source consists of a magnetron and an aggregation cell. Two types of gases are used to generate clusters, i.e., a sputter gas and a buffer gas, which are introduced into the gap of magnetron electrodes and the aggregation cell, respectively. The sputter gas ionized by discharge is accelerated by an electric field toward the cathode, a metal plate called a “metal target”, to sputter metal atoms or ions from the surface. Especially, the ionization is promoted by electrons trapped by a magnetic field in magnetron sputtering. The sputtered atoms and ions are decelerated and cooled by the buffer gas to grow into clusters by three-body collision with the buffer gas and other metal atoms, ions, or clusters. An example of mass spectra of generated clusters is depicted in Figure 2.3. Note that the clusters thus generated are not monodispersed. Additionally, positively and negatively charged clusters as well as neutrals are generated at the same time. It is necessary to select the charge state and size of interest to reveal optical responses of clusters as mentioned below.

A silver plate (Kojundo Chemical Laboratory Co., Ltd., 99.99%) was used as a metal target in the present study. A direct-current voltage was applied between the anode and the metal target. Argon and helium gases (99.99995%) were introduced as sputter and buffer gases, respectively. Their flow rates were kept constant during experiments by mass flow controllers (MODEL 3660 for argon and MODEL 3650 for helium, Kofloc Corp.). The position of the magnetron was designed to be adjustable along its axis to tune an aggregation length through the buffer gas. Size distribution of generated clusters

were dependent on the following parameters, i.e., the direct-current voltage, the gas flow rates, and the aggregation length, which were optimized for the cluster size of interest before spectroscopic measurements.

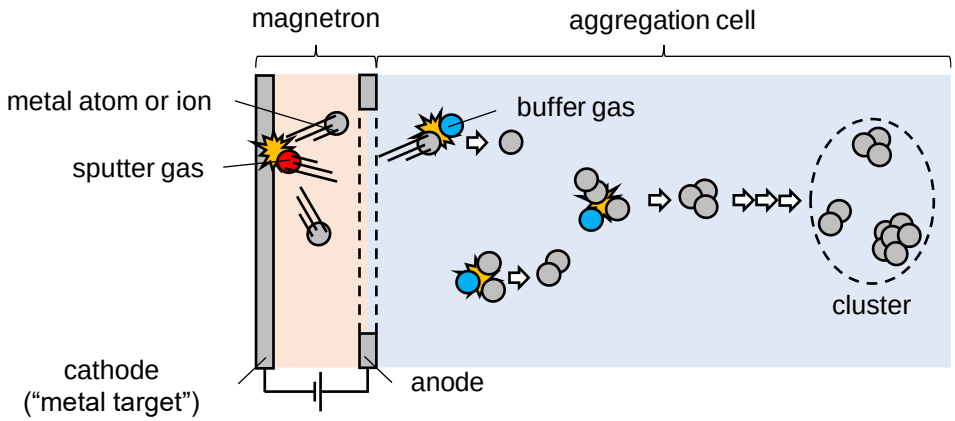

Figure 2.2. The illustration of cluster generation employing magnetron sputtering.

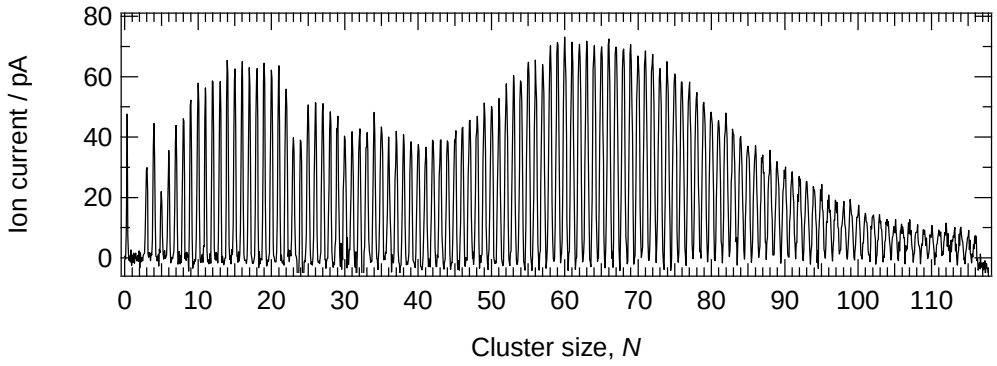

Figure 2.3. An example of mass spectra of silver cluster cations, Ag_N^+, generated by the present cluster source. This mass spectrum was measured at the third octopole ion guide, which was temporary connected to an ammeter while scanning the cluster size by the first mass filter.

2.4. Ion optics

The system to transport the ions is called ion optics. Especially, octopole ion guides and quadrupole ion deflectors were used in the present study. An octopole ion guide consists of eight rod electrodes arranged cylindrically around the central axis. The rods are alternately wired and thus divided into two groups, where the opposite phases of a radio-frequency voltage are applied to each group. Ions entering an ion guide undergo the resultant effective potential to stay inside, which pass through the ion guide if parameters of the radio-frequency voltage such as its amplitude and frequency are optimized to the mass of the sample. A quadrupole ion deflector consists of four electrodes with a cylindrical surface, which are arranged at corners of a square. The diagonally arranged electrodes are wired together. Different direct-current voltages are applied to the two pairs of the electrodes. When the neutral, positive and negatively charged clusters enter a quadrupole ion deflector, the neutral ones pass straight through the deflector, while charged clusters are bent by the electric field perpendicularly. The directions are opposite between cations and anions. Therefore, an ion deflector works to select the charge state of the clusters.

Power supplies for the ion optics are as follows: the ion guides were operated by homemade radio-frequency drivers [6] generating two outputs corresponding to the opposite phases of a radio-frequency voltage with a common direct-current voltage. The circuit of the drivers are depicted in Figure 2.4. The description of the components in Figure 2.4 is listed in Table 2.1. The radio-frequency voltage is generated by a LC circuit mainly consisting of a tank coil inside the driver and the ion guides themselves, which is amplified by vacuum tubes. The coil is designed to exchangeable, which enables adjusting the frequency to the cluster size of interest. The amplitude is also tunable by

another direct-current power supply, which determines an accelerating voltage of electrons inside the vacuum tubes. The direct-current voltages for offset bias of the octopoles and for the ion deflectors are prepared by two direct-current power supplies with potentiometers as resistive dividers.

2.5. Size selection by a quadrupole mass filter

A quadrupole mass filter is composed of four rod electrodes arranged symmetrically around the central axis. Opposite phases of a radio-frequency voltage are applied to neighboring electrodes. The superposition of direct-current and radio-frequency voltages is applied to the two pairs of the rods with different polarities. When a group of ions with different masses enters the mass filter, only ions with a specific mass can pass through the filter depending on the direct-current voltage and the amplitude of the radio-frequency voltage. In the present study, two quadrupole mass filters (MAX-16000, Extrel CMS) commercially available were employed for size selection.

2.6. Linear ion trap

A linear ion trap is a powerful tool for spectroscopic studies in the gas phase. It enables preparation of an ionic sample at a density sufficiently high for spectroscopic studies. It consists of an octopole ion guide arranged between two end electrodes. The ion guide works for radial confinement of ions, while loading/extracting ions and axial confinement are controlled by the voltages applied to the end electrodes with the aid of a buffer gas introduced into the trap.

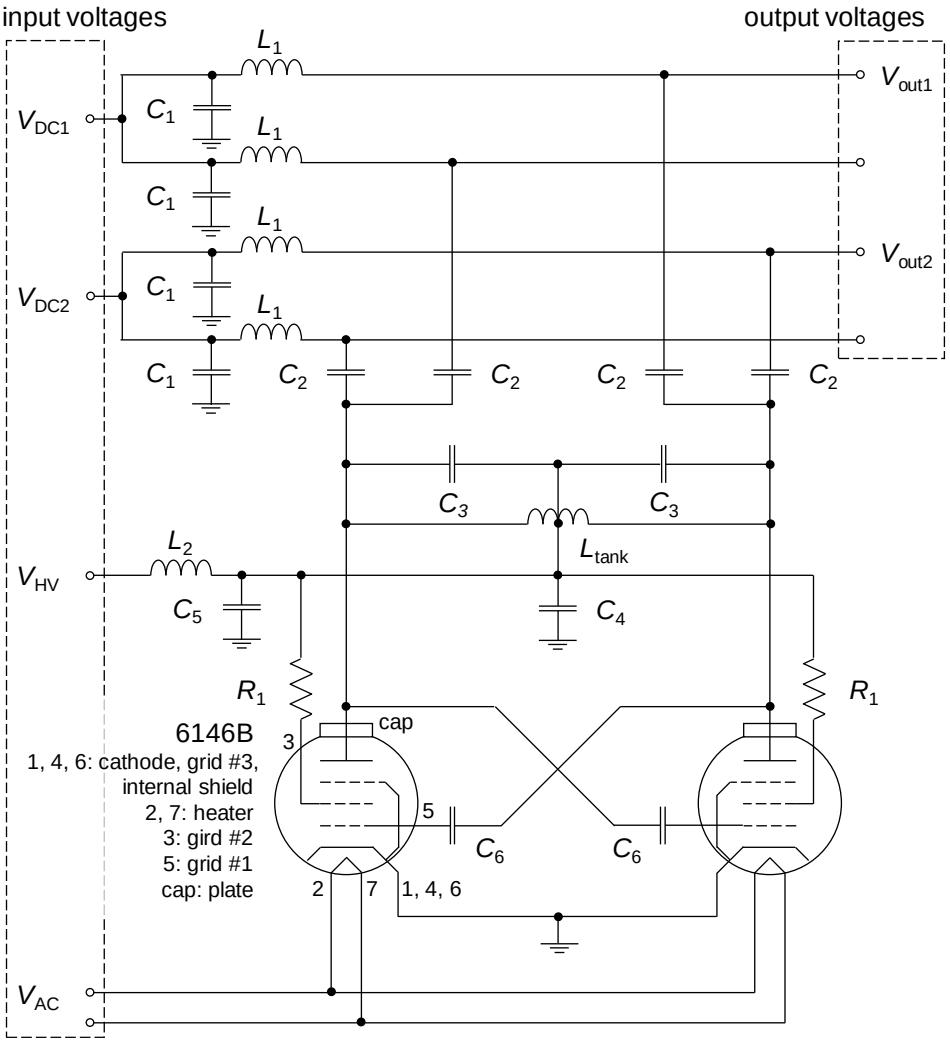

Figure 2.4. The circuit of the homemade radio-frequency drivers, which was slightly modified from the original design [6].

Table 2.1. Description of the components of the radio-frequency drivers.

Component	Value	Note
V_{DC1}, V_{DC2}	max 200 VDC	direct-current component of V_{out1}/V_{out2}
		variable
V_{HV}	max 350 VDC	grid voltage of 6146B
		variable to tune amplitude
V_{AC}	6.3 VAC 2A	for heater of 6146B
V_{out1}, V_{out2}	max 940 Vpp, 340–1100 kHz	dependent on parameters
C_1	0.1μF, 1 kV	ceramic
C_2	1000 pF, 3 kV	ceramic
C_3	100 pF	ceramic
C_4	0.1μF, 1 kV	ceramic
C_5	0.1μF, 1 kV	ceramic
C_6	3 pF, 500 V	mica
R_1	10 kΩ, 20 W	wire wound
L_1	2.2 mH, 60 mA	choking radio-frequency component
L_{tank}	230–3300 μH	copper wire wound in 60-mm diameter
		exchangeable to tune frequency
L_2	2.0 mH, 250 mA	choking radio-frequency component
6146B		vacuum tube

The same type of the radio-frequency driver mentioned above was employed as a power supply for the octopole. The difference between the octopole as a trap and that as a guide is phases of the radio-frequency voltage applied to the poles. Majima et al. revealed that spatial distribution of ions in a linear octopole trap drastically changes depending on its operation mode [7]; ions are located off-center when the opposite phases of a radio-frequency voltage are applied to the eight rods alternately, while ions are concentrated around the central axis during a quasi-quadrupole mode, where neighboring poles are wired to form four pairs of electrodes. Opposite phases of the radio-frequency voltage is applied to the neighboring electrode pairs to mimic a quadrupole. In the present study, the octopole ion guide was operated in the latter mode to maximize interaction between trapped clusters and an incident laser beam.

An operation scheme of an ion trap is depicted in Figure 2.5, which illustrates direct-current voltages applied to the entrance and exit electrodes during the operation. The operation is divided into three steps: (a) loading, (b) trapping, and (c) extracting ions. During the first step, a direct-current voltage is applied to the exit electrode to form a potential barrier that prevents the ions from passing through the exit. A buffer gas decelerates the ions inside the trap to avoid their leakage through the entrance electrode. At the second step, after the sufficient number of ions are loaded, the direct-current voltage applied to the entrance electrode is raised to terminate the ion loading for storage of the ions inside the trap. The stored ions are thermalized by a buffer gas and irradiated with a pulsed laser during the second step. Finally, the ions are extracted from the trap towards an ion-detector electrode connected to an ammeter. The potential is controlled by digital outputs implemented in an analogue output device (PCI-6703, NATIONAL INSTRUMENTS CORP.) installed in a personal computer. Analogue and TTL signals

from the device adjust the voltages applied to the entrance and exit electrodes, respectively. The durations of the TTL signals are variable to adjust time intervals of each step properly.

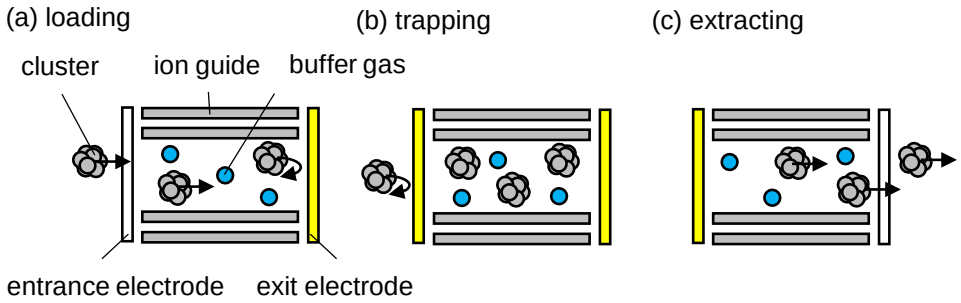

Figure 2.5. Potential control of the entrance and exit lenses composing an ion trap. The operation is divided into three steps: (a) loading, (b) trapping, and (c) extracting ions. Direct-current voltages are applied to the yellow-colored electrodes to form potential barriers for ions.

In the present study, a helium gas was introduced as a buffer gas. The flow rate was controlled by a needle valve. A typical pressure of the buffer helium gas was ~ 0.1 Pa, which was estimated from a partial pressure of helium measured by a residual gas analyzer equipped at the second-deflector chamber.

2.7. Laser system and photodetectors

A tunable nanosecond-pulsed optical parametric oscillator (OPO) laser (50 Hz, NT230-50, EKSPLA) was employed in this study. Its optical path was adjusted by prisms and apertures. The latter also worked as beam shapers of the laser determining its spot size. Especially, two prisms mounted on a translation stage were placed in front

of the ion trap, which enabled moving the optical path parallel to the central axis of the trap. Its power was controlled by neutral density filters. The spot size and laser power were adjusted appropriately (see more details in Chapter 3). In the experiment, it is important to control the number of incident laser pulses. In detail, the laser was always in operation during the experiment. To control the number of the incident pulses, N_{pulse}, a shutter was arranged in front of the ion trap, which was closed normally. The shutter was opened and closed when zero-th and N_{pulse}-th pulses were detected, respectively, by an oscilloscope device (PCI-5122, NATIONAL INSTRUMENTS CORP.) monitoring synchronization signals from the laser as triggers; as it took several milliseconds for the shutter to open, the zero-th pulse was damped by the shutter, whereas the first pulse was introduced into the trap. The time for opening or closing the shutter was confirmed to be shorter than the interval of laser pulses of 20 ms. Pulse duration of the laser was also much shorter than the time for switching the shutter, which avoided missing the laser spot partially. The shutter was driven by a rotary solenoid, a power transistor, and a monostable multivibrator receiving a TTL signal from PCI-6703.

The incident photons were detected by a photodiode (S1337-1010BQ, Hamamatsu Photonics K.K.) in photodissociation spectroscopy and by a photomultiplier tube in cavity ring-down spectroscopy. A photodiode works as a current source when it is irradiated by light. The current is proportional to the number of the incident photons, which is converted to a voltage in a home-made circuit. The circuit used in this study is shown in Figure 2.6, where the output voltage becomes $V_{\mathrm{PD}} = -R_{\mathrm{f}} I_{\mathrm{SC}}$. A calibration curve was created beforehand between the laser power measured by a power meter (3A-P, Ophir) and an integrated value of the temporal profile of the resultant voltage monitored by the oscilloscope device PCI-5122.

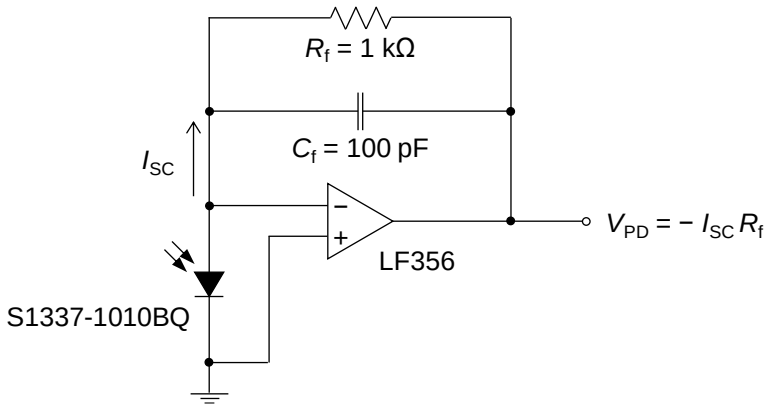

Figure 2.6. The circuit for a photodiode, which includes a resistor, a capacitor, and an operational amplifier.

References

[1] K. Sattler, J. Mühlbach, E. Recknagel, *Phys. Rev. Lett.* **1980**, *45*, 821.

[2] T. G. Dietz, M. A. Duncan, D. E. Powers, R. E. Smalley, *J. Chem. Phys.* **1981**, *74*, 6511.

[3] V. E. Bondybey, J. H. English, *J. Chem. Phys.* **1981**, *74*, 6978.

[4] H. Haberland, M. Karrais, M. Mall, Y. Thurner, *J. Vac. Sci. Technol., A* **1992**, *10*, 3266.

[5] H. Tsunoyama, C. Zhang, H. Akatsuka, H. Sekiya, T. Nagase, A. Nakajima, *Chem. Lett.* **2013**, *42*, 857.

[6] R. M. Jones, S. L. Anderson, *Rev. Sci. Instrum.* **2000**, *71*, 4335.

[7] T. Majima, G. Santambrogio, C. Bartels, A. Terasaki, T. Kondow, J. Meinen, T. Leisner, *Phys. Rev. A* **2012**, *85*, 053414.

3. Cluster-Growth Process in a Magnetron-Sputtering Source

3.1. Introduction

As described in Chapter 2, clusters generated in a magnetron-sputtering ion source are not monodispersed. Therefore, control of the size distribution is important in cluster studies: it is ideal to maximize the intensity of the clusters with the size of interest. The size distribution generated by magnetron sputtering depends on various parameters such as discharge power and gas flow rates. Here the author investigated the cluster-growth process to find optimal parameters for the size of interest.

Several groups have studied the process in a magnetron-sputtering cluster-ion source so far. Theoretically, the Smoluchowski rate equation [1, 2] is one of the most famous models, which describes irreversible aggregation processes of neutral particles. The rate equation was extended later to treat ionic particles in addition to neutrals [3]. Experimentally, controllability of the cluster-size distribution was studied for, e.g., aluminum [4] and silver [5, 6] cluster anions, with the aid of the extended Smoluchowski rate equation. These experimental studies on the cluster-generation process reported so far are based on a mass-spectrometric analysis principally.

In this context, optical emission spectroscopy provides an opportunity to characterize plasma generated in the magnetron for further understanding the cluster-growth process. For example, an optical emission spectrum provides information on the numbers of emitting atoms and ions; in previous studies on high-power impulse magnetron sputtering, an ionization yield of sputtered atoms was reported to be higher than that in direct-current sputtering [7, 8]. However, application of optical emission spectroscopy to cluster studies is limited: a study on the carbon dimer [9] is one of the few examples. Especially, no study on metal clusters has been reported until now.

In this chapter, an analysis of the cluster-growth process in a direct-current magnetron-sputtering source is presented. Experimental results of both mass spectrometry and optical emission spectroscopy are provided to discuss the cluster-growth process. A simple statistical model is proposed to interpret the experimental results, presenting a scenario of cluster growth.

3.2. Experimental procedures

The experiments were performed by the same apparatus described in Chapter 2. Silver cluster cations generated in the magnetron-sputtering cluster-ion source were transported thru the first mass filter for mass selection down to the third ion guide, which was connected to an ammeter (Picoammeter 6485, Keithley Instruments, Inc.), to record a mass spectrum; a direct-current voltage of −35 V was applied to the rod electrodes of the third ion guide to collect the ions. Light emission from the magnetron was detected through a fused silica window by a Czerny–Turner spectrometer (FLAME-S, Ocean Optics, Inc.) coupled with a calcium fluoride plano-convex lens (Sigma Koki Co., Ltd.) and an optical fiber (P400-2-UV-VIS, Ocean Optics, Inc.). Mass and emission spectra were measured as a function of discharge power of the magnetron up to 12 W. Gas flow rates of argon and helium were kept constant in this study: 122 and 208 sccm, respectively.

3.3. Experimental results

Figure 3.1 shows mass spectra of silver cluster cations measured by varying the discharge power. No cluster ion was detected below 3 W; a significant amount of clusters showed up at the discharge power of 4 W and above. Larger cluster cations appeared as the discharge power was raised; the largest cluster detected in this study was Ag_{115}^{+} due to limitation of the mass filter employed. Quantitatively, the average size of the cluster cations, $\langle N \rangle$, ranged from 4.8 at 3 W to 41 at 12 W as shown in Figure 3.1, which is defined by the following equation:

$$\langle N \rangle = \frac{\sum_{N=1}^{115} I_N N}{\sum_{N=1}^{115} I_N}, \tag{3.1}$$

where I_N is the current of a silver cluster cation with a size of N. Corresponding emission spectra are depicted in Figure 3.2. All the emission lines in the spectra were assigned to neutral atoms of silver, helium, and argon by referring to Atomic Spectra Database of National Institute of Standards and Technology [10]. An energy-level diagram relevant to these emission lines is illustrated in Figure 3.3. Energies of the initial states of atomic silver are located at about 3.7 and 6.0 eV above its ground state, while those of atomic argon and helium are at 13–15 eV and 23.1 eV, respectively. Especially, amongst the emission lines, atomic silver exhibited a significant increase in its emission intensity with the discharge power, which qualitatively indicates that more silver atoms were sputtered at higher power.

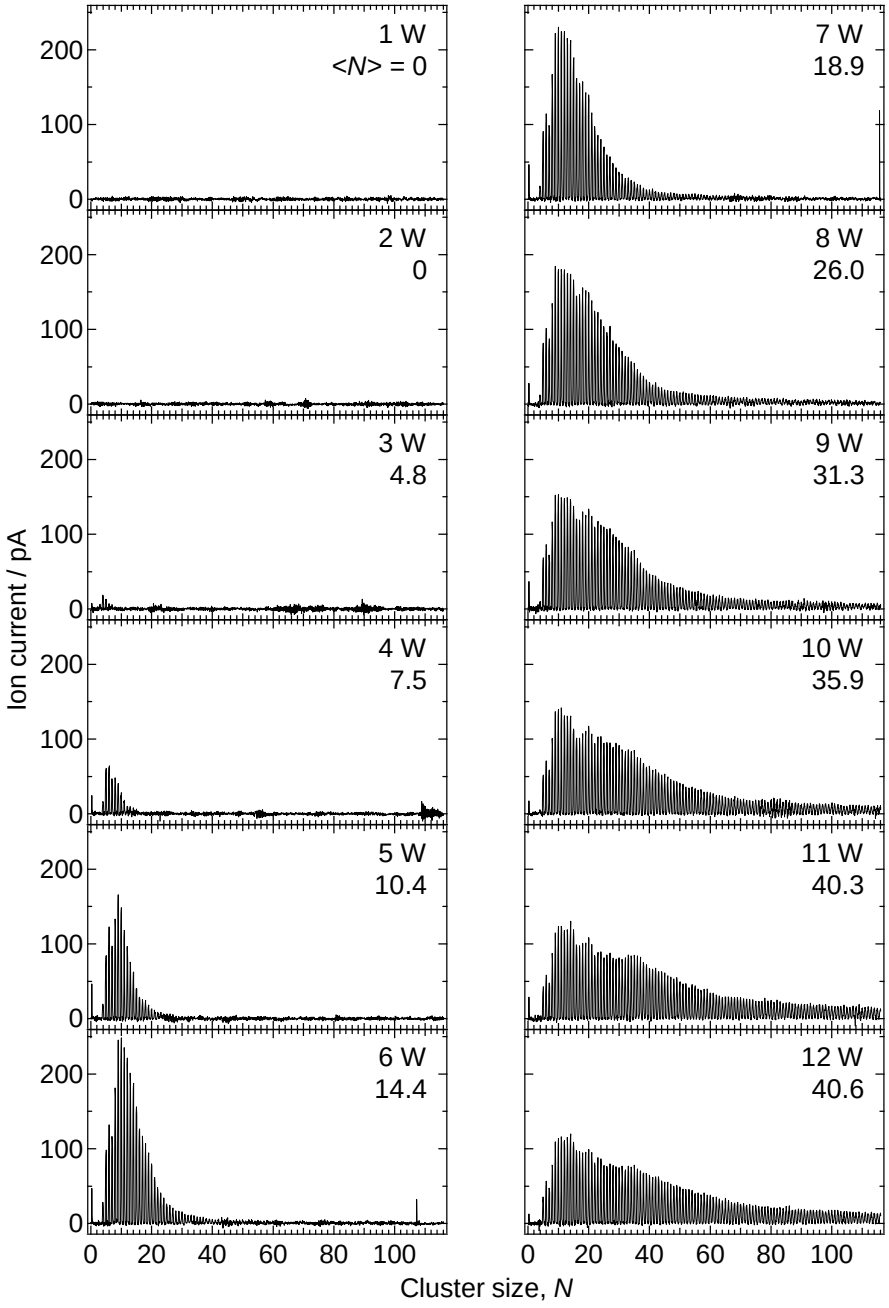

Figure 3.1. Mass spectra of silver cluster cations, Ag_N^+, measured as a function of discharge power of the magnetron.

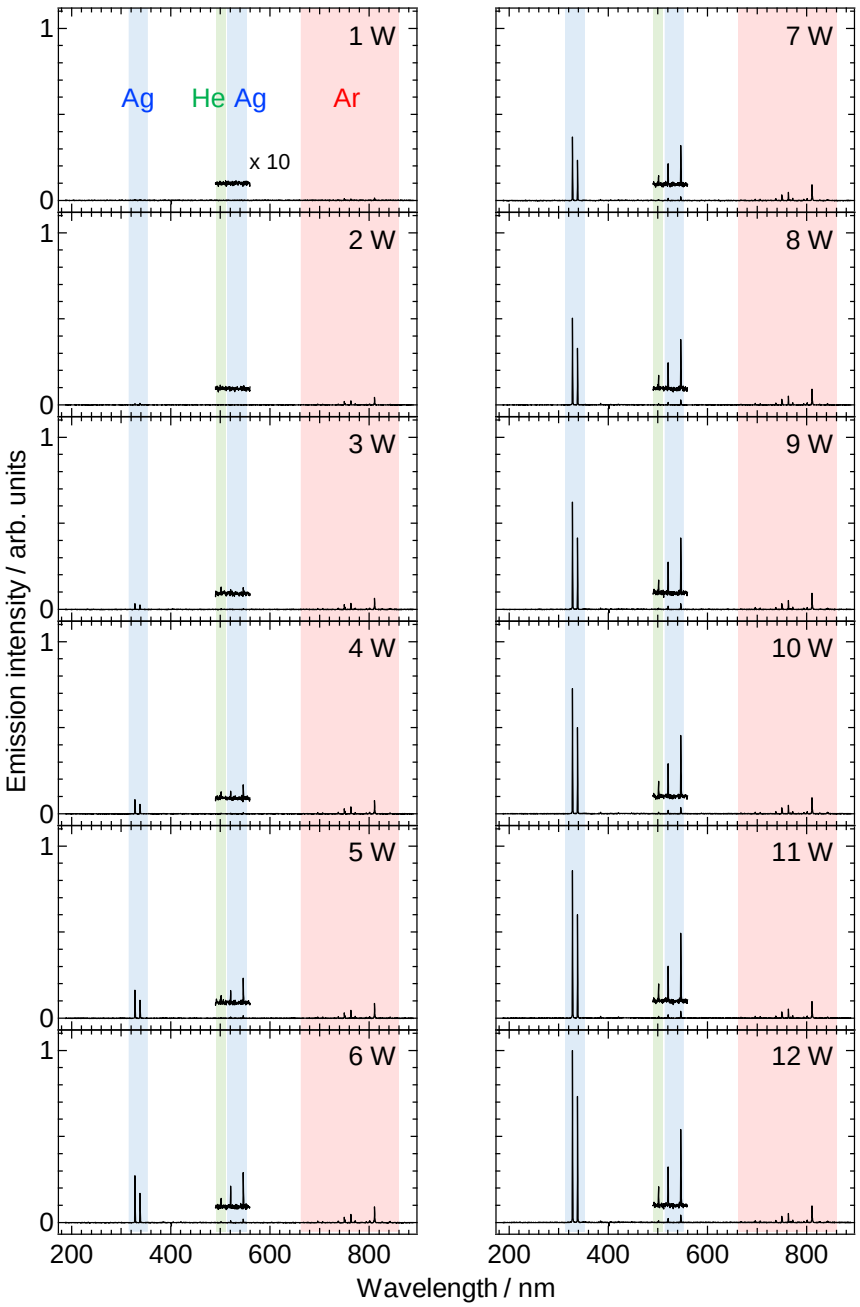

Figure 3.2. Emission spectra measured as a function of discharge power of the magnetron. Assignments of the emission lines are indicated.

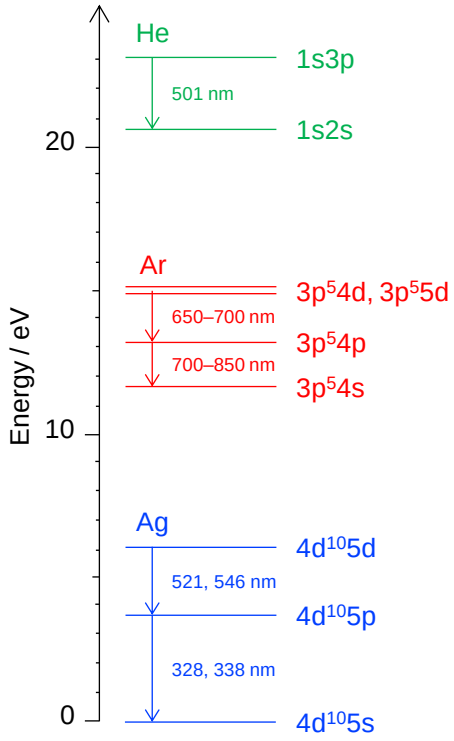

Figure 3.3. An energy-level diagram relevant to emission lines observed in the emission spectra. The ordinate indicates an electronic energy with respect to the ground states of each element.

3.4. Discussion

For interpretation of the experimental data, quantitative evaluation of the number of sputtered silver atoms is necessary. The intensity of a given emission line of atomic silver, I_{Ag}, is expressed by the following equation under an assumption that the population of the exited states follows the Boltzmann distribution:

$$I_{\mathrm{Ag}} = \beta g A N_{\mathrm{Ag}} \exp\left(-\frac{E_{\mathrm{i}}}{k_{\mathrm{B}} T_{\mathrm{e}}}\right), \tag{3.2}$$

Where β is a coefficient to convert an emission rate to intensity, g the statistical weight of the initial state, A the Einstein A coefficient of the corresponding electronic transition,

N_{Ag} the number of silver atoms, E_i the energy of the initial state with respect to the ground state, k_B the Boltzmann constant, and T_e the electronic temperature. This equation is rearranged as follows:

$$\ln \frac{I_{Ag}}{gA} = -\frac{E_i}{k_B T_e} + \ln \beta N_{Ag}. \quad (3.3)$$

Therefore, the values of βN_{Ag} are derived as vertical intercepts in linear plots of $\ln \frac{I_{Ag}}{gA}$ vs. E_i, which show a relative change in the number of sputtered silver atoms as a function of discharge power. Such Boltzmann plots were made for emission lines of atomic silver with wavelengths of 328, 338, 521, and 546 nm at each discharge power as depicted in Figure 3.4, where only data for the power of 6, 9, and 12 W are shown as examples. Physical constants relevant to the emission lines necessary for the Boltzmann plots were taken from Atomic Spectra Database of National Institute of Standards and Technology [10], which are listed with corresponding initial and final electronic configurations in Table 3.1. The relative change in the number of sputtered silver atoms obtained from the Boltzmann plots is shown in Figure 3.5 as a function of discharge power of magnetron, which is normalized by the value at 3 W. The number of sputtered silver atoms increased nonlinearly as the power was raised. To correlate the number of sputtered silver atoms with the measured mass spectra, the average cluster size $<N>$ is plotted as a function of the number of sputtered silver atoms N_{Ag} normalized by that at 3 W in Figure 3.6 in logarithmic scales. The average cluster size increases with the number of sputtered silver atoms. However, the average size is not simply proportional to the number of sputtered silver atoms; it rather shows a power law with 0.50 ± 0.02.

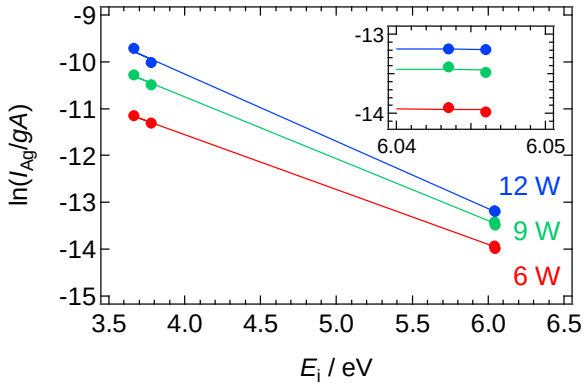

Figure 3.4. Examples of Boltzmann plots for data at discharge power of 6, 9, and 12 W. Solid lines are the best fits to the data. An enlarged view in the energy range of 6.04–6.05 eV is also depicted as an inset. $k_B T_e \sim 0.8$ eV was derived without significant dependence on the discharge power.

Table 3.1. Physical constants relevant to emission lines of atomic silver observed in this study. Corresponding electronic configurations of initial/final states are also listed.

Wavelength / nm	A / 10^8 s^{-1}	E_i / eV	g	Transition
328	1.40	3.778	4	5p ($^2P_{3/2}$) → 5s ($^2S_{1/2}$)
338	1.30	3.664	2	5p ($^2P_{1/2}$) → 5s ($^2S_{1/2}$)
521	0.75	6.043	4	5d ($^2D_{3/2}$) → 5p ($^2P_{1/2}$)
546	0.86	6.046	6	5d ($^2D_{5/2}$) → 5p ($^2P_{3/2}$)

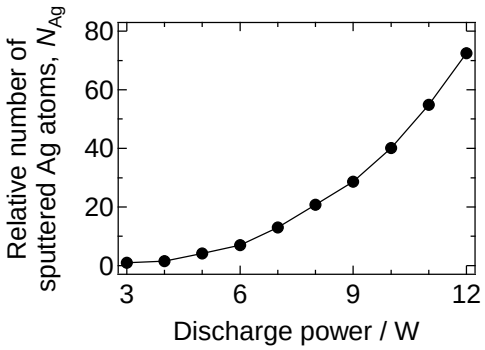

Figure 3.5. The relative change in the number of sputtered silver atoms as a function of discharge power. The ordinate is normalized by the value at the power of 3 W.

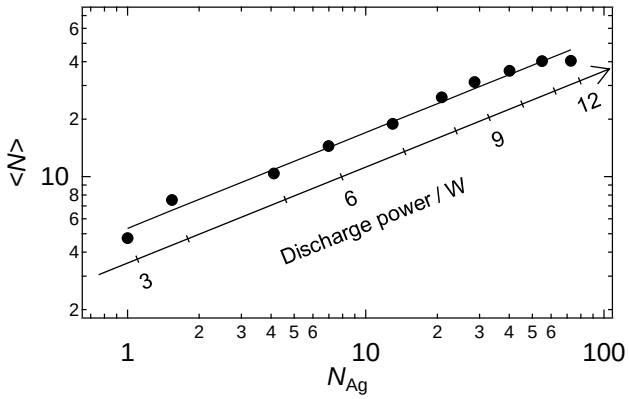

Figure 3.6. Relationship between <*N*> and N_{Ag} normalized by the value at 3 W. Solid circles represent experimental data. The solid line is the best fit to the logarithmic plots.

Before analyzing the spectroscopic result further, the measured mass spectra were modeled; the present mass spectra were found to be well reproduced by a linear combination of multiple Poisson distributions:

$$P(N) = \sum_{i=1}^{10} \alpha_i \frac{\lambda_i^N \exp(-\lambda_i)}{N!}, \tag{3.4}$$

where i labels Poisson distributions with different average cluster sizes of λ_i and α_i is its amplitude. A_i's are parameters for fitting, whereas λ_i 's are fixed values of 1, 3, 7, 13,

21, 32, 45, 61, 79, and 100 for i = 1–10, respectively. Intervals between neighboring λ_i 's were given by full widths at half maximum of Gaussians with standard deviations of $\lambda_i^{1/2}$ centered at λ_i, which well approximates Poisson distributions with average sizes of λ_i:

$$\lambda_{i+1} - \lambda_i \simeq \sqrt{(8\ln 2)\lambda_i}, \tag{3.5}$$

staring with $\lambda_1 = 1$. The linear combination of Poisson distributions with average sizes thus determined allows reproducing the measured mass spectra by a minimal set of the distributions. Figure 3.7 shows that the experimental mass spectra were well reproduced by the linear combination. The fact that the measured mass spectra were reproduced by linear combinations of Poisson distributions suggests a "lattice model" of cluster formation, where a cluster source is divided into a grid of cells representing trajectories of clusters during aggregation (Figure 3.8 (a)); amongst metal atoms randomly distributed to the cells upon sputtering (Figure 3.8 (b)), those in the same cell are supposed to form a single cluster (Figure 3.8 (c)). Based on this model, a mass spectrum of clusters generated by magnetron sputtering follows a Poisson distribution with an average size proportional to an average density of sputtered atoms in the cluster source. The combinations of multiple Poisson distributions with different average sizes rather than a single Poisson distribution imply inhomogeneity in the density of sputtered silver atoms; it is well known that sputtered atoms in a magnetron are distributed In a ring-like profile with a radial gradient in the density. Given this fact, smaller clusters are generated along trajectories with lower average densities of sputtered atom, whereas larger clusters grow along trajectories with higher average densities. Another finding based on this lattice model is about a volume of the cluster-growth region; the average cluster size of the linear combination of multiple Poisson distributions expressed by Equation (3.4) is

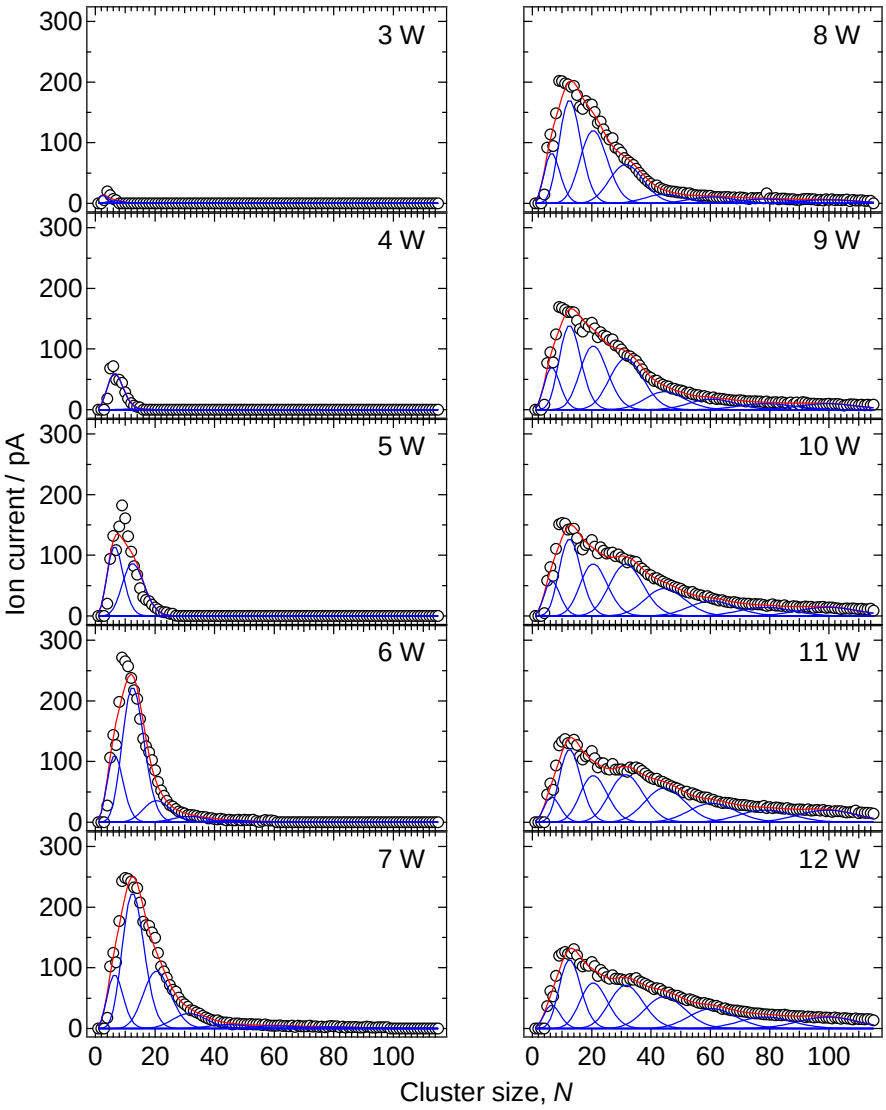

Figure 3.7. Comparison between the linear combination of the Poisson distributions and the experimental mass spectrum of silver cluster cations, Ag_N^+. The blue curves are Poisson distributions with different average sizes, while the red curves are their linear combination. The open circles are experimental ion currents of Ag_N^+.

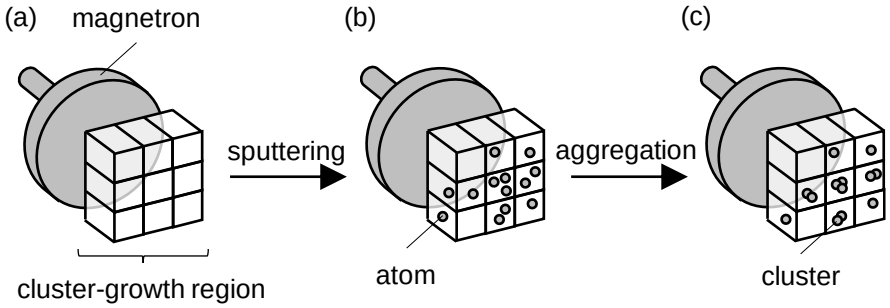

Figure 3.8. The lattice model for cluster formation by magnetron sputtering. See the text for detailed description.

$$\langle N \rangle = \frac{\sum_{N=1}^{115} NP(N)}{\sum_{N=1}^{115} P(N)} = \frac{\sum_{N=1}^{115}\left(\sum_{i=1}^{10} \alpha_i N \frac{\lambda_i^N \exp(-\lambda_i)}{N!}\right)}{\sum_{N=1}^{115}\left(\sum_{i=1}^{10} \alpha_i \frac{\lambda_i^N \exp(-\lambda_i)}{N!}\right)} = \frac{\sum_{i=1}^{10}\left(\alpha_i \sum_{N=1}^{115} N \frac{\lambda_i^N \exp(-\lambda_i)}{N!}\right)}{\sum_{i=1}^{10}\left(\alpha_i \sum_{N=1}^{115} \frac{\lambda_i^N \exp(-\lambda_i)}{N!}\right)}$$
$$= \frac{\sum_{i=1}^{10} \alpha_i \lambda_i}{\sum_{i=1}^{10} \alpha_i}, \tag{3.6}$$

which implies the average cluster size is proportional to the average density of sputtered atoms. The present finding that the atomic density was not proportional to the number of sputtered silver atoms as shown in Figure 3.6 suggests that the effective volume of the cluster-growth region was enlarged at higher discharge power of the magnetron, which leads to rarefaction of the sputtered atoms and inhibition of cluster growth probably because the sputtered atoms had larger kinetic energies than those at lower discharge power and traveled far from the metal target.

3.5. Summary

The cluster-growth process in a magnetron-sputtering cluster-ion source was investigated by optical emission spectroscopy and mass spectrometry to tune the cluster source for efficiently producing clusters with sizes of interest, in particular, in the larger size range. The number of sputtered silver atoms was estimated by measuring emission spectra of the magnetron plasma as a function of its discharge power, while size distributions of silver cluster cations were measured at the same time. The result was analyzed on the basis of a statistic model proposed in the present study. In this model, the size distribution of clusters follows a Poisson distribution with an average size proportional to the density of the atomic silver. The present mass spectra were reproduced by multiple Poisson distributions with several different average sizes rather than a single distribution. This can be ascribed to an inhomogeneous density profile of the sputtered atoms in the magnetron plasma. By relating the number of sputtered silver atoms with their density, expansion of an effective volume of the cluster-growth region was implied for higher discharge power, which leads to rarefaction of the sputtered atoms decelerating cluster growth. This result suggests a possibility to encourage generation of larger clusters, e.g., by preventing the sputtered atoms from rarefaction by decreasing their kinetic energy by a buffer gas. Based on this insight, the author was able to produce larger silver clusters successfully, which benefits spectroscopic experiments presented in the following chapters.

References

[1] M. von Smoluchowski, *Phys. Z.* **1916**, *17*, 557, 585.

[2] M. von Smoluchowski, *Z. Phys. Chem.* **1918**, *92*, 129.

[3] R. B. Huang, Q. Zhang, H. Chen, L. S. Zheng, *Eur. Phys. J. D* **1999**, *9*, 253.

[4] Z. Luo, W. H. Woodward, J. C. Smith, A. W. Castleman, Jr., *Int. J. Mass Spectrom.* **2012**, *309*, 176.

[5] C. Zhang, H. Tsunoyama, H. Akatsuka, H. Sekiya, T. Nagase, A. Nakajima, *J. Phys. Chem. A* **2013**, *117*, 10211.

[6] C. Zhang, H. Tsunoyama, Y. Feng, A. Nakajima, *J. Phys. Chem. C* **2016**, *120*, 5667.

[7] J. Bohlmark, J. Alami, C. Christou, A. P. Ehiasarian, U. Helmersson, *J. Vac. Sci. Technol., A* **2005**, *23*, 18.

[8] M. Hála, J. Čapek, O. Zabeida, J. E. Klemberg-Sapieha, L. Martinu, *Surf. Coat. Technol.* **2012**, *206*, 4186.

[9] A. Saxena, P. Kumar, S. Banerjee, K. P. Subramanian, B. Bapat, *Spectrosc. Lett.* **2014**, *47*, 114.

[10] National Institute of Standards and Technology, "Atomic Spectra Database | NIST", can be found under https://www.nist.gov/pml/atomic-spectra-database, **2018** (accessed 6 June 2019).

4. Photodissociation Action Spectroscopy

4.1. Introduction

Photodissociation action spectroscopy is one of the powerful techniques to investigate photoabsorption of molecules, clusters, and ions. Because a decrease in the number of the sample is measured instead of that in light intensity, this technique works well especially in the gas-phase study, where the density of samples is extremely low.

Many studies on photodissociation spectroscopy of metal clusters have been performed so far [1–32]. One of the series of such studies was conducted by Tiggesbäumker et al. [30–32]. They reported collective excitation of electrons in silver cluster cations, Ag_N^+ (N = 9 and 21), i.e., only one absorption band carrying most of the oscillator strengths originating from 5s valence electrons. In contrast, structure-rich less-intense absorption bands were reported for Ag_9Kr^+ by Rayner et al. [33, 34]. The difference was interpreted from the point of view of an internal energy of the cluster [33–35]; the temperature corresponding to the internal energy was estimated to be ~2000 K in Tiggesbäumker et al.'s study. This implies that temperature control of a sample is important in investigating photoabsorption.

In this context, an ion trap provides two benefits: preparation of a sample both at a high density and at a well-defined temperature. Because of these advantages, photoabsorption spectra of metal clusters have been measured by employing an ion trap either via photodissociation action spectroscopy, which is presented in this chapter, or via highly sensitive photoabsorption spectroscopy [36–41], as will be discussed in Chapter 5.

In this study, photodissociation spectroscopy is performed on silver cluster cations with the sizes up to N = 92. The origin of electronic excitations in these silver clusters will be discussed on the basis of spectral profiles and resonance energies observed

by experiment along with geometric structures obtained by the Clemenger–Nilsson model [42].

4.2. Principle

Photodissociation is a chemical process of a molecule resulting in production of fragments upon absorption of photons. Generally, a molecule undergoes various relaxation processes after electronic excitation by light absorption, e.g., light emission, internal conversion via vibronic coupling, intersystem crossing, bond dissociation in the course of intramolecular vibrational energy redistribution (IVR), and deexcitation by collision with a buffer gas especially in a trap. A photodissociation cross section is a good measure for the strength of light absorption if dissociation is a predominant deexcitation channel for the photoexcited molecules. Technically, there are two experimental modes to evaluate photodissociation cross sections: monitoring decrease in the number of parent molecules or increase in those of fragments. The former was adopted in the present study because a quadrupole mass filter does not allow one to observe all the fragments at the same time.

Suppose that the probability of dissociation for photoexcited ions be unity. When a cloud of parent ions with the length of L_{trap} and the density of $n_{\mathrm{parent}}\left(x,y,z,\tilde{t}\right)$ is irradiated by a laser pulse with a flux of $F\left(x,y,z,\tilde{t}\right)$, the change in the flux with respect to the penetration length along the trap axis, z, is expressed by

$$\mathrm{d}F\left(x,y,z,\tilde{t}\right)=-\sigma_{\mathrm{dis}}n_{\mathrm{parent}}\left(x,y,z,\tilde{t}\right)F\left(x,y,z,\tilde{t}\right)\mathrm{d}z \tag{4.1}$$

as derived from the differential form of the Beer–Lambert law, where (x, y) is a radial vector perpendicular to the trap axis with its origin at the center of the trap and $\tilde{t}$ is a

parameter for describing a temporal intensity profile of the incoming laser pulse. Therefore, $n_{\text{parent}}\left(x,y,z,\tilde{t}\right)$ is defined as the density of the parent ions that experiences the photon flux at $\tilde{t}$, i.e., $F\left(x,y,z,\tilde{t}\right)$ (see Figure 4.1). The change in the number of the parent ions in the volume of d*x*d*y*d*z* after experiencing the photon flux $F\left(x,y,z,\tilde{t}\right)$ within $\mathrm{d}\tilde{t}$ equals to the change in the number of the photons irradiating the parent ions, i.e.,

$$\mathrm{d}n_{\text{parent}}\left(x,y,z,\tilde{t}\right)\mathrm{d}x\mathrm{d}y\mathrm{d}z=\mathrm{d}F\left(x,y,z,\tilde{t}\right)\mathrm{d}x\mathrm{d}y\mathrm{d}\tilde{t}, \tag{4.2}$$

which results in

$$\mathrm{d}n_{\text{parent}}\left(x,y,z,\tilde{t}\right)=\frac{\mathrm{d}F\left(x,y,z,\tilde{t}\right)}{\mathrm{d}z}\mathrm{d}\tilde{t}=-\sigma_{\text{dis}}F\left(x,y,z,\tilde{t}\right)n_{\text{parent}}\left(x,y,z,\tilde{t}\right)\mathrm{d}\tilde{t}. \tag{4.3}$$

The change in the total number of the parent ions after the photon flux $F\left(x,y,z,\tilde{t}\right)$ within $\mathrm{d}\tilde{t}$ passed through the trap is thus derived:

$$\begin{aligned}\mathrm{d}N_{\text{parent}}\left(\tilde{t}\right)&=\iint\mathrm{d}x\mathrm{d}y\int_0^{L_{\text{trap}}}\mathrm{d}z\;\mathrm{d}n_{\text{parent}}\left(x,y,z,\tilde{t}\right)\\&=-\sigma_{\text{dis}}\iint\mathrm{d}x\mathrm{d}y\int_0^{L_{\text{trap}}}\mathrm{d}z\;F\left(x,y,z,\tilde{t}\right)n_{\text{parent}}\left(x,y,z,\tilde{t}\right)\mathrm{d}\tilde{t}.\end{aligned} \tag{4.4}$$

Equation (4.4) was derived without any assumptions or approximation, which leads to a rigorous solution for $\mathrm{d}N_{\text{parent}}\left(\tilde{t}\right)$ once $F\left(x,y,0,\tilde{t}\right)$ and $n_{\text{parent}}\left(x,y,z,0\right)$ are given. However, the equation is difficult to solve analytically in its rigorous form. Therefore, we assume that the density of the parent ions is constant over the trap axis, i.e.,

$$n_{\text{parent}}\left(x,y,z,\tilde{t}\right)=n_{\text{parent}}\left(x,y,\tilde{t}\right), \tag{4.5}$$

which is a reasonable assumption because the absorbance thru the ion trap is extremely small in the present experimental conditions as will be described later. On this assumption, the photon flux is derived from Equation (4.1) as

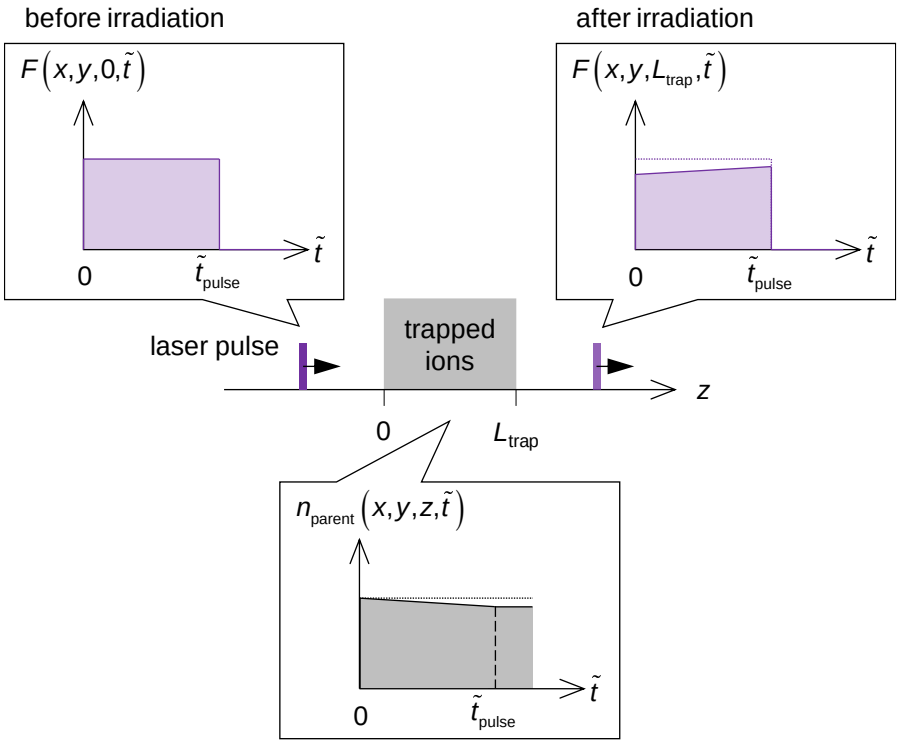

Figure 4.1. Illustration of $F\left(x,y,z,\tilde{t}\right)$ and $n_{\text{parent}}\left(x,y,z,\tilde{t}\right)$. Note that $\tilde{t}$ is a parameter for temporal intensity profiles of the laser pulse. The intensity decreases upon propagation along the trap axis. If the intensity is constant within the pulse width $\tilde{t}_{\text{pulse}}$ before irradiation (i.e., at $z = 0$), leading components of the laser pulse experience trapped ions with a higher density and become weaker than trailing components. $n_{\text{parent}}\left(x,y,z,\tilde{t}\right)$ is defined as the density of the parent ions that experiences the photon flux $F\left(x,y,z,\tilde{t}\right)$. Therefore, $n_{\text{parent}}\left(x,y,z,\tilde{t}\right)$ becomes lower at larger $\tilde{t}$ due to photodissociation.

$$F\left(x,y,z,\tilde{t}\right)=F\left(x,y,0,\tilde{t}\right)\exp\left(-\sigma_{\mathrm{dis}}n_{\mathrm{parent}}\left(x,y,\tilde{t}\right)z\right). \tag{4.6}$$

The change in the total number of the parent ions is thus obtained as

$$\begin{aligned}&\mathrm{d}N_{\mathrm{parent}}\left(\tilde{t}\right)\\&=-\sigma_{\mathrm{dis}}\iint\mathrm{d}x\mathrm{d}y\int_0^{L_{\mathrm{trap}}}\mathrm{d}z\;F\left(x,y,0,\tilde{t}\right)n_{\mathrm{parent}}\left(x,y,\tilde{t}\right)\exp\left(-\sigma_{\mathrm{dis}}n_{\mathrm{parent}}\left(x,y,\tilde{t}\right)z\right)\mathrm{d}\tilde{t}\\&=-\iint\mathrm{d}x\mathrm{d}y\;F\left(x,y,0,\tilde{t}\right)\left(1-\exp\left(-\sigma_{\mathrm{dis}}n_{\mathrm{parent}}\left(x,y,\tilde{t}\right)L_{\mathrm{trap}}\right)\right)\mathrm{d}\tilde{t},\end{aligned} \tag{4.7}$$

This equation is approximated further by the following equation on an assumption that the product $\sigma_{\mathrm{dis}}n_{\mathrm{parent}}\left(x,y,\tilde{t}\right)L_{\mathrm{trap}}\ll 1,$ which holds in the present experimental condition where typical values of $\sigma_{\mathrm{dis}}\sim 1$ Å^2, $n_{\mathrm{parent}}\left(x,y,\tilde{t}\right)\sim 10^7$ ions cm^{-3}, and L_{trap} = 40 cm:

$$\mathrm{d}N_{\mathrm{parent}}\left(\tilde{t}\right)=-\sigma_{\mathrm{dis}}\iint\mathrm{d}x\mathrm{d}y\;n_{\mathrm{parent}}\left(x,y,\tilde{t}\right)L_{\mathrm{trap}}F\left(x,y,0,\tilde{t}\right)\mathrm{d}\tilde{t}. \tag{4.8}$$

If the incident laser has a flat-top intensity profile, i.e.,

$$F\left(x,y,0,\tilde{t}\right)=\begin{cases}F_{\mathrm{flat}} & \left(x^2+y^2\le r_{\mathrm{flat}}^2,0\le\tilde{t}\le\tilde{t}_{\mathrm{pulse}}\right)\\ 0 & \left(\mathrm{otherwise}\right)\end{cases}, \tag{4.9}$$

where r_{flat} is the radius of the laser spot, the change in the total number of the parent ions becomes

$$\begin{aligned}\mathrm{d}N_{\mathrm{parent}}\left(\tilde{t}\right)&=-\sigma_{\mathrm{dis}}F_{\mathrm{flat}}\iint_{x^2+y^2\le r_{\mathrm{flat}}^2}\mathrm{d}x\mathrm{d}y\;n_{\mathrm{parent}}\left(x,y,\tilde{t}\right)L_{\mathrm{trap}}\mathrm{d}\tilde{t}\\&=-\gamma\sigma_{\mathrm{dis}}F_{\mathrm{flat}}N_{\mathrm{parent}}\left(\tilde{t}\right)\mathrm{d}\tilde{t}.\end{aligned} \tag{4.10}$$

The integration equals the number of the parent ions within the flat-top laser spot, $\gamma N_{\mathrm{parent}}\left(\tilde{t}\right)$, for an arbitrary ion-distribution profile, $n_{\mathrm{parent}}\left(x,y,\tilde{t}\right)$, where γ is a fraction of the irradiated ions to the total number of the trapped ions. Solving the above differential equation gives

$$N_{\mathrm{parent}}\left(\tilde{t}\right)=N_{\mathrm{parent}}\left(0\right)\exp\left(-\gamma\sigma_{\mathrm{dis}}F_{\mathrm{flat}}\tilde{t}\right)\quad\left(0\le\tilde{t}\le\tilde{t}_{\mathrm{pulse}}\right), \tag{4.11}$$

which derives the dissociation yield after the laser irradiation as

$$D = \frac{N_{\text{parent}}(0) - N_{\text{parent}}(\tilde{t}_{\text{pulse}})}{N_{\text{parent}}(0)} = 1 - \exp\left(-\gamma \sigma_{\text{dis}} F_{\text{flat}} \tilde{t}_{\text{pulse}}\right). \tag{4.12}$$

Therefore, the photodissociation cross section is expressed as

$$\sigma_{\text{dis}} = -\frac{\ln(1-D)}{\gamma F_{\text{flat}} \tilde{t}_{\text{pulse}}} \tag{4.13}$$

If the dissociation yield is sufficiently small, this equation is approximated by

$$\sigma_{\text{dis}} = \frac{D}{\gamma F_{\text{flat}} \tilde{t}_{\text{pulse}}} = \frac{\pi r_{\text{flat}}^2}{\gamma} \frac{D}{N_{\text{photon}}^{\text{in}}}. \tag{4.14}$$

where π is the circle ratio and $N_{\text{photon}}^{\text{in}} = F_{\text{flat}} \times \pi r_{\text{flat}}^2 \times \tilde{t}_{\text{pulse}}$ the number of the incident photons. This is the equation for evaluating photodissociation cross sections.

In the experiments, D and $N_{\text{photon}}^{\text{in}}$ in Equation (4.14) are measurable by an ammeter and a photodiode, respectively; the latter should be calibrated beforehand by a power meter. r is determined by an aperture. γ is evaluated by measuring the ion-distribution profile as follows. Prior to the measurements of the photodissociation spectra, dissociation yields were measured by scanning the laser position (x, y) at a constant laser power. The spot size, ~1 mm in diameter, was kept constant during the measurements. The result was Gaussian-like as shown in Figure 4.2. This one-dimensional result was converted to two-dimensional data of spatial distribution of ions by assuming a cylindrical symmetry. The numerical integration of the two-dimensional data inside the laser spot with linear interpolation between every data point gives the γ value.

Photodissociation spectroscopy is sensitive as explained as follows: the dissociation yield, D, defined by Eq. (4.12) is readily detectable, which can be as high as

about 10% in the present experimental condition with typical parameters of $\sigma_{\mathrm{dis}} \sim 1$ Å^2, $F_{\mathrm{flat}} \sim 10^{13}$ photons cm^{-2} ns^{-1}, $\tilde{t}_{\mathrm{pulse}} = 10\ \mathrm{ns\ pulse^{-1}} \times 10\ \mathrm{pulses} = 100\ \mathrm{ns}$, and $\gamma \sim 70\%$. On the other hand, the number of photons after irradiation is expressed as

$$N_{\mathrm{photon}}^{\mathrm{out}} = N_{\mathrm{photon}}^{\mathrm{in}} - DN_{\mathrm{parent}}(0). \tag{4.15}$$

This equation gives the decrease in the number of photons as follows:

$$\frac{N_{\mathrm{photon}}^{\mathrm{in}} - N_{\mathrm{photon}}^{\mathrm{out}}}{N_{\mathrm{photon}}^{\mathrm{in}}} = D\frac{N_{\mathrm{parent}}(0)}{N_{\mathrm{photon}}^{\mathrm{in}}}. \tag{4.16}$$

Typically, $D \sim 10\%$, $N_{\mathrm{parent}}(0) \sim 10^8$ ions, and $N_{\mathrm{photon}}{}^{\mathrm{in}} \sim 10^{13}$ photons result in $\frac{N_{\mathrm{photon}}^{\mathrm{in}} - N_{\mathrm{photon}}^{\mathrm{out}}}{N_{\mathrm{photon}}^{\mathrm{in}}} \sim 1.0\ \mathrm{ppm}$, which is extremely small to be detected by ordinary photoabsorption spectroscopy by means of transmission measurement.

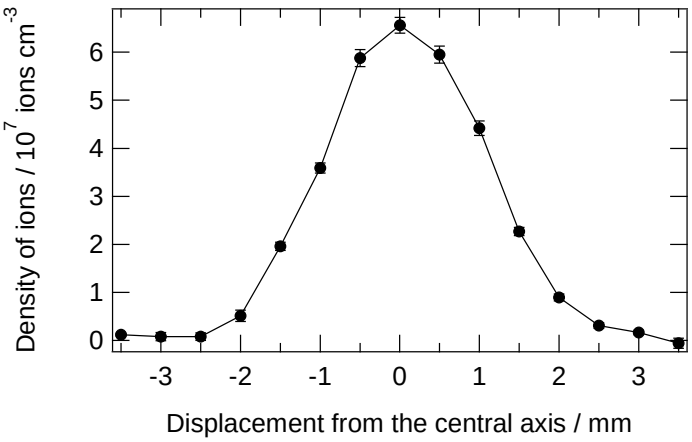

Figure 4.2. The spatial distribution measured for the silver trimer ions.

The explanation presented here is based on the assumption that the dissociation probability is unity, which does not hold in some cases (e.g., Ag_{16}^+, see Section 4.5). Therefore, photodissociation cross sections thus evaluated are lower limits of

photoabsorption cross sections. However, especially for smaller clusters, the assumption seems to hold well as discussed in Section 4.5, which allows us to adopt these photodissociation cross sections as measures for photoabsorption. The assumption will be confirmed as well by cavity ring-down spectroscopy presented in Chapter 5.

4.3. Experimental procedures

In the photodissociation spectroscopy, silver cluster cations Ag_N^+ generated by magnetron sputtering and size-selected by a quadrupole mass filter were loaded into the ion trap until a sufficiently large amount of cluster ions was stored, typically for several hundred milliseconds. The trapped ions were then thermalized for 500 ms by a buffer helium gas at room temperature and were irradiated by 10 shots of laser pulses. After the irradiation, the ions were additionally stored in the trap for 500 ms until dissociation was completed. The ions were finally extracted from the trap and transferred to the second mass filter to select only parent ions. After the mass selection, the ions were detected by the ammeter. The same procedure without laser irradiation was carried out. This set of measurements was repeated 10 times to obtain the number of the parent ions with and without laser irradiation along with the number of photons measured by a photodiode. A photodissociation cross section was evaluated from these measured values and the fraction of the irradiated ions evaluated beforehand. Repeated measurements as a function of photon energy of the laser, typically in the range of 2.8–5.0 eV, resulted in a photodissociation spectrum for one size of the silver cluster cations. In the present study, the photodissociation spectra were measured for almost every cluster size of N = 2–92. The incident laser power was always adjusted so that the photodissociation yield does not exceed 10% to satisfy the assumption of

Photodissociation cross sections were evaluated by substituting experimental data into Equation (4.14). The errors in the cross sections originate both from statistical and from systematic errors. The former was due to fluctuations in the numbers of the ions and the incident photons. Their standard deviations were converted to the standard errors by assuming that the central limit theorem holds true for these parameters. The total statistical error in a photodissociation cross section was derived from propagation of these standard errors, which is depicted as an error bar in the figures presented below. As for the systematic errors, uncertainty in the diameter of the laser spot is the major source. Let us assume a Gaussian profile for the spatial distribution of the trapped ions:

$$n_{\text{parent}}\left(x, y, \tilde{t}\right) = \frac{N_{\text{parent}}\left(\tilde{t}\right)}{\pi r_{\text{parent}}^2 \times L_{\text{trap}}} \exp\left(-\frac{x^2 + y^2}{r_{\text{parent}}^2}\right), \tag{4.17}$$

where r_{parent} is a parameter determining the width of the ion distribution. From Equation (4.17), the photodissociation cross section $\sigma_{\text{dis}}(2r_{\text{flat}})$ is expressed by Equation (4.14) with $\gamma = 1 - \exp\left(-\left(\frac{r_{\text{flat}}}{r_{\text{parent}}}\right)^2\right)$. Typically, $2r_{\text{flat}} \sim 2r_{\text{parent}} \sim 3$ mm in the present study. The photodissociation cross section simulated is depicted in Figure 4.3 as a function of diameter of the laser spot ($2r_{\text{flat}}$), which is normalized by the cross section at $2r_{\text{flat}} = 3$ mm. The cross section is overestimated if the laser diameter is overestimated because the photon flux is estimated to be lower than the real value. By assuming the uncertainty of ±0.5 mm in $2r_{\text{flat}}$, the uncertainty in the cross section is estimated to be about ±15%. The consideration presented here implies the possibility to reduce the systematic error by measuring the beam profile. An additional error would be caused by the approximation of $D \ll 1$ to derive Equation (4.14) from Equation (4.13). At $D = 10\%$, the cross section is underestimated by 5%, minor than the error caused by uncertainty in laser diameter.

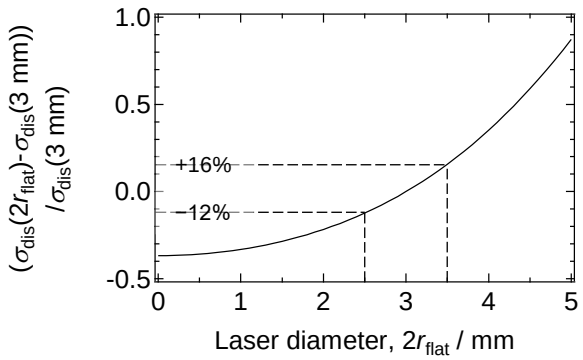

Figure 4.3. Estimation of the systematic error in the photodissociation cross section. $2r_{parent}$ was set to be 3 mm.

4.4. Photodissociation spectra of silver cluster cations

Photodissociation spectra of silver cluster cations measured for the size range of N = 2–92 are shown in Figures 4.4–4.7. Note that the ordinate shows "multi-photon dissociation yield" (see Section 4.5) instead of cross sections for N = 19 and above, where multi-photon processes are observed as will be discussed in Section 4.5. One of the characteristic features of the present photodissociation spectra is a concentration of absorption bands in a narrow spectral range at larger sizes. For example, $Ag_{4,6,11,12}^+$ showed multiple bands over the entire spectral range of 2.8−5.0 eV, while absorption bands were located in 3.6–4.1 eV range at the sizes larger than 19. This feature reminds us of collective excitation of electrons although quantitative measurements of absolute cross sections are necessary to discuss the collectivity for $N \geq 19$. Firstly, the present results are compared with those in the previous studies in this section.

Ag_2^+. The dimer showed only one band at 3.01 eV, which was observed by a previous report [37] as well. The band is identical to the previous data both in the band shape and in the cross sections. A tail toward the lower-energy side is interpreted as hot

bands as discussed in the previous report. The present study extended the spectral range of the measurement from 2.8–3.1 eV of the previous report to 2.4–5.0 eV; a spectrum covering such a wide energy range was measured for the first time. However, no other bands were observed except for that around 3.01 eV.

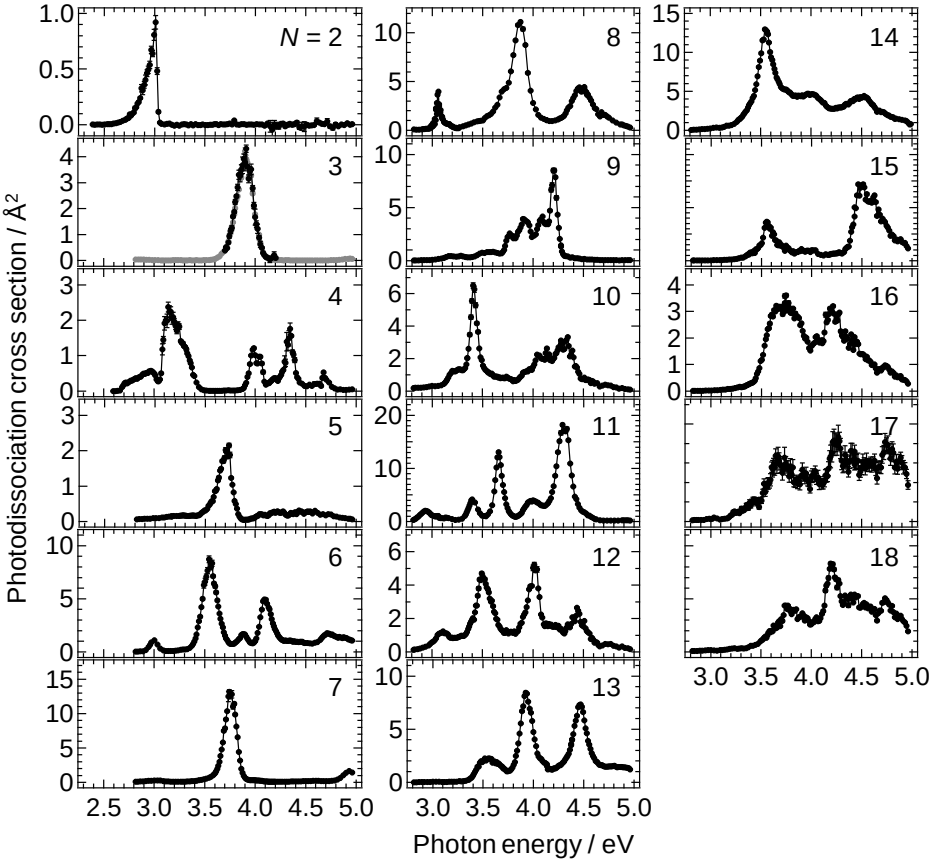

Figure 4.4. Photodissociation spectra of Ag_N^+ (N = 2–18). The error bars denote statistical errors. The clusters dissociated upon one-photon absorption in the entire photon-energy range except for N = 15, 17, and 18. Note that the spectra of N = 15, 17, and 18 are shown on the assumption that they dissociated by one-photon absorption, although two-photon processes contributed as well in the low energy region. As for the black and gray plots in the spectrum of N = 3, see the text for explanation.

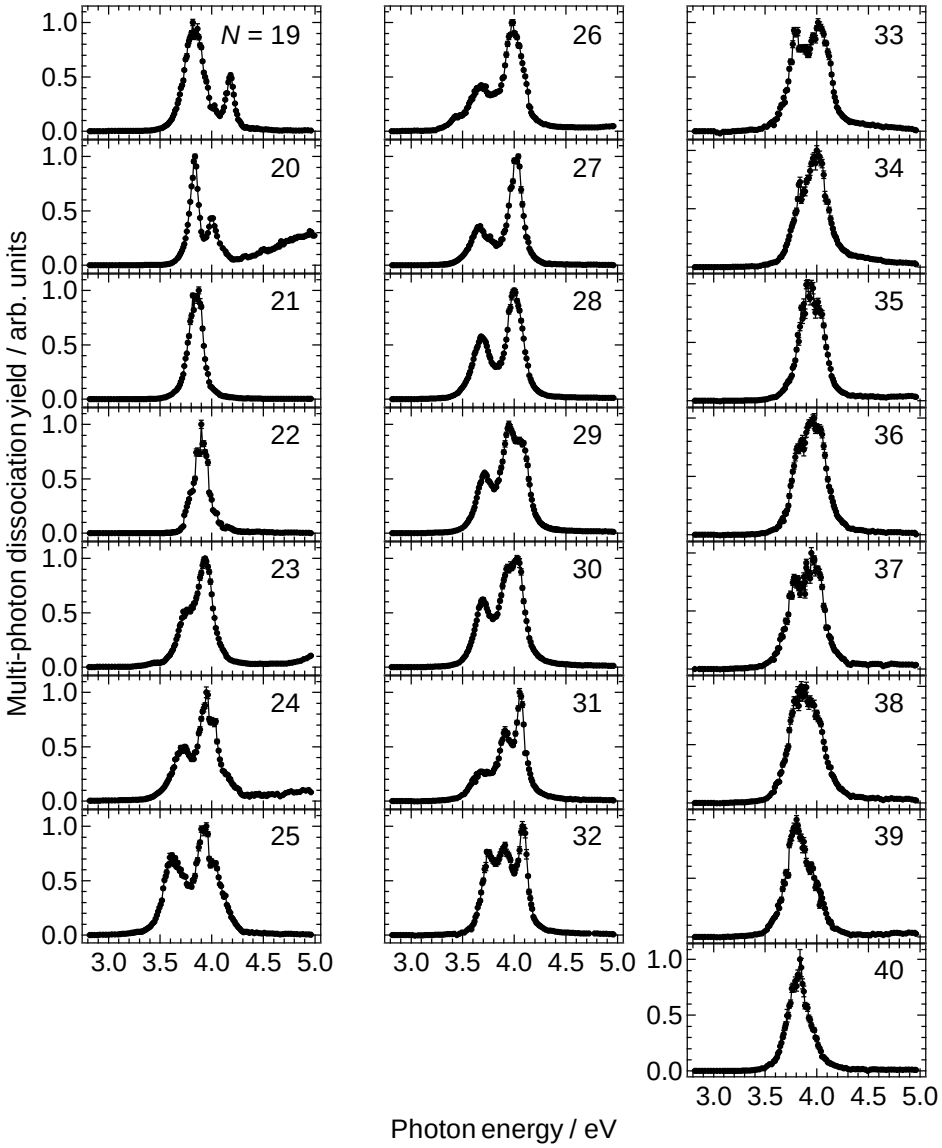

Figure 4.5. Photodissociation spectra of Ag_N^+ (N = 19–40), which dissociated via two-photon absorption.

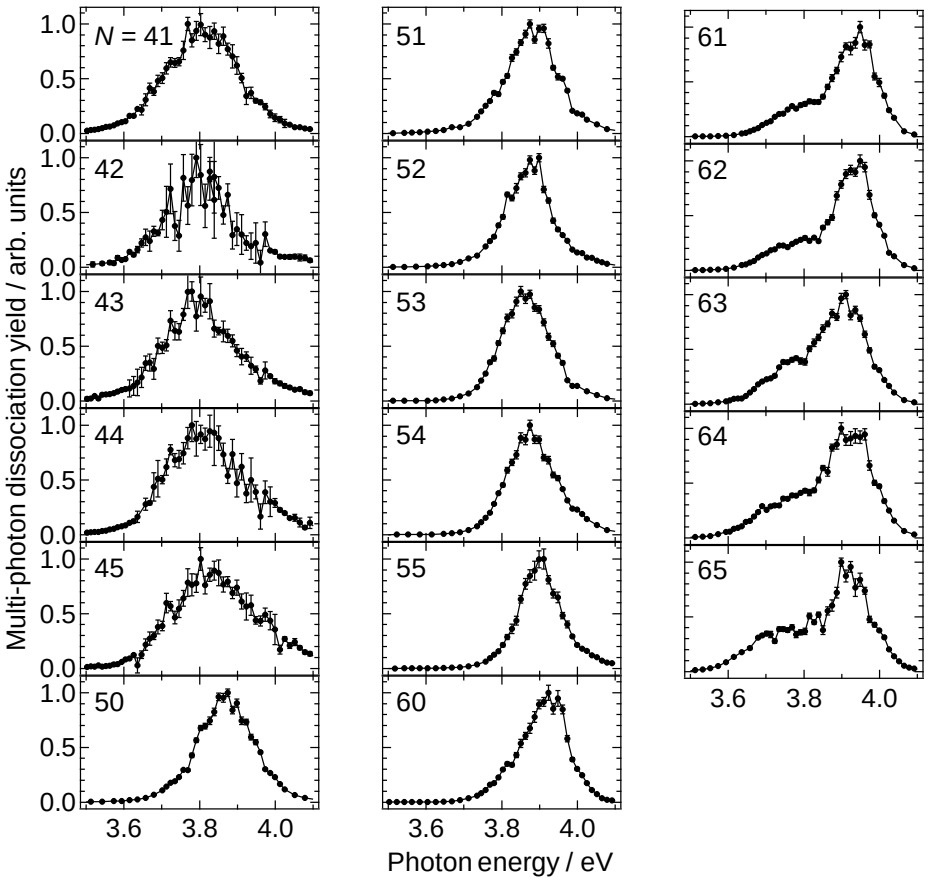

Figure 4.6. Photodissociation spectra of Ag_N^+ (N = 41–65). The clusters with sizes of 41–55 dissociated upon three-photon absorption, while those with N = 60–65 showed dissociation upon four-photon absorption. The spectra of N = 42–45 were obtained by five times of measurements, which resulted in larger statistic errors than those in the other sizes measured 10 times. Note that the spectral range of the measurement is narrower than that for $N \leq 40$.

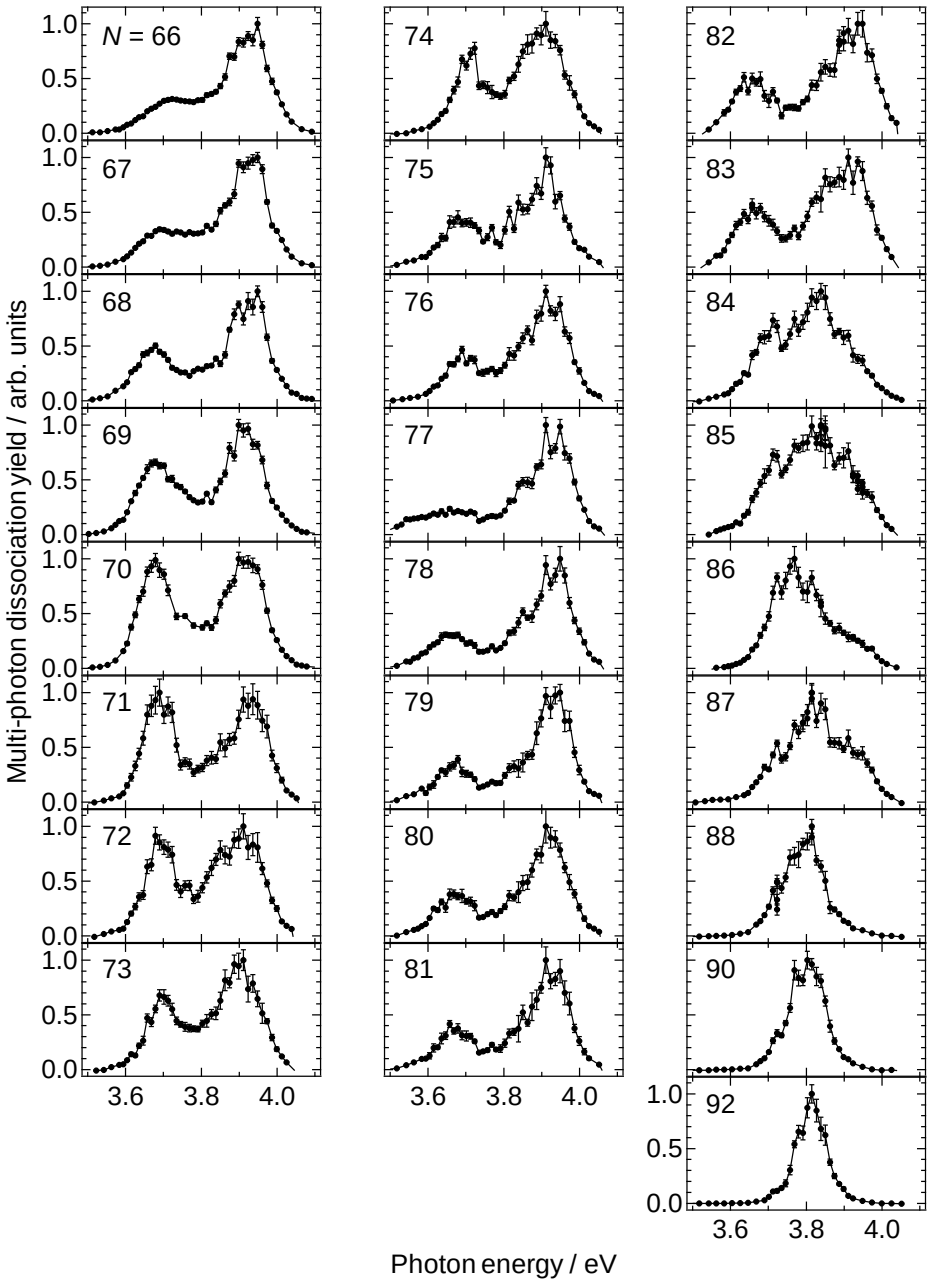

Figure 4.7. Photodissociation spectra of Ag_N^+ ($N = 66$–92), which dissociated upon five-photon absorption.

Ag_3^+. In Figure 4.4, two sets of data are plotted; black circles are measured in a limited energy range with accurate estimation of the laser diameter, while gray circles cover a wider energy range but with some uncertainty in the laser diameter. Therefore, the latter spectrum was scaled so that the cross section coincides with that of the former; the profiles of both the spectra were confirmed to be completely identical. The two complementary spectra thus elucidate that the silver trimer cation exhibits only one band at about 3.9 eV in the energy range of 2.8–5.0 eV. Such a spectral feature reminds us of the equilateral-triangular structure of the trimer. See Chapter 6 for more details.

Ag_4^+. The photodissociation spectrum of the cationic silver tetramer was previously measured by Terasaki et al. [40]. The present spectrum matches well with the previous data in view of their profiles and cross sections. A slight difference between them is in the profiles of the absorption band at 3.14 eV: it shows a rather sharp profile in the previous study, while the intensity decreases slowly toward the higher energy side in the present study. The reason for this difference is currently unclear. The absorption spectrum was also measured for the corresponding rare-gas complexes of $Ag_4Kr_2^+$ and $Ag_4Kr_3^+$ by Rayner et al. [33], showing only one band around 3 eV in the spectral range of 2.5–5.0 eV, which is different from the present result. This might be due to the Kr adatoms: krypton accounts for 33% or 43% of the constituent atoms of the cluster. Due to the large polarizability of krypton, perturbation to the electronic state of the cationic silver tetramer would not be negligible.

Ag_8^+. One absorption band was previously observed by Ito for the cationic silver octamer [35], where the spectral range was limited to 3.70–4.35 eV due to the light source employed. The present study with an extended spectral range revealed three absorption bands. The band at 3.87 eV was identical to that observed by Ito. The other

bands observed for the first time in this study make geometry assignment clearer as will be shown in Chapter 6.

Ag_9^+. Ag_9^+ is one of the magic clusters because it is regarded as an eight-valence-electron system based on the electronic shell structure of metal clusters [51]. Tiggesbäumker et al. examined the absorption spectrum of Ag_9^+ in this context [30–32]. The spectrum exhibited a single band located at 4.02 eV, which is extremely different from the present photodissociation spectrum of Ag_9^+ showing a multi-modal profile as observed by Ito [35] who also employed an ion trap. The difference is explained by several groups [33–35]; the temperature of Ag_9^+ prepared by Tiggesbäumker et al. was estimated to be about 2000 K. In that case, Ag_9^+ is regarded as in a liquid phase, which enables the application of the jellium model to the cluster according to Rayner et al. [33]. However, there are several questions about the explanation by Rayner et al.; firstly, the motion of electrons is much more rapid than that of the nuclei. Therefore, the electrons in the cluster experience some ionic background depending on the geometric structure of the cluster at the moment of photoabsorption, not the jellium-like potential necessarily. Secondly, even if the potential for the valence electrons is regarded as the jellium potential, the excitations are just described by linear combinations of individual transitions between superatomic orbitals. If an excitation is dominated by one transition between superatomic orbitals, it is not collective. The result of Tiggesbäumker et al. just indicates that the absorption band of Ag_9^+ at 4.02 eV possesses 94% of the oscillator strength originating from the valence electrons in their experimental condition, of which systematic error was estimated to be 50% [30, 32]. The present result rather resembles an absorption spectrum of Ag_9^+ measured by cavity ring-down spectroscopy by Terasaki et al. [36], a photodissociation spectrum by Ito [35], and of Ag_9Kr^+ measured by Rayner

et al. [33, 34] both in spectral profiles and in absorption cross sections. It is natural to speculate that the difference between the spectral profile in the present study and that measured by Tiggesbäumker et al. is ascribed to a thermal effect as pointed out by Moseler et al. [43] and Ito [35]; just vibrationally excited clusters and coexistent geometric isomers seem to be contributing in the previous report of Tiggesbäumker et al. Moreover, their oscillator strengths would probably have been overestimated by considering the systematic errors in their report, which results in the difference in absorption cross sections between the present and the previous reports. The present result is rather identical with the photodissociation spectrum measured by Lindinger et al. [52] in the spectral profile, although the present cross sections are larger than their report. However, quantitative comparison of cross sections is difficult because they do not mention the accuracy of their cross sections in [52].

Ag_{10}^+. There is only one study on the photoabsorption spectrum of Ag_{10}^+ [35], where a structureless spectrum was observed in the spectral range of 3.70–4.35 eV, which is a part of the absorption band around 4.3 eV observed in the present study. Moreover, a sharp absorption band at 3.41 eV was detected for free Ag_{10}^+ for the first time in this study. The corresponding Kr complex, $Ag_{10}Kr^+$, exhibited a similar spectrum [33], which reflects the fact that perturbation of the krypton adatom on the cluster is less significant at this size.

Ag_{11}^+. There are two studies on the photoabsorption spectrum for $N = 11$. The photodissociation spectrum measured by Tiggesbäumker et al. is characterized by two broad Lorentzian-like absorption bands located at 3.44 and 4.22 eV with full widths at half maximum (FWHM) of 0.30 and 0.87 eV, respectively [30, 31]. These spectral features are different from those of the present spectrum, where five bands were observed

at 2.93, 3.40, 3.66, 4.00, and 4.29 eV. Among them, the bands at 3.66 and 4.29 eV show large oscillator strengths. However, these bands were absent in the previous study. Probably, isomers other than those possessing large oscillator strengths at 3.44 and 4.22 eV were substantially populated in their experimental condition with a high internal temperature, which led to the ensemble-averaged spectrum qualitatively described by the ellipsoidal shell model [42, 53]. On the other hand, the present photodissociation spectrum is similar to that measured by Ito [35] in its profile; the present photodissociation cross sections reproduced those measured by Ito within the present systematic error (see Section 4.3 for details).

Ag_{12}^+. Four bands were observed in the present study. Among them, a band located at 4.01 eV reproduced the only one previous report on the photoabsorption on pure cationic silver dodecamer [35] both in profiles and quantitative cross sections within systematic errors. Comparison with a previous study on $Ag_{12}Kr^+$ [33] provides an important insight, where the absorption bands are sharper than those in the present study, showing even splitting into multiple bands. This difference originates from the temperature; the previous spectrum of $Ag_{12}Kr^+$ was measured at 100 K, resulted in removing hot bands observed in the present study.

Ag_{13}^+. There is only one spectrum available for Ag_{13}^+ [35], which shows a single band centered at 3.91 eV. The band was quantitatively reproduced by the present study. Moreover, additional two bands were found at 3.55 and 4.48 eV out of the previous spectral range.

Ag_{14}^+. A structureless photodissociation spectrum was reported previously in an energy range of 3.70–4.35 eV [35]. The present result clearly shows three maxima in an extended spectral range; the band in the previous report was reproduced well.

$Ag_{15,17,18}^+$. $N = 15$ showed two bands located at ~3.6 and 4.5 eV, while $N = 17$ and 18 exhibited broad bands over the energy range of ~3.5–5.0 eV. However, these profiles do not reflect actual profiles of their photoabsorption spectra because two-photon processes as well as one-photon dissociation contribute to the action spectrum depending on the photon energy (see more details in Section 4.5). Among these clusters, a photodissociation spectrum of Ag_{15}^+ was reported by Tiggesbäumker et al. previously [30]; a sharper band and a more intense and broader band were observed at 3.46 and 4.07 eV, respectively. Although the internal energies were different, the latter would correspond to the band at 4.5 eV observed in the present study. The intense absorption around 4.07 eV in their spectrum would not result in dissociation due to insufficient photon energy for the present experiment where cooling by the buffer helium gas competes with dissociation processes, while the absorption around 4.5 eV provides sufficient energy for Ag_{15}^+ to dissociate (see Section 4.5). To record photoabsorption spectra of such sizes where one- and two-photon processes compete, some other techniques may be available, e.g., by cavity ring-down spectroscopy that does not rely on the action of dissociation.

Ag_{19}^+. $N = 19$ is a characteristic size where photoabsorption started to converge into a specific photon energy. Tiggesbäumker et al. measured the photodissociation spectrum for this size. However, the spectral profile was not reported. They only mentioned the average resonance energy of 3.97 eV [32]. The photodissociation spectrum of $N = 19$ was reported in this thesis for the first time. The spectral profile will be interpreted by considering the geometric structure of the cluster in Section 4.6.

Ag_{21}^+. $N = 21$ is a notable size because it is regarded as 20-valence-electorn closed-shell system based on the electronic shell structure of metal clusters [51]. In this

context, Tiggesbäumker et al. reported its photodissociation spectrum [30–32], where a single Lorentzian is centered at 3.82 eV with FWHM of 0.56 eV and maximum intensity of 8.84 Å^2. The single band was observed as well in the present study at the same transition energy. However, a difference is in its width, which is as narrow as 0.16 eV in FWHM in the present spectrum. The origin of this difference is the two-photon dissociation process observed in the present study as described in Section 4.5; the ordinate of the spectrum qualitatively corresponds to the product of the sequential absorption cross sections, which results in the sharper spectrum. Ag_{21}^+ has been regarded to exhibit collective excitation of electrons so far in view of the fact that 64% of the valence electrons contributes to the observed absorption [30–32]. Quantitative analysis of the oscillator strength is difficult for the present photodissociation spectrum. However, the single-band profile observed in this study brings an important insight into the electronic excitation; the profile is explained by a number of locally pseudodegenerate excitations originating from a single geometric isomer, as will be mentioned in Chapter 6. Although further analysis is necessary, this feature implies collectivity in the electronic excitation of Ag_{21}^+.

Comparison with neutral and anionic silver clusters. There is no data available for photoabsorption spectra of silver cluster cations, Ag_N^+ (N = 5–7, 16–20, 22 and above). However, those of neutral and anionic counterparts were reported by several groups. Harbich and coworkers reported photoabsorption spectra of neutral silver clusters with the sizes of 1–120 in various rare-gas matrices [54–58]. Simply speaking, absorption spectra of Ag_N are much different from those of cations for $N < 16$, while they are similar to each other in their profiles for $N \geq 16$. For example, Ag_{35} showed a central absorption energy of 3.84 eV in their study. To compare this resonance

energy with that of the present result of the gas-phase cationic counterpart, the absorption energies in the neon matrix were blue-shifted by 0.17 eV to remove a dielectric effect of the matrix [54, 60]; it is expected that Ag_{35} shows an absorption maximum at 4.01 eV in the gas phase, which is close to that of the present result of Ag_{35}^+ at 3.95 eV. Profiles of the previous absorption spectra of $Ag_{55,84,92}$ embedded in the neon matrix are similar to photodissociation spectra of the cationic counterparts in the present study. However, the resonance energies in the previous study were 3.90, 3.77, and 3.80 eV, which corresponds to the energies of 4.07, 3.94, and 3.97 eV in a vacuum, respectively; the energies are somewhat different from those of the present study, i.e., 3.90, 3.83, and 3.81 eV for Ag_{55}^+, Ag_{84}^+, and Ag_{92}^+, respectively. As for the anions, Ag_N^-, Tiggesbäumker et al. reported broad Lorentzian-like spectra for $N = 7$, 9, 11, 13, 15, 17, and 19 [27, 29]. Among them, Ag_7^- and Ag_{19}^- showed single-band profiles with FWHM of 0.88 and 0.61 eV, respectively, while the others exhibited double-band profiles. Compered with these results, the present study of cations showed rather multi-modal profiles for $N \leq 13$, which is due to the difference in internal energies of the clusters as mentioned above. The photodestruction spectra for Ag_N^- (N = 3–19) were reported recently [41], where the spectral profiles were completely different from the present results for cations. A recent report on electron detachment cross sections of Ag_{91}^- showed a Lorentzian located at 3.74 eV [59]; although the resonance energy of Ag_{91}^- is different from that of Ag_{92}^+ in the present study, the profiles are similar to each other.

To summarize, the spectral shapes of neutral and cationic silver clusters become similar to each other above the size of 16. The spectral profile of Ag_{91}^- is also similar to that of Ag_{92}^+. From these considerations, it is inferred that the influence of the charge state is less important above the size of ~20, despite lack of data for anions in the $N = 20$–

30 range.

4.5. Dissociation processes

For evaluation of photodissociation cross sections, it is necessary to understand photodissociation processes. A photoabsorbed molecule undergoes various relaxation paths as mentioned in Section 4.3. Especially, dissociation after photoabsorption and deexcitation by collision with a buffer gas are major paths on an assumption of rapid internal conversion and no contribution of radiative paths to deexcitation. Qualitatively, if dissociation were the only pathway that a cluster undergoes, all the clusters would dissociate after laser irradiation. However, in an ion trap, the cluster is cooled via collision with the buffer helium gas. Therefore, it does not dissociate by one-photon absorption when its internal energy after one-photon absorption is not as high as the dissociation rate exceeds the cooling rate; the cluster needs to absorb additional photons for dissociation, which leads to multi-photon processes. If clusters dissociate upon two-photon absorption, i.e., excitation of clusters by the first photon is followed by dissociation upon absorption of the second photon, the first process corresponds to the absorption cross section expressed by Equation (4.14):

$$\sigma_1 = \frac{\pi r_{\mathrm{flat}}^2}{\gamma_1 N_{\mathrm{photon}}^{\mathrm{in}}} \frac{N_{\mathrm{exc}}}{N_{\mathrm{parent}}}. \tag{4.18}$$

and the second one gives the photodissociation cross section of

$$\sigma_{\mathrm{dis}} = \frac{\pi r_{\mathrm{flat}}^2}{\gamma_2 N_{\mathrm{photon}}^{\mathrm{in}}} \frac{N_{\mathrm{dis}}}{N_{\mathrm{exc}}}. \tag{4.19}$$

where N_{exc} is the number of excited clusters upon photon absorption, N_{parent} that of parent ions inside the ion trap, N_{dis} that of dissociated clusters (or a decrease in that of the parent

ions), N_{photon} that of incident photons, and γ_1 and γ_2 fractions of the parent and excited ions irradiated by a laser beam, respectively. The number of the excited clusters cannot be measured. However, a product of

$$\sigma_1\sigma_{\mathrm{dis}} = \frac{N_{\mathrm{dis}}}{\gamma_1\gamma_2 N_{\mathrm{parent}}}\left(\frac{\pi r_{\mathrm{flat}}^2}{N_{\mathrm{photon}}^{\mathrm{in}}}\right)^2 = \frac{D}{\gamma_1\gamma_2}\left(\frac{\pi r_{\mathrm{flat}}^2}{N_{\mathrm{photon}}^{\mathrm{in}}}\right)^2 \tag{4.20}$$

is expressed by the measurable quantities. Generally, when clusters dissociate upon M-photon absorption, a product of

$$\sigma_1\sigma_2\cdots\sigma_{M-1}\sigma_{\mathrm{dis}} = \frac{D}{\gamma_1\gamma_2\cdots\gamma_M}\left(\frac{\pi a^2}{N_{\mathrm{photon}}}\right)^M \tag{4.21}$$

is a measure of photoabsorption practically available. This product is referred below as a "multi-photon dissociation yield," D', for $M \geq 2$ because it is proportional to a dissociation yield $D = N_{\mathrm{dis}}/N_{\mathrm{parent}}$ divided by the M-th power, $N_{\mathrm{photon}}{}^M$, of the number of incident photons. The above equation is rearranged as follows:

$$\log D = M\log N_{\mathrm{photon}} + \text{const.}, \tag{4.22}$$

which implies that the value of M is derived from a slope of a double logarithmic plot of photodissociation yields as a function of the number of incident photons.

The plots are shown in Figure 4.8, while M values determined by fitting are shown in Table 4.1 with the photon energies of the incident photons in the experiments; the energies at absorption maxima were chosen for each cluster size. Generally speaking, dissociation yields increased drastically as a function of laser intensity for larger clusters; the smaller clusters with the sizes of 8 and 14 showed dissociation upon one-photon absorption, while Ag_{30}^+ and Ag_{40}^+ exhibited two-photon absorption to dissociate. The largest clusters in the experiments, Ag_{66}^+ and Ag_{92}^+, dissociated upon even five-photon absorption. This behavior, i.e., emergence of photodissociation upon multi-photon

absorption at higher sizes, is explained based on the RRK theory [44–46]; as the number of the vibrational modes increases at larger sizes, the dissociation rate decreases exponentially. Clusters with larger sizes must absorb another photon to dissociate.

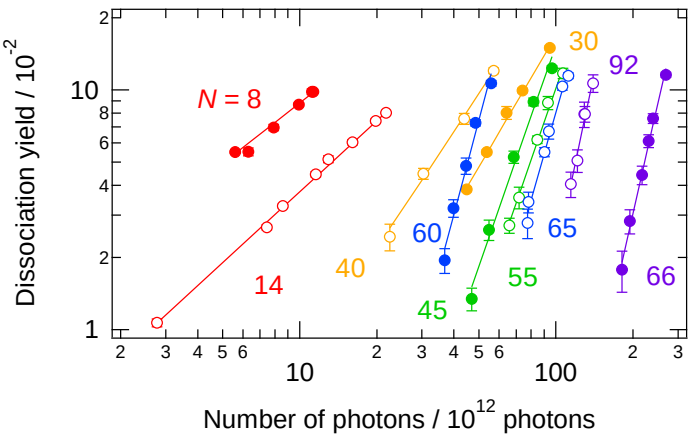

Figure 4.8. Dissociation yields measured for silver cluster cations, Ag_N^+, as a function of the number of incident photons. The solid regression lines were determined by fitting the experimental data to the power law by employing the least squares method.

Table 4.1. The M values obtained for Ag_N^+ clusters along with the photon energies of the incident photons employed in the measurements.

N	M	Photon energy / eV	N	M	Photon energy / eV
8	1	3.87	55	3	3.90
14	1	4.49	60	4	3.87
30	2	4.03	65	4	3.87
40	2	3.80	66	5	3.92
45	3	3.87	92	5	3.81

It is noteworthy to mention experimental results of Ag_{18}^+ in Figure 4.9. Dissociation yields were measured as a function of the number of incident photons at the photon energies of 3.78, 4.00, and 4.43 eV. The slopes of the regression lines are different from each other; dissociation yields increased more drastically in data with a lower photon energy than those in a higher energy. Moreover, the values of the slopes were between one and two, i.e., not integers. This behavior was also recognized for Ag_{15}^+ and Ag_{17}^+. The result indicates that both one-photon and two-photon absorption contribute to photodissociation. When clusters absorb the first photon, its dissociation rate is moderate; some clusters dissociate before absorbing second photons, while others remain as they are until dissociation occurs upon second-photon absorption. If the photon energy is lower, one-photon absorption yields a smaller dissociation rate because of a smaller internal energy. Therefore, dissociation upon two-photon absorption is slightly major. On the other hand, the internal energy gained by absorption of even a single photon at a higher photon energy brings a higher dissociation rate, which makes dissociation upon one-photon absorption rather major. Because of this complexity, the photodissociation spectra of sizes of 15, 17, and 18 should be interpreted carefully.

Furthermore, a simulation was performed to explain the size- and photon-energy-dependent multi-photon processes. Suppose that clusters photoexcited at the time origin follow two pathways, i.e., dissociation followed by rapid internal conversion and intramolecular vibrational energy redistribution (IVR), or deexcitation by the buffer gas. The density of the clusters at time t, $n_{\mathrm{parent}}(t)$, follows the differential equation of

$$\frac{\mathrm{d}n_{\mathrm{parent}}(t)}{\mathrm{d}t} = -k_{\mathrm{dis}}(t)\,n_{\mathrm{parent}}(t), \tag{4.23}$$

where $k_{\mathrm{dis}}(t)$ is the time-dependent decay rate. For the non-infinitesimal simulation time step Δt, the equation is transformed to

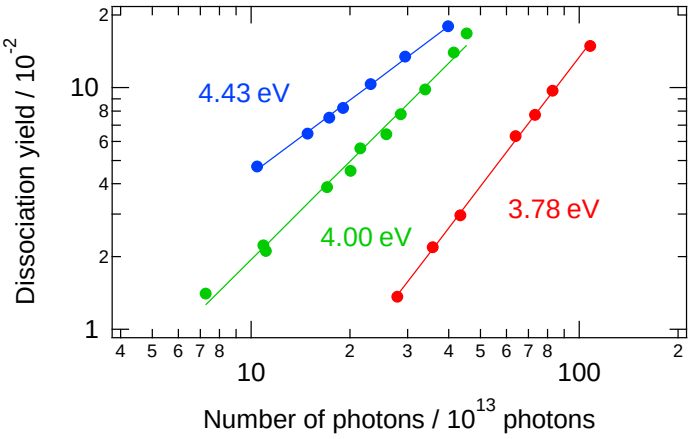

Figure 4.9. Dissociation yields of Ag_{18}^{+} measured as a function of the number of incident photons at different photon energies. The solid regression lines were determined by fitting to the experimental data to the power law by employing the least squares method.

$$\Delta n_{\text{parent}}(t) = -k_{\text{dis}}(t)\, n_{\text{parent}}(t)\, \Delta t. \tag{4.24}$$

The decay rate is represented by referring to the RRK theory [44–46],

$$k_{\text{dis}}(t) = \begin{cases} \nu\left(1 - \dfrac{E_0}{E_{\text{tot}}(t)}\right)^{s-1} & \left(E_0 \le E_{\text{tot}}(t)\right), \\ 0 & (\text{otherwise}) \end{cases} \tag{4.25}$$

where ν is the frequency pre-factor, $E_{\text{tot}}(t)$ the total energy, E_0 the dissociation energy, $s = 3N - 5$ (for a linear cluster, i.e., the dimer) or $3N - 6$ (for the others) the number of the vibrational modes, and N the cluster size. The frequency pre-factor was assumed to be the Debye frequency of the bulk silver, 4.48×10^{12} Hz [47]. The dissociation energy was cited from the previous report by Krückeberg et al. [50]. The cooling effect by the buffer helium gas is expressed as the time-dependent total energy

$$E_{\text{tot}}(t) = \begin{cases} sk_{\text{B}}T_{\text{buffer}} + h\nu \equiv sk_{\text{B}}T_{\text{parent}}(0) & (t = 0) \\ sk_{\text{B}}T_{\text{parent}}(t) & (t > 0) \end{cases} \tag{4.26}$$

by assuming one-photon absorption, where $T_{\mathrm{buffer}} = 300$ K is the temperature of the buffer helium gas, $T_{\mathrm{parent}}(t)$ that of the clusters that follows the time-dependence of

$$T_{\mathrm{parent}}(t) = \left(T_{\mathrm{parent}}(0) - T_{\mathrm{buffer}}\right)\left(1 - \frac{K}{3Nk_{\mathrm{B}}}\right)^{\frac{t}{t_{\mathrm{collision}}}} + T_{\mathrm{buffer}}, \tag{4.27}$$

k_{B} the Boltzmann constant, hv the photon energy, K the energy exchange constant set to be 4.5 μeV K^{-1} by referring to a previous molecular dynamics study on Pd_{13} [48], and $t_{\mathrm{collision}}$ the interval of collisions between the clusters and the buffer gas. The interval was obtained as a reciprocal of the Langevin rate constant

$$k_{\mathrm{Langevin}} = \sqrt{\frac{\pi\alpha_{\mathrm{buffer}}e^2}{\varepsilon_0\mu}}n_{\mathrm{buffer}}, \tag{4.28}$$

where $\alpha_{\mathrm{buffer}} = 1.38\ a_0^3$ the polarizability volume of the buffer helium [49], a_0 the Bohr radius, e the elementary charge, ε_0 the vacuum permittivity, $\mu = \frac{m_{\mathrm{parent}}m_{\mathrm{buffer}}}{m_{\mathrm{parent}} + m_{\mathrm{buffer}}}$ the reduced mass, m_{parent} the mass of the cluster, m_{buffer} that of the buffer-gas atom, $n_{\mathrm{buffer}} = \frac{p_{\mathrm{buffer}}}{k_{\mathrm{B}}T_{\mathrm{buffer}}}$ the density of the buffer gas, and $p_{\mathrm{buffer}} = 0.1$ Pa the pressure of the buffer. The dissociation probability is derived by solving Equations (4.24)–(4.28).

The results of the simulation for $Ag_{8,16,19}^+$ are depicted in Figure 4.10. The photon energies were set to be those at absorption maxima in the present photodissociation spectra. Ag_8^+ decays rapidly via dissociation with a lifetime as short as 35 ns, while its internal energy is constant in that time window. This result is consistent with the present experiment, where Ag_8^+ dissociated by one-photon absorption. This simulation indicates that the smaller clusters dissociate by one-photon absorption because the absorbed photon energy is easily concentrated to a specific vibrational mode leading to dissociation. As for Ag_{19}^+, its decay rate is extremely low due to a large

number of vibrational modes; the internal energy becomes lower than the dissociation energy within 92 ms before dissociation, which is consistent with the fact that Ag_{19}^+ dissociated by two-photon absorption. On the other hand, Ag_{16}^+ shows an intermediate behavior between the two sizes. It dissociates rapidly just after the laser irradiation. However, the dissociation is terminated at $t \sim 10$ ms due to decreases in the internal energy and dissociation rate. The internal energy becomes lower than the bond dissociation energy at 97 ms. The population of the parent ions becomes 24% finally; the dissociation probability is thus estimated to be 76%. Although the estimation described above is qualitative, it explains the reason for the low photodissociation cross section observed for Ag_{16}^+: such incomplete dissociation results from comparable rates for dissociation and buffer-gas cooling. Note that photodissociation cross sections underestimate photoabsorption cross sections in such cases. The simulation was performed further for Ag_{15}^+ as shown in Figure 4.11. The parent ions do not dissociate at the photon energy of 3.55 eV, while 64% of the parent ion dissociate at the photon energy of 4.50 eV. This result is consistent with the fact that Ag_{15}^+ showed dissociation upon one-photon absorption at higher photon energies and that upon two-photon absorption at lower photon energies. As a result of the present simulation and photodissociation spectroscopy, N = 15–18 are critical sizes for emergence of multi-photon processes. The reason why only Ag_{16}^+ showed one-photon dissociation (with a low dissociation probability) among them would be because it is bound more weakly than the others; the bond dissociation energy of Ag_{16}^+ is reported to be 2.05 eV, which is lower than those of $Ag_{15,17,18}^+$ by 0.3–0.5 eV [50].

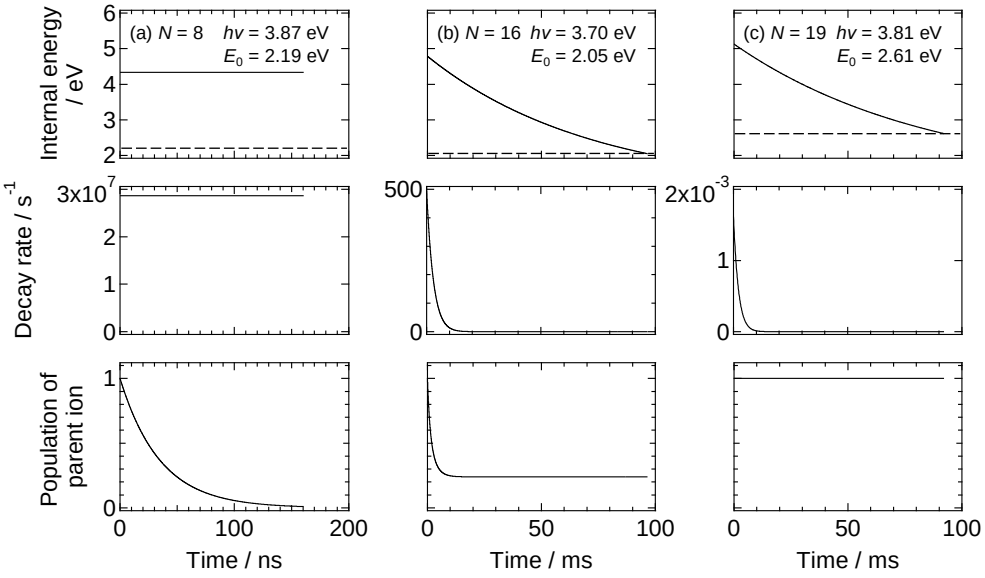

Figure 4.10. The simulated internal energies, decay rates, and the population of the parent ions, Ag_N^+, as a function of time. The dashed lines indicate the bond dissociation energies E_0 [50]. $T_{\text{parent}}(0) = 2795$, 1322, and 1167 K for $N = 8$, 16, and 19, respectively.

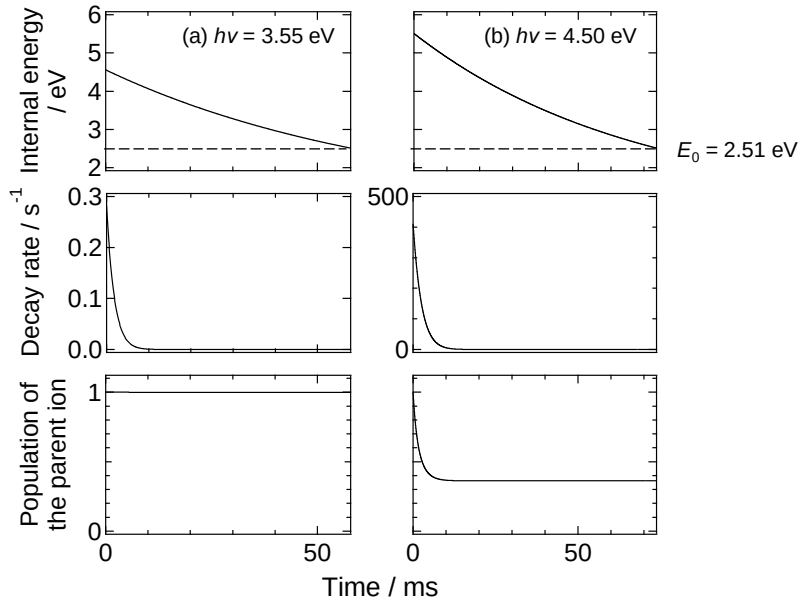

Figure 4.11. The simulated internal energy and the population of the parent Ag_{15}^+ as a function of time. The dashed lines indicate the bond dissociation energy E_0 [50]. $T_{\text{parent}}(0) = 1356$ and 1639 K for panels (a) and (b), respectively.

4.6. Discussion

Now the discussion will focus on the larger size range dominated by multi-photon dissociation, where the spectral profile exhibits a few features depending on the cluster size above $N = 19$. As shown in Figure 4.5, $Ag_{19,20}^+$ showed double-band profiles where the bands at a lower energy was more intense than that at a higher energy. On the other hand, $Ag_{21,22}^+$ exhibited single-band profiles. Ag_N^+ ($N = 23$–33) presented double-band profiles, where the band at a higher energy was more intense, except for $N = 26$, 31, and 32 exhibiting triple-band profiles. The clusters showed single-band profiles again at the size above 34 up to 60 with a blueshift of the absorption band, which was located around 3.9 eV at $N = 60$. At $N = 61$, an absorption band redshifted to ~3.8 eV, which became more intense with respect to intensity of the absorption band at the higher energy and redshifted further to ~3.7 eV as the cluster grew into larger sizes; the two bands showed the same intensity at $N = 71$. The absorption band at the lower energy became weaker from $N = 72$ to 77 and again stronger from $N = 78$ to 83. The two bands converged into ~3.8 eV showing a broad band width above $N = 84$, which resulted in a single band of Ag_{92}^+ with a sharp band width. Such a change in the spectral profiles would result from geometries dependent on the cluster size; according to Schmidt et al. [1], when the cluster is regarded as a spheroid,

$$R_{\text{radius}} = R_{\text{energy}}, \tag{4.29}$$

where R_{radius} is the ratio of the radius along the symmetry axis to the radius perpendicular to the axis, R_{energy} the ratio of the resonance energies of the more intense band to that of the weaker band. The special case of $R_{\text{radius}} = 1$ corresponds to a spherical structure of the cluster. The ratio of the energies was evaluated by fitting of the experimental results by double-Lorentzian functions:

$$D'(E) = \frac{D_{\text{major}}'}{1+\left(\dfrac{E-E_{\text{major}}}{E_{\text{w,major}}/2}\right)^2} + \frac{D_{\text{minor}}'}{1+\left(\dfrac{E-E_{\text{minor}}}{E_{\text{w,minor}}/2}\right)^2} \tag{4.30}$$

with a constraint of $D_{\text{major}}'E_{\text{w,major}} = 2D_{\text{minor}}'E_{\text{w,minor}}$ for the intensity ratio of the two bands, where E is the photon energy, $D_{\text{major/minor}}'$ the maximum intensity of each Lorentzian at the photon energy of $E_{\text{major/minor}}$, and E_{w} the full width at half maximum, respectively. The subscript, major/minor, specifies whether the absorption is more intense or less. An example of the results of the fitting is shown in Figure 4.12, where $E_{\text{major}} = 4.02$ eV, $E_{\text{minor}} = 3.67$ eV, and $R_{\text{energy}} = 1.10$ were obtained. The resonance energies and energy ratios thus evaluated are depicted in Figure 4.13, which explains the growth mechanism of Ag_N^+; the cluster shows oblate structures at $N = 19$ and 20, and becomes spherical at $N = 21$. Silver atoms are added to elongate the geometry above $N = 21$, which results in prolate structures. At $N = 27$, silver atoms prefer to attach in the direction perpendicular to the symmetric axis probably to maximize the coordination number. Therefore, the cluster shows again a spherical structure at $N \sim 40$. Such a geometric growth, i.e., oblate → sphere → prolate → sphere → prolate → sphere, is observed up to $N = 92$ (Figure 4.14).

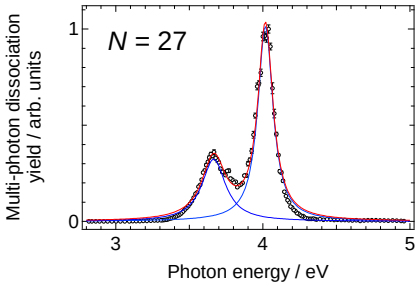

Figure 4.12. The result of the fitting. Circles: experimental results. Blue curves: Lorentzian function. Red curves: summation of the two Lorentzian. $D_{\text{major}}' = 1.01$, $E_{\text{major}} = 4.02$ eV, $E_{\text{w,major}} = 0.12$ eV, $D_{\text{minor}}' = 0.32$, $E_{\text{minor}} = 3.67$ eV, and $E_{\text{w,minor}} = 0.20$ eV.

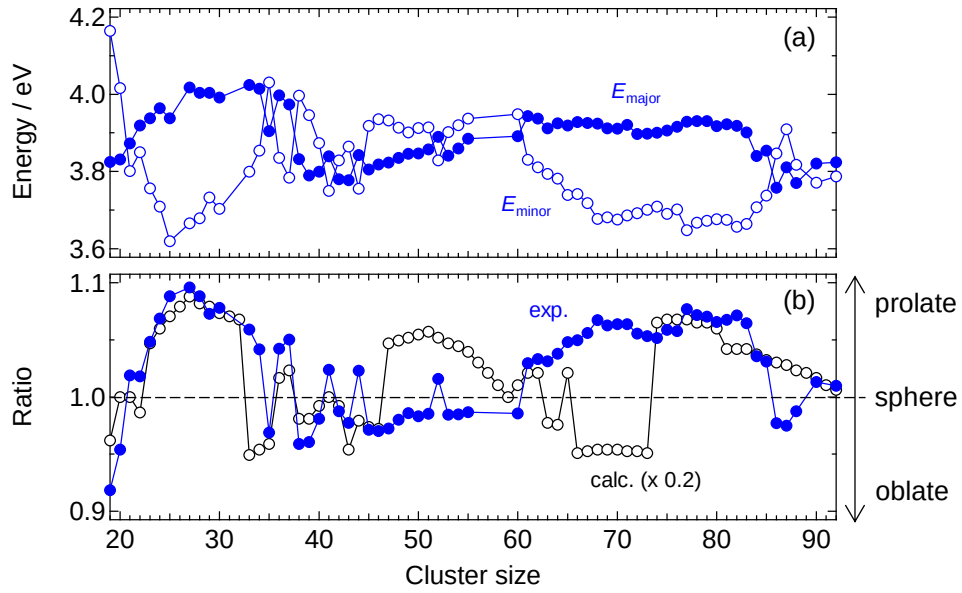

Figure 4.13. (a) The photon energies of the two bands observed in the photodissociation spectra as a function of cluster size. The data were obtained by the double-Lorentzian fitting to the experimental results. The fitting was not carried out for $N = 26$, 31, and 32, where triple-band profiles were observed. (b) Geometric structures represented by distortion from a sphere predicted for silver cluster cations. Blue filled circles: the experimental energy ratio. Black open circles: the radial ratio of the most stable geometry based on the Clemenger–Nilsson model, which is scaled by 0.2 for visibility. The anharmonic parameter U was set to be 0.04, which is the same as that in Clemenger's report for neutral sodium clusters.

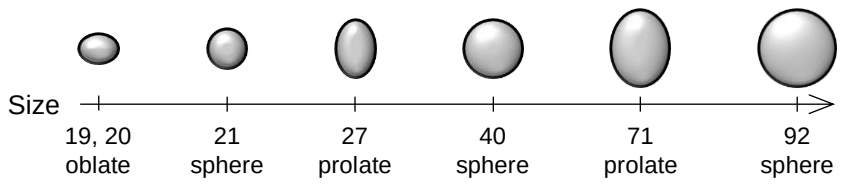

Figure 4.14. Illustration of the geometric growth of Ag_N^+.

The Clemenger–Nilsson model [42] is a successful model to explain experimental results [41, 53, 61]. In this model, a valence electron experiences an anisotropic quasi-harmonic potential; the effective single-particle Hamiltonian is expressed by

$$\begin{aligned}\hat{H} &= \frac{\hat{\mathbf{p}}^2}{2m_e} + \frac{1}{2}m_e\omega_0^2\left(\Omega_\perp^2 r^2 + \Omega_z^2 z^2\right) - U\hbar\omega_0\left(\hat{\mathbf{l}}^2 - \left\langle \mathbf{l}^2 \right\rangle_{N_{\text{total}}}\right) \\ &\equiv \hat{H}_0 - U\hbar\omega_0\left(\hat{\mathbf{l}}^2 - \left\langle \mathbf{l}^2 \right\rangle_{N_{\text{total}}}\right)\end{aligned} \tag{4.31}$$

where $\hat{\mathbf{p}}$ is the momentum operator, m_e the electron mass, ω_0 the eigenfrequency when the distortion parameter , δ, and the anharmonic parameter, U, are zero, $\Omega_\perp = \left(\frac{2+\delta}{2-\delta}\right)^{\frac{1}{3}}$ and $\Omega_z = \left(\frac{2+\delta}{2-\delta}\right)^{-\frac{2}{3}}$ ellipsoidal scaling factors satisfying the constant-volume constraint $\Omega_\perp^2\Omega_z = 1$, z the coordinate along the symmetry axis, r the distance from the z-axis, $\hbar$ Dirac's constant, $\hat{\mathbf{l}}$ the total angular momentum operator, $\left\langle \mathbf{l}^2 \right\rangle_{N_{\text{total}}} = \frac{1}{2}N_{\text{total}}\left(N_{\text{total}}+3\right)$, N_{total} the total oscillator quantum number, and $\hat{H}_0$ the harmonic part of the Hamiltonian. The non-zero anharmonic parameter U works to flatten the bottom of the harmonic potential. The distortion parameter δ is associated with the radial ratio R_{radius} as

$$R_{\text{radius}} = \frac{2+\delta}{2-\delta}. \tag{4.32}$$

By using Rassey's representation of basis functions, non-zero elements of the Hamiltonian matrix **H** are calculated by the following equations [62]:

$$
\begin{aligned}
&\left\langle N_{\text{total}}, N_z, \Lambda \middle| \hat{H}_0 \middle| N_{\text{total}}, N_z, \Lambda \right\rangle \\
&= \left(N_{\text{total}} - N_z + 1\right)\hbar\omega_0\Omega_\perp + \left(N_z + \frac{1}{2}\right)\hbar\omega_0\Omega_z \\
&\left\langle N_{\text{total}}, N_z + 2, \Lambda \middle| \hat{\mathbf{l}}^2 \middle| N_{\text{total}}, N_z, \Lambda \right\rangle \\
&= \sqrt{\left(N_{\text{total}} - N_z - \Lambda\right)\left(N_{\text{total}} - N_z + \Lambda\right)\left(N_z + 1\right)\left(N_z + 2\right)}, \\
&\left\langle N_{\text{total}}, N_z - 2, \Lambda \middle| \hat{\mathbf{l}}^2 \middle| N_{\text{total}}, N_z, \Lambda \right\rangle \\
&= \sqrt{\left(N_{\text{total}} - N_z + \Lambda + 2\right)\left(N_{\text{total}} - N_z - \Lambda + 2\right)N_z\left(N_z - 1\right)}, \\
&\left\langle N_{\text{total}}, N_z, \Lambda \middle| \hat{\mathbf{l}}^2 \middle| N_{\text{total}}, N_z, \Lambda \right\rangle \\
&= \Lambda^2 + 2N_z\left(N_{\text{total}} - N_z\right) + 2N_z + \left(N_{\text{total}} - N_z\right),
\end{aligned}
\tag{4.33}
$$

where N_z is the number of oscillator quanta along the symmetry axis and Λ the z-component of the orbital angular momentum. The Hamiltonian matrix **H** thus derived is block-diagonalized as

$$
\mathbf{H} = \begin{bmatrix}
\boxed{\mathbf{H}_{0,0}} & & & & & \\
& \boxed{\mathbf{H}_{1,0}} & & & \mathbf{0} & \\
& & \boxed{\mathbf{H}_{1,1}} & & & \\
& & & \boxed{\mathbf{H}_{2,0}} & & \\
& & & & \boxed{\mathbf{H}_{2,1}} & \\
& \mathbf{0} & & & & \boxed{\mathbf{H}_{2,2}} \\
& & & & & & \ddots
\end{bmatrix},
\tag{4.34}
$$

where $\mathbf{H}_{N_{\text{total}},\Lambda}$ is a matrix formed by collecting non-zero elements of **H** having common N_{total} and Λ, e.g., $\mathbf{H}_{0,0} = \left\langle 0,0,0 \middle| \hat{H} \middle| 0,0,0 \right\rangle, \mathbf{H}_{2,0} = \begin{bmatrix} \left\langle 2,0,0 \middle| \hat{H} \middle| 2,0,0 \right\rangle & \left\langle 2,0,0 \middle| \hat{H} \middle| 2,2,0 \right\rangle \\ \left\langle 2,2,0 \middle| \hat{H} \middle| 2,0,0 \right\rangle & \left\langle 2,2,0 \middle| \hat{H} \middle| 2,2,0 \right\rangle \end{bmatrix}$,

etc. **H** is diagonalized by the matrix

$$\mathbf{P} = \begin{bmatrix} \mathbf{P}_{0,0} & & & & & \\ & \mathbf{P}_{1,0} & & & \mathbf{0} & \\ & & \mathbf{P}_{1,1} & & & \\ & & & \mathbf{P}_{2,0} & & \\ & & & & \mathbf{P}_{2,1} & \\ & \mathbf{0} & & & & \mathbf{P}_{2,2} \\ & & & & & \ddots \end{bmatrix}, \tag{4.35}$$

where $\mathbf{P}_{N_{\text{total}},\Lambda}$ is a matrix diagonalizing $\mathbf{H}_{N_{\text{total}},\Lambda}$. Therefore, the (exact) eigenenergies are derived as the diagonal elements of $\mathbf{P}^{-1}_{N_{\text{total}},\Lambda}\mathbf{H}_{N_{\text{total}},\Lambda}\mathbf{P}_{N_{\text{total}},\Lambda}$. Note that $\Lambda = 0$ levels are twofold degenerate, while the others are fourfold degenerate. The eigenenergy is a function of the distortion parameter δ. The most stable geometry is predicted by a distortion parameter which results in the minimum total energy of electrons.

The result is superimposed in Figure 4.13 (b) by black open circles. The ratio evaluated based on the Clemenger–Nilsson model explains the experimental result qualitatively below $N \leq 46$. A disagreement between the results is observed above $N \geq 47$; sphere-like or oblate structures were experimentally indicated for $N = 47$–60, while rather prolate structures were predicted by the Clemenger–Nilsson model. As for $N = 66$–73, the clusters were suggested to be prolate by experiments, while oblate structures were predicted by the model. The disagreement implies that an effect of packing becomes dominant at the larger sizes; atoms in the cluster are located to maximize their coordination number to stabilize the cluster in the experiment. Such a disagreement was also reported in a previous photoelectron-spectroscopic study on sodium cluster anions

with the size of 40–57 [61]. As for larger sizes, an elongated structure at $N = 71$ and a spherical one at $N = 92$ were reported for sodium cluster anions in a previous experimental study [63] and for their neutral counterparts in a theoretical study employing classical interatomic potentials [64]. Moreover, the packing scheme also explains the local minima in the mass spectra of photoionized sodium clusters with the sizes of 1500–22000 [62]. Geometric structures of neutral silver clusters were also reported by Chen et al., where geometry optimization was performed by employing an embedded atom method potential in combination with a genetic algorithm [66]. To compare their geometries with the present photodissociation spectra, moments of inertia of each cluster are evaluated by assuming that the clusters are expressed by an ellipsoid with a uniform density and radii of r_x, r_y, and r_z:

$$\sum_{i=1}^{N} m_i \left(x_i^2 + y_i^2 \right) = \frac{1}{5} m_{\text{ellipsoid}} \left(r_x^2 + r_y^2 \right) \tag{4.36}$$

around z-axis, where m_i is the mass of the i-th atom, $m_{\text{ellipsoid}} = \sum_{i=1}^{N} m_i$ that of the ellipsoid, $x_i^2 + y_i^2$ the squared distance between the i-th atom and z-axis. By solving the equation for the geometric structures of $Ag_{40,55,71,92}$ reported by Chen et al., their corresponding radii were derived as listed in Table 4.2. This analysis supported the present results of photodissociation spectroscopy except for $N = 40$. As will be mentioned in Section 6.4, for example, an oblate structure was also obtained for Ag_{38}^+ by a theoretical calculation in the present study, which resulted in a double-band profile in its absorption spectrum. The present photodissociation spectrum indicates the existence of a spherical geometry which was not found in the present/previous calculations.

Table 4.2. Estimation of radii of neutral silver clusters, Ag_N, and geometry assignments by the author. The coordinates of geometries for the calculation were cited from the report by Chen et al. [66].

N	r_x / Å	r_y / Å	r_z / Å	Geometry assignment
40	5.8	5.6	4.4	oblate
55	5.8	5.8	5.8	sphere
71	7.5	5.9	5.9	prolate
92	7.1	7.1	7.1	sphere

As mentioned above, absorption bands converged into a narrow spectral range above N = 19, which suggests collective excitation of electrons. The present photodissociation spectroscopy revealed also geometry evolution in silver cluster cations as follows: oblate (N = 19, 20) → sphere (N = 21, 22) → prolate (N = 23–25, 27–30, 33) → sphere (N = 34–60) → prolate (N = 61–83) → sphere (N = 84–92). By combining these insights, threefold degenerate collective excitations of electrons are expected for spherical clusters, which was observed as a single band. On the other hand, the degeneracy is supposed to be lifted in a prolate structure; a collective excitation along the symmetry axis is located at a lower energy than that of twofold degenerate collective excitations perpendicular to the symmetry axis. In addition, the absorption band of Ag_{55}^+ at 3.9 eV redshifted by 0.1 eV at N = 92. Such geometry- and size-dependence of an absorption spectrum is well-known in collective excitations of electrons in nanoparticles and nanorods. Form this analogy, it is implied that collective excitation of electrons emerges above N = 19. However, an additional analysis on oscillator strengths is necessary to conclude the emergence of collective excitation of electrons,

which will be presented in the next chapter on the basis of cavity ring-down spectroscopy that enables evaluation of one-photon absorption cross sections even for these large sizes without relying on multi-photon dissociation.

4.7. Summary

Photodissociation action spectroscopy was performed on silver cluster cations, Ag_N^+, almost every size in a very broad range from $N = 2$ to 92. For larger cluster sizes, multi-photon absorption was necessary for the clusters to dissociate. Such multi-photon processes were interpreted by the following scenario: the photon energy absorbed is converted to a vibrational energy via internal conversion followed by intramolecular vibrational energy redistribution (IVR) processes. The RRK theory tells us that photodissociation that takes place via localization of the internal energy in a specific vibrational mode occurs less frequently at larger sizes, which results in a low dissociation rate. Therefore, multi-photon absorption is necessary for larger clusters to undergo photodissociation.

The present photodissociation spectra were compared with previous ones. Especially, Ag_9^+ showed a multi-modal profile, which was in contrast to the previous report by Tiggesbäumker et al. [30–32]; they observed a broad band which carries 94% of oscillator strengths originating from the eight valence electrons and thus concluded that the absorption was collective. The temperature-controlled present study revealed that such interpretation is not rationalized, i.e., collective excitation of electrons is not probable for Ag_9^+. The broad intense band must have rather been due to a high internal energy and a systematic error in their measurement. On the other hand, Ag_{21}^+ exhibited a single band similar to but narrower than that observed by Tiggesbäumker et al. [30–32].

Generally, the smaller clusters with the sizes of $N \leq 14$ showed multiple bands over the entire energy range of 2.8–5.0 eV, while one or two bands were observed for those with $N \geq 19$. Such concentration of absorption bands indicates emergence of the collective excitation of electrons in silver cluster cations with $N \geq 19$. The size-dependence of the spectral profile also provided information on a growth process of clusters, i.e., oblate → sphere → prolate → sphere → prolate → sphere, up to $N = 92$; the single-band profiles correspond to a spherical geometry, where three collective excitation modes are degenerate. On the other hand, the degeneracy is lifted in prolate structures, which results in a collective excitation along the symmetry axis at a lower energy and a twofold degenerate collective excitation perpendicular to the axis at a higher energy. Moreover, a redshift of the absorption band was observed as the cluster grew from $N = 55$ to 92. These trends are reminiscent of collective excitation of electrons in nanoparticles and nanorods.

However, it is necessary to discuss oscillator strengths to conclude collectivity of excitations. In Chapter 5, the author tries to characterize the electronic excitations in silver cluster cations from this point of view.

References

[1] M. Schmidt, H. Haberland, *Eur. Phys. J. D* **1999**, *6*, 109.

[2] C. Bréchignac, P. Cahuzac, F. Carlier, M. de Frutos, J. Leygnier, *Chem. Phys. Lett.* **1992**, *189*, 28.

[3] C. Bréchignac, P. Cahuzac, F. Carlier, J. Leygnier, *Chem. Phys. Lett.* **1989**, *164*, 433.

[4] W. A. de Heer, K. Selby, V. Kresin, J. Masui, M. Vollmer, A. Châtelain, *Phys. Rev. Lett.* **1987**, *59*, 1805.

[5] K. Selby, V. Kresin, J. Masui, M. Vollmer, W. A. de Heer, A. Scheidemann, W. D. Knight, *Phys. Rev. B* **1991**, *43*, 4565.

[6] K. Selby, M. Vollmer, J. Masui, V. Kresin, W. A. de Heer, W. D. Knight, *Phys. Rev. B* **1989**, *40*, 5417.

[7] M. Broyer, G. Delacrétaz, G.-Q. Ni, R. L. Whetten, J.-P. Wolf, L. Wöste, *J. Chem. Phys.* **1989**, *90*, 843.

[8] K. Selby, PhD Thesis, University of California, Berkeley (United States of America), **1990**.

[9] C. R. C. Wang, S. Pollack, M. M. Kappes, *Chem. Phys. Lett.* **1990**, *166*, 26.

[10] M. F. Jarrold, K. M. Creegan, *Chem. Phys. Lett.* **1990**, *166*, 116.

[11] M. D. Morse, J. B. Hopkins, P. R. R. Langridge-Smith, R. E. Smalley, *J. Chem. Phys.* **1983**, *79*, 5316.

[12] U. Ray, M. F. Jarrold, J. E. Bower, J. S. Kraus, *Chem. Phys. Lett.* **1989**, *159*, 221.

[13] M. Broyer, G. Delacrétaz, P. Labastie, J. P. Wolf, L. Wöste, *Phys. Rev. Lett.* **1986**, *57*, 1851.

[14] K. Selby, M. Vollmer, J. Masui, V. Kresin, W. A. de Heer, W. D. Knight, *Z. Phys. D* **1989**, *12*, 477.

[15] C. R. C. Wang, S. Pollack, D. Cameron, M. M. Kapees, *J. Chem. Phys.* **1990**, *93*, 3787.

[16] M. F. Jarrold, K. M. Creegan, *Int. J. Mass Spectrom. Ion Processes* **1990**, *102*, 161.

[17] C. R. C. Wang, S. Pollack, T. A. Dahlseid, G. M. Koretsky, M. M. Kappes, *J. Chem. Phys.* **1992**, *96*, 7931.

[18] S. Pollack, C. R. C. Wang, M. M. Kappes, *J. Chem. Phys.* **1991**, *94*, 2496.

[19] H. Fallgren, T. P. Martin, *Chem. Phys. Lett.* **1990**, *168*, 233.

[20] J. Borggreen, P. Chowdhury, N. Kebaïli, L. Lundsberg-Nielsen, K. Lützenkirchen, M. B. Nielsen, J. Pedersen, H. D. Rasmussen, *Phys. Rev. B* **1993**, *48*, 17507.

[21] W. A. de Heer, *Rev. Mod. Phys.* **1993**, *65*, 611.

[22] J. Blanc, M. Broyer, J. Chevakeyre, P. Dugourd, H. Kühling, P. Labastie, M. Ulbricht, J. P. Wolf, L. Wöste, *Z. Phys. D* **1991**, *19*, 7.

[23] J. Pedersen, J. Borggreen, P. Chowdhury, N. Kebaïli, L. Lundsberg-Nielsen, K. Lützenkirchen, M. B. Nielsen, H. D. Rasmussen, *Z. Phys. D* **1993**, *26*, 281.

[24] H. Fallgren, K. M. Brown, T. P. Martin, *Z. Phys. D* **1991**, *19*, 81.

[25] C. R. C. Wang, S. Pollack, J. Hunter, G. Alameddin, T. Hoover, D. Cameron, S. Liu, M. M. Kappes, *Z. Phys. D* **1991**, *19*, 13.

[26] W. A. Saunders, P. Fayet, L. Wöste, *Phys. Rev. A* **1989**, *39*, 4400.

[27] J. Tiggesbäumker, L. Köller, K. H. Meiwes-Broer, *Chem. Phys. Lett.* **1996**, *260*, 428.

[28] C. Ellert, M. Schmidt, C. Schmitt, T. Reiners, H. Haberland, *Phys. Chem. Lett.* **1995**, *75*, 1731.

[29] J. Tiggesbäumker, L. Köller, H. O. Lutz, K. H. Meiwes-Broer in Nuclear Physics Concepts in the Study of Atomic Cluster Physics, Lecture Notes in Physics Vol 404 (Eds.: R. Schmidt, H. O. Lutz, R. Dreizler), Springer, Berlin, Heidelberg, **1992**, p.244.

[30] J. Tiggesbäumker, L. Köller, H. O. Lutz, K. H. Meiwes-Broer, *Chem. Phys. Lett.* **1992**, *190*, 42.

[31] J. Tiggesbäumker, L. Köller, H. O. Lutz, K. H. Meiwes-Broer in Physics and Chemistry of Finite Systems: From Clusters to Crystals, NATO ASI Series Vol. 374 (Eds.: P. Jena, S. N. Khanna, B. K. Rao), Springer, Dordrecht, **1992**, p. 1001.

[32] J. Tiggesbäumker, L. Köller, K.-H. Meiwes-Broer, A. Liebsch, *Phys. Rev. A* **1993**, *48*, R1749.

[33] D. M. Rayner, K. Athanassenas, B. A. Collings, S. A. Mitchell, P. A. Hackett in Theory of Atomic and Molecular Clusters: With a Glimpse at Experiments, Springer Series in Cluster Physics (Ed.: J. Jellinek), Springer, Berlin, Heidelberg, **1999**, p. 371.

[34] B. A. Collings, K. Athanassenas, D. M. Rayner, P. A. Hackett, *Chem. Phys. Lett.* **1994**, *227*, 490

[35] T. Ito, PhD Thesis, Kyushu University (Japan), **2015**.

[36] A. Terasaki, T. Majima, C. Kasai, T. Kondow, *Eur. Phys. J. D* **2009**, *52*, 43.

[37] K. Egashira, C. Bartels, T. Kondow, A. Terasaki, *Eur. Phys. J. D* **2011**, *63*, 183.

[38] K. Egashira, A. Terasaki, *Chem. Phys. Lett.* **2015**, *635*, 13.

[39] A. Terasaki, T. Majima, T. Kondow, *J. Phys.: Conf. Ser.* **2009**, *185*, 012045.

[40] A. Terasaki, S. Minemoto, M. Iseda, T. Kondow, *Eur. Phys. J. D* **1999**, *9*, 163.

[41] S. Kawamura, M. Yamaguchi, S. Kono, M. Arakawa, T. Yasuike, T. Horio, A. Terasaki, *J. Phys. Chem. A* **2023**, *127*, 6063.

[42] K. Clemenger, *Phys. Rev. B* **1985**, *32*, 1359.

[43] M. Moseler, H. Häkkinen, U. Landman, *Phys. Rev. Lett.* **2001**, *87*, 053401.

[44] O. K. Rice, H. C. Ramsperger, *J. Am. Chem. Soc.* **1927**, *49*, 7.

[45] L. S. Kassel, *J. Phys. Chem.* **1928**, *32*, 225.

[46] J. I. Steinfeld, J. S. Francisco, W. L. Hase, *Chemical Kinetics And Dynamics*, Prentice Hall, Upper Side River, **1989**, p. 358.

[47] N. W. Aschcroft, N. D. Mermin, *Solid State Physics*, Saunders College, Philadelphia, **1976**, p. 458.

[48] J. Westergren, H. Grönbeck, S.-G. Kim, D. Tománek, *J. Chem. Phys.* **1997**, *107*, 3071.

[49] M. Masili, A. F. Starace, *Phys. Rev. A* **2003**, *68*, 012508.

[50] S. Krückeberg, G. Dietrich, K. Lüzenkirchen, L. Schweikhard, C. Walther, J. Ziegler, *J. Chem. Phys.* **1999**, *110*, 7216.

[51] W. D. Knight, K. Clemenger, W. A. de Heer, W. A. Saunders, M. Y. Chou, M. L. Cohen, *Phys. Rev. Lett.* **1984**, *52*, 2141.

[52] M. Lindinger, K. Dasgupta, G. Dietrich, S. Krückeberg, S. Kuznetsov, K. Lützenkirchen, L. Schweikhard, C. Walther, J. Ziegler, *Z. Phys. D* **1997**, *40*, 347.

[53] K. Selby, M. Vollmer, J. Masui, V. Kresin, W. A. de Heer, W. D. Knight, *Phys. Rev. B* **1989**, *40*, 5417.

[54] C. Yu, R. Schira, H. Brune, B. von Issendorff, F. Rabilloud, W. Harbich, *Nanoscale* **2018**, *10*, 20821.

[55] W. Harbich, S. Fedrigo, J. Buttet, *Chem. Phys. Lett* **1992**, *195*, 613.

[56] S. Fedrigo, W. Harbich, J. Buttet, *Phys. Rev. B* **1993**, *47*, 10706.

[57] W. Harbich, S. Fedrigo, J. Buttet, *Z. Phys. D* **1993**, *26*, 138.

[58] S. Fedrigo, W. Harbich, J. Belyaev, J. Buttet, *Chem. Phys. Lett.* **1993**, 211, 166.

[59] N. Iwe, K. Raspe, F. Martinez, L. Schweikhard, K.-H. Meiwes-Broer, J. Tiggesbäumker, *Phys. Chem. Chem. Phys.* **2023**, *25*, 1677.

[60] R. Schira, F. Rabilloud, *J. Phys. Chem. C* **2018**, *122*, 27656.

[61] B. Huber, M. Moseler, O. Kostko, B. von Issendorff, *Phys. Rev. B* **2009**, *80*, 235425.

[62] A. J. Rassey, *Phys. Rev.* **1958**, *109*, 949.

[63] O. Kostko, B. Huber, M. Moseler, B. von Issendorff, *Phys. Rev. Lett.* **2007**, *98*, 043401.

[64] E. G. Noya, J. P. K. Doye, D. J. Wales, A. Aguado, *Eur. Phys. J. D* **2007**, *43*, 57.

[65] T. P. Martin, T. Bergmann, H. Göhlich, T. Lange, *Z. Phys. D* **1991**, *19*, 25.

[66] M. Chen, J. E. Dyer, K. Ki, D. A. Dixon, *J. Phys. Chem. A* **2013**, *117*, 8298.

5. Cavity Ring-Down Spectroscopy

5.1. Introduction

In Chapter 4, electronic excitations of silver cluster cations were found to center around a specific energy range above $N = 19$ as elucidated by photodissociation spectroscopy. Although it was speculated that the spectral profiles are explained by collective excitation modes by comparing them with the change in the cluster geometries, there are several problems in the discussion based on photodissociation; photodissociation cross sections cannot be regarded as photoabsorption cross sections unless the photodissociation yield is unity. Moreover, photodissociation spectroscopy cannot determine even spectral profiles because of the involvement of multi-photon processes discussed in Chapter 4. Therefore, the oscillator strengths are not determined by relying only on photodissociation spectroscopy, especially for larger clusters. Therefore, it is desired to perform quantitative absorption spectroscopy without relying on action spectroscopy. However, it is not feasible to measure absorption cross sections by conventional transmission measurements based on the Beer–Lambert law as mentioned in Section 2.1.

Cavity ring-down spectroscopy [1] is a highly sensitive technique to detect very weak extinction of light through a low-density sample, which enables "direct" measurement of optical absorption without relying on photodissociation. Since its development by O'Keefe et al., the technique has been applied to various systems [2, 3], e.g., atoms [4], molecules [5–21], radicals [22–25], ions [26–28], films [29–35], nanoparticles [36, 37], and metal clusters [38–44]. However, there are only a few reports on size-selected clusters [40, 44] because of difficulties due to an extremely low sample density.

In the present study, an ion trap is employed for cavity ring-down spectroscopy to overcome this difficulty by accumulating sample clusters to enhance their density. Genuine photoabsorption spectra of silver cluster cations, Ag_N^+ (N = 3, 4, 8, 9, 35, 40, 45, 50, 55, 60, 65, 70, 71, 81, and 92) are presented here for the first time after previous reports limited to N = 2 and 9. Concentration of oscillator strengths in a specific spectral range is revealed quantitatively, which leads to conclusion that collective excitation of electrons emerges above N = 19, by combining the insight from the present photodissociation spectroscopy presented in Chapter 4.

5.2. Principle

In cavity ring-down spectroscopy, a pair of high-reflectivity mirrors, i.e., an optical "cavity," is arranged to enclose a sample as shown in Figure 5.1. An incident laser beam undergoes multiple reflection between the two mirrors, during which it decays gradually due to absorption by the sample of trapped ions. At the same time, a small fraction of the incident light leaks out through the mirror. The intensity of the light leakage, I_i, is a function of the number of round trips, i. The light undergoes reflection twice by the mirrors with reflectivity of R as well as absorption along the optical path through an ion cloud with a total length of $2L_{\mathrm{trap}}$ during one round trip, which causes extinction of light intensity according to the Beer–Lambert law:

$$\frac{I_{i+1}}{I_i} = \left(R \exp(-\sigma_{\mathrm{abs}} n_{\mathrm{parent}} L_{\mathrm{trap}}) \right)^2, \tag{5.1}$$

where σ_{abs} is an absorption cross section of the sample cluster ions, n_{parent} a density of the trapped ions. This equation is generalized as follows:

$$\frac{I_i}{I_0} = \left(R \exp(-\sigma_{\mathrm{abs}} n_{\mathrm{parent}} L_{\mathrm{trap}}) \right)^{2i}, \tag{5.2}$$

where I_0 is an intensity of the first output. The number of round trips is related to the cavity length, L_{cavity}, speed of light, c, and time, t:

$$i = \frac{t}{2L_{\text{cavity}}/c}. \tag{5.3}$$

By introducing a notation of $I(t)$ as a function of time instead of I_i, the intensity is expressed by the following equation:

$$\frac{I(t)}{I_0} = \left(R\exp(-\sigma_{\text{abs}} n_{\text{parent}} L_{\text{trap}})\right)^{\frac{ct}{L_{\text{cavity}}}}, \tag{5.4}$$

which implies that the intensity decays exponentially as $\exp(-kt)$ with a decay rate of

$$k = \frac{c}{L_{\text{cavity}}}\left(\sigma_{\text{abs}} n_{\text{parent}} L_{\text{trap}} - \ln R\right). \tag{5.5}$$

By defining k_0 as a decay rate without a sample in the trap, the difference, Δk, between k and k_0 is proportional to the absorption cross section:

$$\sigma_{\text{abs}} = \frac{L_{\text{cavity}}}{cL_{\text{trap}}}\frac{\Delta k}{n_{\text{parent}}}. \tag{5.6}$$

Because L_{cavity} and L_{trap} are constants specific to the present experimental setup (see Figure 5.1) as well as the speed of light c, the absorption cross section is determined by measuring Δk and n_{parent}.

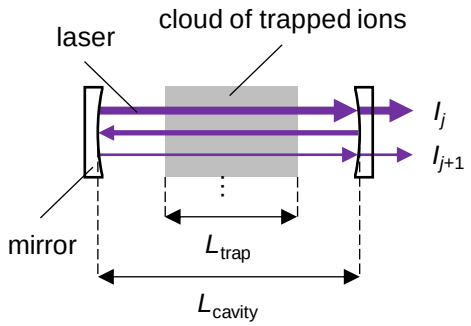

Figure 5.1. A schematic view of the setup for cavity ring-down spectroscopy.

5.3. Experimental procedures

In the present study, size-selected silver cluster cations prepared by the same way as in the photodissociation spectroscopy were loaded in the ion trap, where a buffer helium gas at room temperature was introduced to thermalize the ions for 500 ms. After thermalization, the ions were irradiated by 100 shots of the pulsed laser. Temporal profiles of light intensity were monitored by the oscilloscope device. The laser irradiation was followed by extracting the ions toward the electrode connected to the ammeter. It is noteworthy that the electrode was placed in the third-deflector chamber: the electrode behind the second quadrupole mass filter was not used in the cavity ring-down spectroscopy because transmittance of ions through the mass filter is not 100%, which makes it difficult to estimate an actual density of ions inside the trap. On the other hand, the electrode behind the mass filter was used when it was necessary to examine whether the ions did not dissociate upon absorbing photons; the photon flux was adjusted not to induce photodissociation. The above set of measurements were repeated for 100 times to derive an increase in the decay rate, Δk, and the number of the trapped ions. The density, n_{parent}, of the trapped ions was estimated from the number of the ions by assuming that its spatial-distribution profile was the same as that measured by photodissociation spectroscopy in advance. An absorption cross section, σ_{abs}, was calculated from these values. The measurement was repeated as a function of photon energy to derive an absorption spectrum for one size of the cluster.

There is a difficulty in determination of the ion density; it drastically changes as a function of distance from the central axis of the ion trap. It is desirable to irradiate the densest and uniform region of the trapped ions. Prior to the cavity ring-down spectroscopy, a spatial distribution of the ions inside the trap was measured by employing

photodissociation as described in Chapter 4. Cavity mirrors were arranged carefully to maximize overlap between the distribution of the trapped ions and the cavity mode of the laser. A Gaussian cavity mode in the middle of the cavity is expressed by

$$I(x,y) = I(0,0)\exp\left(-2\frac{x^2+y^2}{w^2}\right), \tag{5.7}$$

where (x, y) is a radial vector perpendicular to the cavity axis with its origin at the axis and $2w$ the minimum beam diameter; $1 - \exp(-2) = 86.5\%$ of the light energy of the Gaussian mode is focused inside this diameter. The parameter, w, is given as follows [45]:

$$w^2 = \frac{\lambda}{2\pi}\sqrt{L_{\text{cavity}}\left(2\rho - L_{\text{cavity}}\right)}, \tag{5.8}$$

where λ is the wavelength of the incident light, π the circle ratio, ρ the radius of curvature of the mirrors, which is 6 m in this study. The cavity length L_{cavity} was 1.6 m. For the incident laser with a wavelength of 308 nm, $2w \sim 1$ mm, which implies that almost all the incident light interact with the ion density at the trap center in view of the spatial distribution of the ions measured as shown in Figure 4.2. This is the reason why the density maxima were used to calculate the absorption cross sections in this study. Of course, the beam diameter estimated above is that in an ideal case where the curvature of the wavefront of the incident laser perfectly coincides with that of the cavity mirrors; the beam radius may be larger than the ideal value practically.

A spectral range of absorption spectra obtainable is limited by specification of the cavity mirrors. Reflectivity of cavity mirrors is an important factor determining sensitivity of the measurement: change in the decay rates due to absorption by a sample is undistinguishable from rapid decay by reflection loss at cavity mirrors if the reflectivity is low. It is important to measure an entire spectral range of absorption for characterizing

electronic transitions based on oscillator strengths. The reflectivity as a function of photon energy measured for three pairs of cavity mirrors employed in this study is shown in Figure 5.2. A single mirror covers only a narrow spectral range. A wide spectral range was thus covered by the three pairs of mirrors designed for different energy ranges.

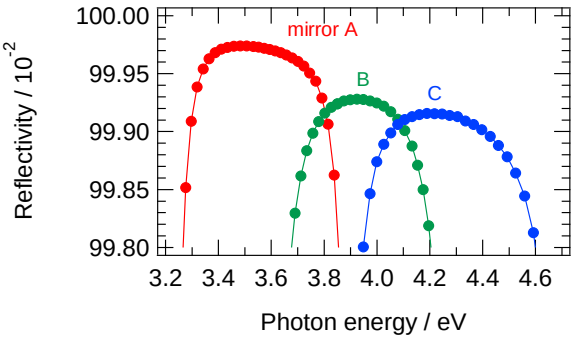

Figure 5.2. Reflectivity of the mirrors used in this study, which was measured by the cavity ring-down technique without a sample, i.e., for an empty cavity. Data for three types of mirrors are plotted, which have different coating optimized for covering the wide spectral range.

5.4. Results

Photoabsorption spectra of silver cluster cations, Ag_N^+, measured as a function of photon energy are shown in Figure 5.3. Especially, three types of the mirrors were employed in the measurements for $N = 55$, 71, 81, and 92. The photodissociation spectra presented in Chapter 4 are superimposed in the figure by gray curves.

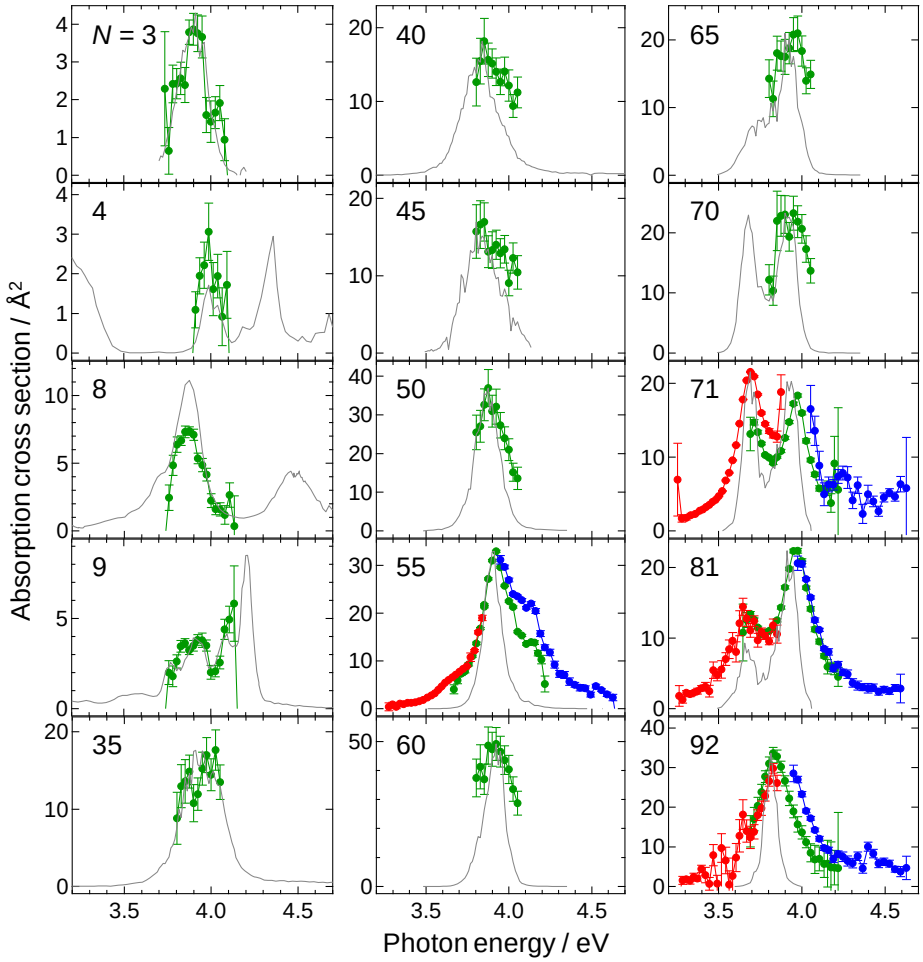

Figure 5.3. Photoabsorption spectra of silver cluster cations, Ag_N^+. Colored circles: photoabsorption cross sections measured by the cavity ring-down technique with three types of mirrors. Gray curves: photodissociation spectra measured in the present study, i.e., identical to the plots in Figures 4.4–4.7; multi-photon dissociation spectra are scaled so that the band height is comparable with the maximum absorption cross section.

As for $N \leq 9$, the cross sections and spectral profiles of the absorption spectra were identical with those of the photodissociation spectra within the systematic errors of the measurement. This agreement implies that the probability of dissociation for these clusters was unity in the present experiments, which is consistent with the simulation in Chapter 4 where the RRK dissociation rate and the cooling effect by the buffer helium

gas are considered. On the other hand, the widths of absorption bands for $N \geq 40$ were broader than those of corresponding photodissociation action spectra. This disagreement originates from the multi-photon processes involved in photodissociation discussed in Chapter 4; the gray curves in Figure 5.3 denote "multi-photon dissociation yields" proportional to the product of multiple photoabsorption cross sections and a dissociation cross section as defined by Equation (4.21). Moreover, Ag_{60}^{+} showed a maximum intensity of ~50 $Å^2$ at 3.9 eV, while $Ag_{65,70,71,81}^{+}$ exhibited absorption maxima of ~20 $Å^2$ at the same photon energy. Such a decrease in the absorption cross section is consistent with the discussion made in Chapter 4; due to the elongation of the geometric structure of the cluster, three-fold degenerate excitations are split into two excitation modes, i.e., a doubly degenerate mode along two shorter axes of the cluster with a higher excitation energy and a single mode along the longer axis with a lower excitation energy. As a result of this splitting, the absorption band at the higher energy lost its oscillator strength, which caused the decrease in the absorption cross section. The lost oscillator strength was carried by the band emerged at the lower photon energy, which was confirmed in the absorption spectra of $N = 71$ and 81 measured by employing the mirror A (red circles).

Before the following discussion, it is necessary to mention the systematic error in the absorption cross sections. As for $N = 92$, there are three data sets in the present absorption spectra. There plots must coincide at the same photon energies especially where the reflectivity of the mirrors is identical (i.e., at ~3.8 and ~4.1 eV, see Figure 5.2). However, for example, the absorption cross sections at the higher energies plotted as the blue circles are higher than those measured at the lower energies indicated by the red and green circles. This disagreement originates from an insufficient overlap between the

spatial distribution of the trapped ions and the Gaussian cavity mode; the laser pulses would experience an ion density off the trap axis, where the density is low and has a radial gradient. To merge data of photoabsorption cross sections measured by the three types of the mirrors, the data sets with higher cross sections were scaled down to the lower ones in the overlapped spectral region. Such photoabsorption spectra, depicted in Figure 5.4, show lower limits of photoabsorption cross sections. Conversely, if the cross sections measured by the mirrors A and B are scaled, the obtained spectra show upper limits of the cross sections. From the data sets for Ag_{92}^{+}, the author concluded that photodissociation cross sections could be larger than those depicted in Figures 5.3 and 5.4 by a factor of two.

5.5. Discussion

The author focuses on oscillator strengths of the absorption bands for characterization of the present optical processes. An oscillator strength is related to absorption cross sections by the following equation:

$$f = \frac{4\varepsilon_0 m_e c}{he^2} \int_{E_{min}}^{E_{max}} \mathrm{d}E \, \sigma_{abs}(E), \tag{5.9}$$

where ε_0 is the vacuum permittivity, m_e the electron mass, c the speed of light in a vacuum, h Plank's constant, e the elementary charge, $\sigma_{abs}(E)$ the absorption cross section at the photon energy E, and E_{max} and E_{min} specify an integration interval. f = 1, i.e., $\int_{E_{min}}^{E_{max}} \mathrm{d}E \, \sigma_{abs}(E) = \frac{he^2}{4\varepsilon_0 m_e c}$ corresponds to the situation where a single electron regarded as a classical oscillator contributes to the excitation [46]. By substituting the 2018 CODATA recommended values [47, 48] for the physical constants into the above equation, the oscillator strength is represented by the following equation:

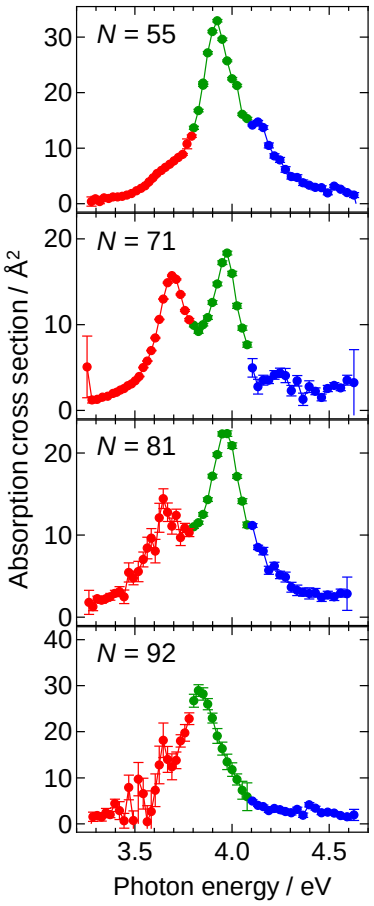

Figure 5.4. Merged spectra of silver cluster cations, Ag_N^+ (N = 55, 71, 81, and 92).

$$f = 0.911 \int_{E_{\min}}^{E_{\max}} \mathrm{d}E/\mathrm{eV}\ \sigma_{\mathrm{abs}}(E)/\mathrm{Å}^2. \tag{5.10}$$

Evaluation of oscillator strengths were performed as follows; for the clusters that dissociated by one-photon absorption, i.e., $N \leq 14$, photodissociation cross sections were assumed to be identical to photoabsorption cross sections, which were substituted into the Equation (5.10). This assumption is based on (a) equivalence between photoabsorption and photodissociation spectra for $N \leq 9$ and (b) that between experimental and predicted absorption spectra for N = 10–14 as will be shown in Chapter 6. N = 15–18 were excluded from the oscillator-strength analysis because the photodissociation cross

sections were not equivalent with absorption cross sections due to the low dissociation probability as discussed in Chapter 4 (for N = 16) or due to competing one- and two-photon-dissociation processes (for the other sizes). As for N = 35, 40, 45, 50, 60, 65, and 70 where the entire spectral range was not covered, the profiles were deduced from M-th roots of the photodissociation spectra (M is the number of photons necessary for dissociation, see Table 4.1). The profiles of photoabsorption spectra were assumed to coincide with M-th roots of the photodissociation spectra. As for N = 55, 71, 81, and 92 where the entire spectral region was covered by the present experiment, the absorption spectra were numerically integrated without relying on the photodissocitaion spectra to obtain oscillator strengths. To integrate the spectra, the three sets of data measured by each type of mirrors must be merged. In the present analysis, the data sets with higher cross sections were scaled down to the lower ones in the overlapped spectral region. Therefore, the oscillator strengths thus evaluated for N = 55, 71, 81, and 92 present the lower limits. Note that the integration in Equation (5.10) was performed over the entire spectral range. In addition, the author defines the spectral width d for characterization of concentration of oscillator strengths as

$$d^2 = \frac{\int_{E_{\min}}^{E_{\max}} \mathrm{d}E \left(E - E_{\text{average}}\right)^2 \sigma_{\text{abs}}\left(E\right)}{\int_{E_{\min}}^{E_{\max}} \mathrm{d}E\, \sigma_{\text{abs}}\left(E\right)},$$
$$E_{\text{average}} = \frac{\int_{E_{\min}}^{E_{\max}} \mathrm{d}E\, E\sigma_{\text{abs}}\left(E\right)}{\int_{E_{\min}}^{E_{\max}} \mathrm{d}E\, \sigma_{\text{abs}}\left(E\right)}. \tag{5.11}$$

The integration was performed over the entire spectral range. For example, $E_{\max}$ and $E_{\min}$ were set to be 5.0 and 2.6 eV, respectively, for the photodissociation spectrum of the tetramer (see Figure 4.4) and 4.6 and 3.3 eV, respectively, for the photoabsorption

spectrum of Ag_{92}^{+}.

The result is depicted in Figure 5.5. The oscillator strength showed an increasing trend with respect to the cluster size below $N = 14$. On the other hand, the oscillator strength did not show significant size-dependence above $N = 35$. As for neutral Ag_{55}, Koval et al. reported an absorption spectrum simulated by time-dependent density-functional theory [49], where it shows a Lorentzian-like band with a maximum intensity of ~33 $Å^2$ at ~3.70 eV and a full width at half maximum of ~0.22 eV. By substituting the Lorentzian profile with these parameters into Equation (5.10), an oscillator strength of 10.4 is obtained, which is consistent with that of the present absorption spectrum of Ag_{55}^{+} except for the redshift in their spectrum by 0.2 eV from the present experimental absorption spectrum. Koval et al. also simulated an absorption spectrum of Ag_{147}, where a Lorentzian-like band with a maximum intensity of 56 $Å^2$ at ~3.49 eV and a full width at half maximum of ~0.34 eV. These parameter yields an oscillator strength of 27.2. By interpolation between Ag_{55} and Ag_{147}, an oscillator strength of 17.2 is expected at $N = 92$, which agrees with the present result within the systematic error.

On the other hand, the spectral widths d showed a decreasing trend except for $N = 2$ and 3. Concentration of oscillator strengths was observed by the present photodissociation spectroscopy as well, although it was just a qualitative result because multi-photon dissociation spectra do not reflect absolute profiles of absorption spectra. Here, the author defines an oscillator-strength density as $\frac{f}{d}$, which represents a density of oscillator strengths within a practical spectral range. The density exhibited an increasing trend with respect to the cluster size, which elucidates concentration of oscillator strengths in a specific photon-energy range.

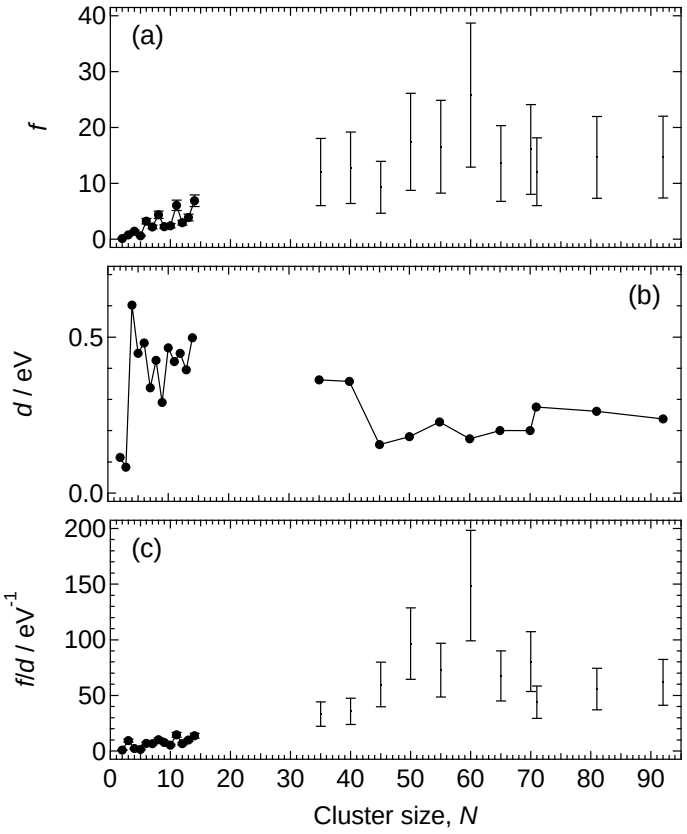

Figure 5.5. (a) Oscillator strengths, (b) spectral widths, and (c) oscillator strength per energy as a function of cluster size, *N*. The error bars denote systematic errors are not presented in the figure.

5.6. Summary

Photoabsorption spectra of silver cluster cations were measured by cavity ring-down spectroscopy. The clusters that dissociated by one-photon absorption in the present photodissociation spectroscopy (see Chapter 4) showed absorption spectra identical to their photodissociation spectra in a point of view of spectral profiles and cross sections. On the other hand, the clusters that dissociated by multi-photon processes exhibited absorption spectra broader than photodissociation action spectra. This difference in the spectral profiles was explained by the multi-photon processes. Oscillator strengths of silver cluster cations were systematically and quantitatively evaluated for specific sizes up to 92 for the first time. A density of oscillator strengths was also evaluated, which showed an increasing trend. In Chapter 6, the observed absorption will be analyzed theoretically.

References

[1] A. O'Keefe, D. A. G. Deacon, *Rev. Sci. Instrum.* **1988**, *59*, 2544.

[2] J. J. Scherer, J. B. Paul, A. O'Keefe, R. J. Saykally, *Chem. Rev.* **1997**, *97*, 25.

[3] G. Berden, R. Peeters, G. Meijer, *Int. Rev. Phys. Chem.* **2000**, *19*, 565.

[4] J.-M. Antonietti, M. Michalski, U. Heiz, H. Jones, K. H. Lim, N. Rösch, A. D. Vitto, G. Pacchioni, *Phys. Rev. Lett.* **2005**, *94*, 213402.

[5] J. J. Scherer, D. Voelkel, D. J. Rakestraw, J. B. Paul, C. P. Collier, R. J. Saykally, A. O'Keefe, *Chem. Phys. Lett.* **1995**, *245*, 273.

[6] K. K. Lehmann, G. Berden, R. Engeln in Cavity Ring-Down Spectroscopy: Techniques and Applications (Eds.: G. Berden, R. Engeln), Wiley, New York, **2009**, p. 1.

[7] R. T. Jongma, M. G. H. Boogaarts, I. Holleman, G. Meijer, *Rev. Sci. Instrum.* **1995**, *66*, 2821.

[8] A. G. Robinson, P. R. Winter, T. S. Zwier, *J. Chem. Phys.* **2002**, *116*, 7918.

[9] M. D. Wheeler, S. M. Newman, A. J. Orr-Ewing, M. N. R. Ashfold, *J. Chem. Soc. Faraday Trans.* **1998**, *94*, 337.

[10] Y. Chen, W. Wang, L. Zhu, *J. Phys. Chem. A* **2000**, *104*, 11126.

[11] L. Zhu, C.-F. Ding, *Chem. Phys. Lett.* **1997**, *265*, 177.

[12] L. Zhu, D. Kellis, C.-F. Ding, *Chem. Phys. Lett.* **1996**, *257*, 487.

[13] L. Zhu, T. Cronin, A. Narang, *J. Phys. Chem. A* **1999**, *103*, 7248.

[14] T. J. Cronin, L. Zhu, *J. Phys. Chem. A* **1998**, *102*, 10274.

[15] S. S. Brown, R. W. Wilson, A. R. Ravishankara, *J. Phys. Chem. A* **2000**, *104*, 4976.

[16] D. Kleine, S. Stry, J. Lauterbach, K. Kleinermanns, P. Hering, *Chem. Phys. Lett.* **1999**, *312*, 185.

[17] D. Romanini, K. K. Lehmann, *J. Chem. Phys.* **1993**, *99*, 6287.

[18] D. Romanini, K. K. Lehmann, *J. Chem. Phys.* **1995**, *102*, 633.

[19] D. Romanini, K. K. Lehmann, *J. Chem. Phys.* **1996**, *105*, 68.

[20] D. Romanini, A. A. Kachanov, N. Sadeghi, F. Stoeckel, *Chem. Phys. Lett.* **1997**, *264*, 316.

[21] D. Romanini, A. A. Kachanov, F. Stoeckel, *Chem. Phys. Lett.* **1997**, *5*, 546.

[22] K. Tonokura, M. Koshi, *J. Phys. Chem. A* **2000**, *104*, 8456.

[23] C. D. Pibel, A. Mcllroy, C. A. Taatjes, S. Alfred, K. Patrick, J. B. Halpern, *J. Chem. Phys.* **1999**, *110*, 1841.

[24] A. Fahr, P. Hassanzadeh, D. B. Atkinson, *Chem. Phys.* **1998**, *236*, 43.

[25] K. Tonokura, S. Marui, M. Koshi, *Chem. Phys. Lett.* **1999**, *313*, 771.

[26] M. Kotterer, J. Conceicao, J. P. Maier, *Chem. Phys. Lett.* **1996**, *259*, 233.

[27] A. Terasaki, T. Majima, T. Kondow, *J. Chem. Phys.* **2007**, *127*, 231101.

[28] A. Terasaki, T. Majima, T. Kondow, *J. Phys.: Conf. Ser.* **2009**, *185*, 012045.

[29] K. Egashira, A. Terasaki, T. Kondow, *J. Chem. Phys.* **2007**, *126*, 221102.

[30] R. Engeln, G. von Helden, A. J. A. van Roij, G. Meijer, *J. Chem. Phys.* **1999**, *110*, 2732.

[31] D. Kleine, J. Lauterbach, K. Kleinermanns, P. Hering, *Appl. Phys. B* **2001**, *72*, 249.

[32] R. N. Muir, A. J. Alexander, *Phys. Chem. Chem. Phys.* **2003**, *5*, 1279.

[33] I. M. P. Aarts, B. Hoex, A. H. M. Smets, R. Engeln, W. M. M. Kessels, M. C. M. van de Sanden, *Appl. Phys. Lett.* **2004**, *84*, 3079.

[34] T. Lelaidier, T. Lünskens, A. von Weber, T. Leoni, A. Ranguis, A. D'Aléo, F. Fages, A. Kartouzian, C. Backer, U. Heiz, *Phys. Chem. Chem. Phys.* **2016**, *18*, 5299.

[35] M. Thämer, A. Kartouzian, P. Heister, S. Gerlach, M. Tschurl, U. Boesl, U. Heiz, *J. Phys. Chem. C* **2012**, *116*, 8642.

[36] S. Gilb, K. Hartl, A. Kartouzian, J. Peter, U. Heiz, H.-G.Boyen, P. Ziemann, *Eur. Phys. J. D* **2007**, *45*, 501.

[37] A. C. R. Pipino, J. T. Woodward, C. W. Meuse, V. Silin, *J. Chem. Phys.* **2004**, *120*, 1585.

[38] A. O'Keefe, J. J. Scherer, A. L. Cooksy, R. Sheeks, J. Heath, R. J. Saykally, *Chem. Phys. Lett.* **1990**, *172*, 214.

[39] J. J. Scherer, J. B. Paul, R. J. Saykally, *Chem. Phys. Lett.* **1995**, *242*, 395.

[40] A. Terasaki, T. Majima, C. Kasai, T. Kondow, *Eur. Phys. J. D* **2009**, *52*, 43.

[41] A. Kartouzian, M. Thämer, T. Soini, J. Peter, P. Pitschi, S. Gilb, U. Heiz, *J. Appl. Phys.* **2008**, *104*, 124313.

[42] T. Lünskens, A. von Weber, M. Jakob, T. Lelaidier, A. Kartouzian, U. Heiz, *J. Phys. Chem. C* **2017**, *121*, 9331.

[43] M. Thämer, A. Kartouzian, P. Heister, T. Lünskens, S. Gerlach, U. Heiz, *small* **2014**, *10*, 2340.

[44] K. Egashira, C. Bartels, T. Kondow, A. Terasaki, *Eur. Phys. J. D* **2011**, *63*, 183.

[45] W. T. Silfvast, *Laser Fundamentals*, Cambridge University Press, Cambridge, **1996**, p.339.

[46] A. Corney, *Atomic and Laser Spectroscopy*, Clarendon Press, Oxford, **1977**, p. 274.

[47] E. Tiesinga, P. J. Mohr, D. B. Newell, B. N. Taylor, *Rev. Mod. Phys.* **2021**, *93*, 025010.

[48] E. Tiesinga, P. J. Mohr, D. B. Newell, B. N. Taylor, *J. Phys. Chem. Ref. Data*, **2021**, *50*, 033105.

[49] P. Koval, F. Marchesin, D. Foerster, D. Sánchez-Portal, *J. Phys.: Condens. Matter* **2016**, *28*, 214001.

6. Theoretical Evaluation of Collectivity in the Excitations

6.1. Introduction

In Chapters 4 and 5, the author experimentally investigated collective excitation of electrons in silver cluster cations, which was discussed from points of view of the spectral profile and the oscillator strength. On the other hand, theoretical approaches have also been made to gain further insights into collective excitations. Aikens et al. examined absorption spectra of tetrahedral neutral silver clusters with sizes of 10, 20, 35, 56, 84, and 120 to find out spectral evolution from molecular-like to plasmon-like [1, 2]. Yannouleas et al. revealed that concentration of individual excitations brings a collective excitation in alkali-metal clusters [3–6]. According to theorical studies of Yan et al. on linear neutral clusters of sodium, potassium, and silver, there are two modes in their excitation spectra, i.e., the longitudinal and transverse modes, of which transition moments increase with the cluster size [7, 8]. However, the mechanism of the growing intensity has not been revealed. Yasuike et al. evaluated "collectivity indices," which represent an effective number of individual excitations contributing to the excitation [9]. From the collectivity-index analysis for linear neutral sodium clusters, it was revealed that the size-dependent increase in the transition moment of the longitudinal mode originates from an increase in the charge-transfer distance, while that in the transverse mode is due to an increase in the collectivity index contributing to the excitation [9]. Yasuike et al.'s method is more quantitative and useful than that proposed by Guidez et al. [2, 10–13] treating configuration interaction coefficients qualitatively; Guidez et al. discussed the collectivity from a point of view of whether the excitation is generated by constructive addition of single-particle transitions or not.

In this chapter, absorption spectra of silver cluster cations are simulated by

employing time-dependent density-functional theory. Collectivity indices are also evaluated for the electronic excitations obtained to characterize their collectivity. Size-dependent evolution in the collectivity is discussed.

6.2. Computational procedures

The computational procedures are divided into three major steps: (a) geometry optimization, (b) simulation of absorption spectra, and (c) evaluation of collectivity indices. The geometry optimization was performed by the Gaussian 16 package [14], which was based on the density-functional theory [15, 16] employing the B3LYP functional [17, 18] and the basis set of LanL2DZ with the corresponding effective core potential [19]. Initial geometric structures were prepared by referring to previous theoretical studies on those of cationic [20] and neutral silver clusters [21]. The spin multiplicity was set to be singlet for odd N and doublet for even N. Normal mode analysis was also carried out to rule out geometries at saddle points on potential surfaces. Only the most stable structures were handled in the following steps. In the second step, spectral simulation was also carried out by the Gaussian 16 package. The calculation was based on the linear-response density-functional theory [22]. The CAM-B3LYP functional [23] and the basis set of LanL2DZ with the corresponding effective core potential were adopted. In the third step, collectivity indices were evaluated for excitations derived in the spectral simulation.

A detailed explanation of the collectivity index is available in Reference [9]. Here, its brief description is provided to present an overview. In the linear-response density-functional theory (LRDFT), a linear response of the molecule is derived from the solutions of the following eigenvalue problem:

$$\begin{pmatrix} \mathbf{A} & \mathbf{B} \\ -\mathbf{B} & -\mathbf{A} \end{pmatrix} \begin{pmatrix} \mathbf{X}^m \\ \mathbf{Y}^m \end{pmatrix} = \omega_m \begin{pmatrix} \mathbf{X}^m \\ \mathbf{Y}^m \end{pmatrix}, \tag{6.1}$$

where m is an index for the eigenstates, $\mathbf{X}^m$ and $\mathbf{Y}^m$ vectors formed by collecting amplitudes for particle–hole and hole–particle pair excitations, respectively, ω_m the eigenvalue, **A** and **B** matrices defined by the following equations,

$$\begin{aligned} A_{(i,a),(j,b)} &= (\varepsilon_a - \varepsilon_i)\delta_{ij}\delta_{ab} + 2K_{(i,a),(j,b)}, \\ B_{(i,a),(j,b)} &= 2K_{(i,a),(j,b)}, \\ K_{(i,a),(j,b)} &= \int \mathrm{d}\mathbf{r}\mathrm{d}\mathbf{r}' \phi_i(\mathbf{r})\phi_a(\mathbf{r}) \left(\frac{1}{|\mathbf{r}-\mathbf{r}'|} + \frac{\delta v_{\mathrm{XC}}(\rho)}{\delta\rho}\delta(\mathbf{r}-\mathbf{r}') \right) \phi_b(\mathbf{r}')\phi_j(\mathbf{r}'), \end{aligned} \tag{6.2}$$

i and j indices for occupied (hole) Kohn-Sham orbitals, a and b those for vacant (particle) Kohn-Sham orbitals, ε_i the orbital energy, δ_{ij} the Kronecker delta, **r** and **r** *'* position vectors, ϕ_i a Kohn–Sham orbital, $v_{\mathrm{XC}}(\mathbf{r})$ an exchange–correlation functional, and ρ the electron density. Note that (i,a) and (j,b) are orbital pairs specifying a row and a column of the matrix, respectively. The second step mentioned above is accomplished by solving this eigenvalue problem. The vectors $\mathbf{X}^m$ and $\mathbf{Y}^m$ satisfy the normalization condition:

$$\sum_{(i,a)} \left(X^m_{(i,a)} X^n_{(i,a)} - Y^m_{(i,a)} Y^n_{(i,a)} \right) = \delta_{mn}, \tag{6.3}$$

where m and n are indices for the eigenstates; the summation is performed over all the combinations of i and a. If the matrix **B** is negligible, the vector $\mathbf{Y}^m$ can be assumed to be **0**. In this case called the Tamm-Dancoff approximation (TDA), a transition density matrix $\mathbf{T}^m$ is formed from the vector **X** as $T_{i,a}{}^m = X_{(i,a)}{}^m$. The rectangular matrix $\mathbf{T}^m$ is transformed to a generalized diagonal form by the singular value decomposition with diagonal elements of $\lambda_1{}^m$, $\lambda_2{}^m$, etc., which gives the minimal representation of the excitation. The corresponding bases are called natural transition orbitals [24, 25]. Here, $\sum_{i,a} \left(T^m_{i,a} \right)^2 = \sum_{(i,a)} \left(X^m_{(i,a)} \right)^2 = 1$ holds from Equation (6.3). Because the summation of

squared matrix elements conserves before and after the singular value decomposition, $\sum_{i,a}\left(T_{i,a}^{m}\right)^2=\sum_{i=1}^{N_{\mathrm{occ}}}\left(\lambda_i^{m}\right)^2$, where N_{occ} is the number of occupied orbitals. Therefore, the diagonal elements satisfy the normalization condition $\sum_{i=1}^{N_{\mathrm{occ}}}\left(\lambda_i^{m}\right)^2=1$. In this condition, an inverse participation ratio

$$\nu_m^{*}=\frac{1}{\sum_{i=1}^{N_{\mathrm{occ}}}\left(\lambda_i^{m}\right)^4} \tag{6.4}$$

represents the effective number of individual excitations (pairs of natural transition orbitals) contributing to an excited state of interest: when $\lambda_1{}^m = 1$ and $\lambda_i{}^m = 0$ for $i \neq 1$, $\nu_m{}^*$ becomes 1, which represents that only one particle–hole pair contributes to the excitation. On the other hand, when contribution of all the excitation pairs is equal, i.e., $\lambda_i^{m}=\frac{1}{\sqrt{N_{\mathrm{occ}}}}$, $\nu_m{}^*$ becomes N_{occ}. The above description is based on the TDA, which does not hold in the general LRDFT. Yasuike et al. defined pseudo transition density matrices

$$T_{i,a}^{X^m}=\frac{X_{(i,a)}^{m}}{\sqrt{\sum_{(i,a)}\left(X_{(i,a)}^{m}\right)^2}},\ T_{i,a}^{Y^m}=\frac{Y_{(i,a)}^{m}}{\sqrt{\sum_{(i,a)}\left(Y_{(i,a)}^{m}\right)^2}} \tag{6.5}$$

for particle–hole and hole–particle excitation spaces, respectively. Inverse participation ratios for each excitation space, $\nu_{X^m}^{*}$ and $\nu_{Y^m}^{*}$, are obtained from the procedure described above, which are averaged to obtain the overall collectivity index

$$n_m^{*}=\left(\nu_{X^m}^{*}\right)^{K\sqrt{\sum_{(i,a)}\left(X_{(i,a)}^{m}\right)^2}}\left(\nu_{Y}^{*}\right)^{K\sqrt{\sum_{(i,a)}\left(Y_{(i,a)}^{m}\right)^2}},\ K=\frac{1}{\sqrt{\sum_{(i,a)}\left(X_{(i,a)}^{m}\right)^2}+\sqrt{\sum_{(i,a)}\left(Y_{(i,a)}^{m}\right)^2}}. \tag{6.6}$$

The concept similar to the collectivity index is proposed by Luzanov et al. for the first

time to discuss collectivity in electronic excitations of simple π-conjugated systems [26]. In addition, a similar approach was applied to Al_{13}^- by Casanova et al. [27] after the report of Yasuike et al. [9]. Luzanov et al.'s and Casanova et al.'s approaches only handle the contribution of the particle–hole excitation space $\mathbf{X}^m$. Generally, the contribution of the hole–particle excitation space $\mathbf{Y}^m$ becomes more significant as the silver cluster cations grow larger. Therefore, Yasuike et al.'s approach was adopted in the present study to treat both the excitation spaces. Note that the transition density matrix in the present study is defined as follows:

$$\mathbf{T}^m = \begin{bmatrix} \mathbf{T}_\alpha^m & \mathbf{0} \\ \mathbf{0} & \mathbf{T}_\beta^m \end{bmatrix}, \tag{6.7}$$

where $\mathbf{T}_\alpha{}^m$ and $\mathbf{T}_\beta{}^m$ are matrices formed by α-orbital- and β-orbital-components of $\mathbf{T}^m$, respectively. Therefore, collectivity indices thus obtained represent the effective number of electrons contributing to the excitation, which is different from Yasuike et al.'s definition [9].

Transition densities were calculated additionally. A transition density gives dynamical information of the electronic density of the molecule because it is proportional to the Fourier component of the time-dependent electronic density at the resonance frequency. In the framework of the linear-response density-functional theory, it is expressed by

$$\rho_{\mathrm{tr}}^{0m}(x,y,z) = \sum_{(i,a)} \sqrt{2}\left(X_{(i,a)}^m \phi_i(x,y,z)\phi_a(x,y,z) + Y_{(i,a)}^m \phi_a(x,y,z)\phi_i(x,y,z)\right). \tag{6.8}$$

Transition densities are depicted by the software VESTA [28] in the figures presented below.

In this study, the above calculations were performed for silver cluster cations in the size range of 2–40. The collectivity in electronic excitations of silver clusters is

discussed by considering optimized three-dimensional structures of the silver clusters beyond the model cases of linear/ring geometries treated in the previous studies [9, 27].

6.3. Geometric structures

The structures obtained by geometry optimization are depicted in Figure 6.1. Bond lengths are typically ~2.8 Å for smaller clusters, while those of larger clusters become larger in some cases; e.g., max ~3.2 Å for Ag_{40}^+. $Ag_{3,4,6}^+$ exhibited planar structures, while the other Ag_N^+ with N = 5, 7, and above were three-dimensional. In general, the geometries of Ag_N^+ ($N \geq 21$) were derivatives of icosahedra with adatoms as reported by Chen et al. for neutral silver clusters, Ag_N [21], despite the difference in the charge state and the method employed in the computation. In this section, the geometric structures obtained in the present study are compared with those in previous studies.

Ag_2^+. There are several experimental and theoretical studies on the bond length of the silver dimer. Weis et al. determined the length to be about 2.7 Å by ion mobility measurements [29]. Bonačić-Koutecký et al. reported the bond length of 2.85 and 2.69 Å in their theoretical studies employing relativistic effective core potentials for the one and 11 valence electrons of a silver atom [32, 33], respectively. The bond length was 2.80 Å in the present study, which is consistent with the previous reports.

Ag_3^+. All data available [29–35] support the D_{3h} equilateral-triangular structure, which was reproduced by the present calculation. A $D_{\infty h}$ linear structure was also employed as an initial structure, which was relaxed into the D_{3h} structure.

Ag_4^+. A D_{2h} planar rhombic structure was obtained, which is well-established by the previous reports [29–34, 36–41].

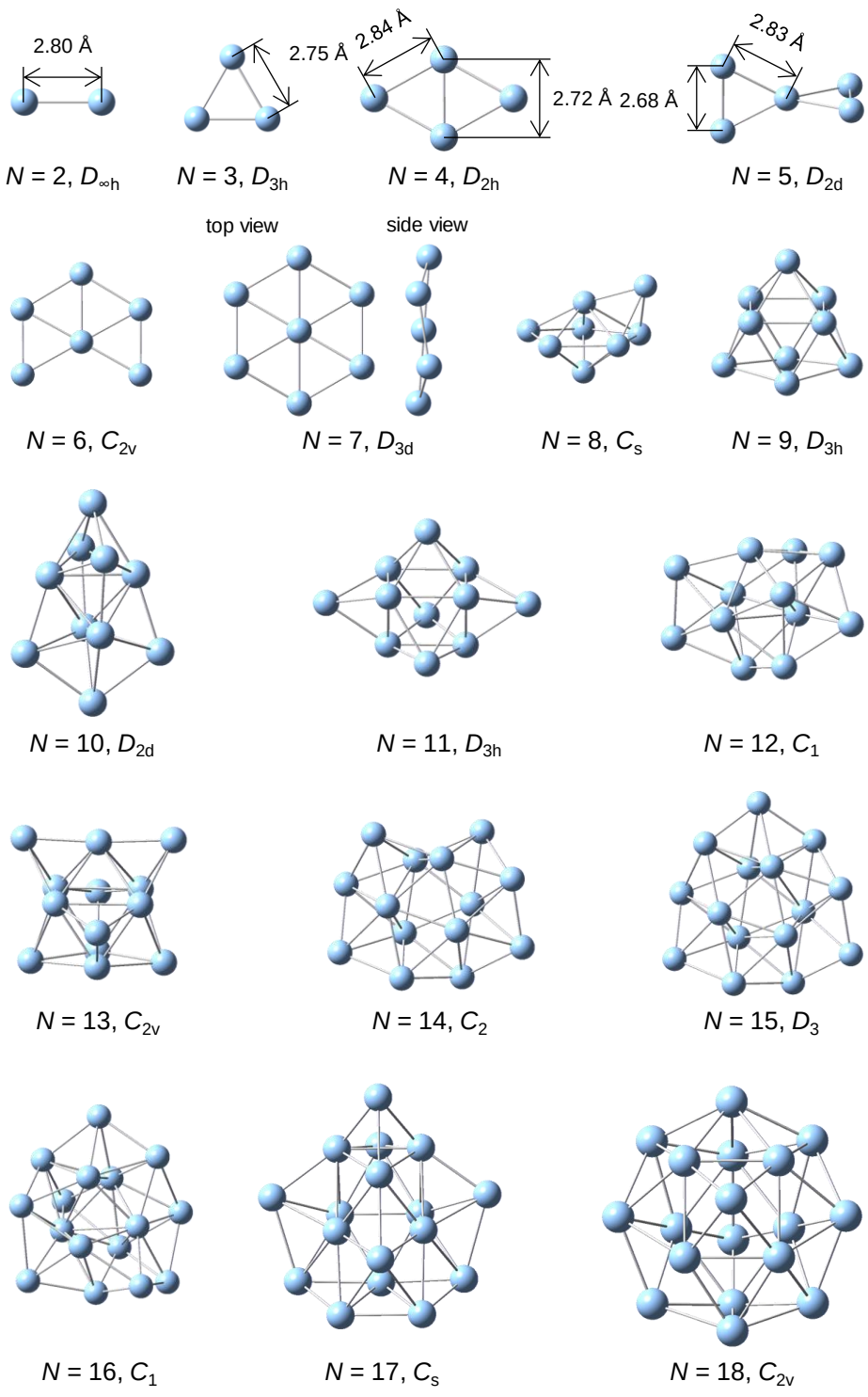

Figure 6.1. The most stable geometric structures of silver cluster cations, Ag_N^+ ($N = 2$–18), obtained by the present geometry optimization.

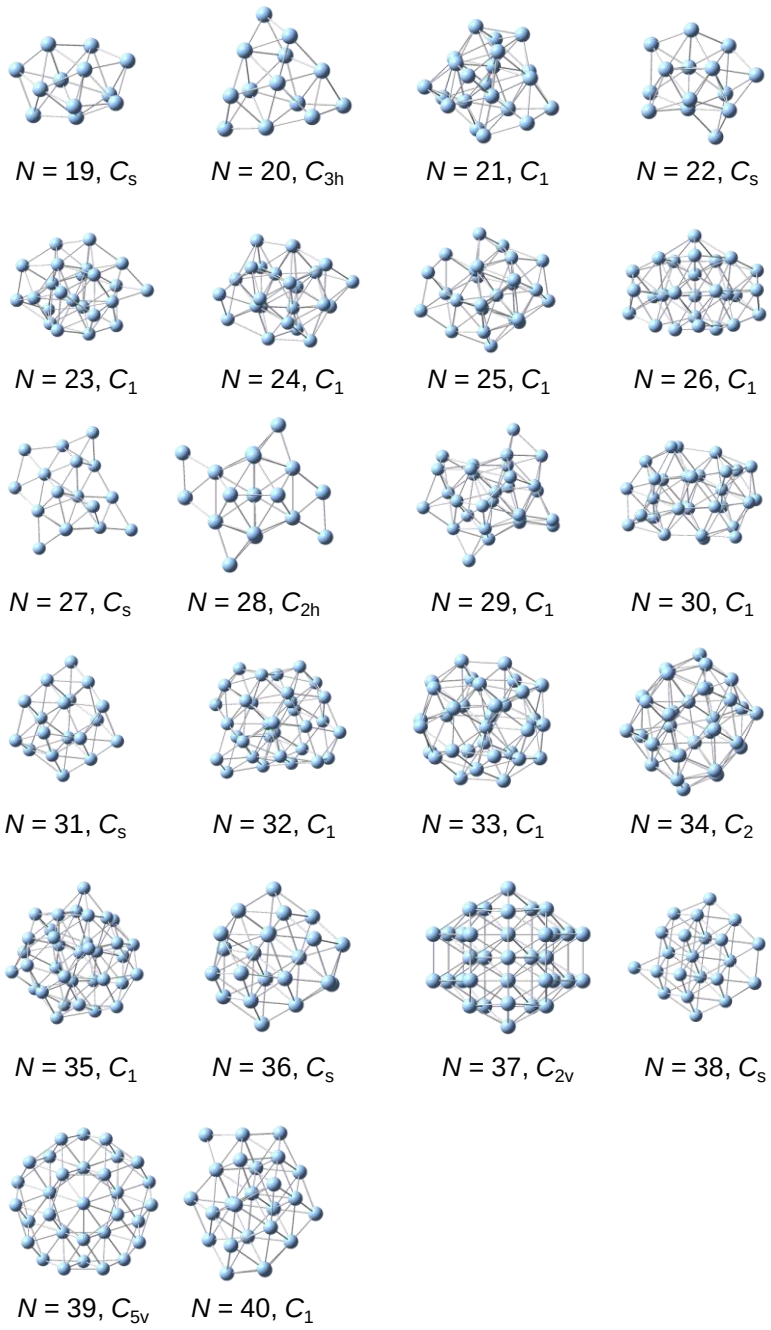

Figure 6.1 (cont.) The most stable geometric structures of silver cluster cations, Ag_N^+ (N = 19–40), obtained by the present geometry optimization.

Ag_5^+. A D_{2d} three-dimensional twisted X-structure was obtained. Many researchers reported the same twisted X-structure of Ag_5^+ as the most stable geometry [29–30, 34, 38]. In the theoretical study of Bonačić-Koutecký et al. [32], a D_{3h} trigonal bipyramid structure was reported to be the most stable, which was ruled out experimentally by Weis et al. [29]. The present study also confirmed that the trigonal bipyramid shows a saddle point on the potential energy surface and relaxed into the twisted X-shape. A D_{2h} planar X-structure is derived by changing the dihedral angle between two Ag_2 units, which was reported to be slightly less stable than the twisted one by 0.03 eV from the quantum chemical calculation by Weis et al. [29]. The energy difference was identical to that obtained in the present calculation as shown in Figure 6.2. Weis et al. also mentioned that the two isomers were essentially indistinguishable by ion mobility measurement because their rotationally averaged collision cross sections are completely identical. Therefore, the dihedral angle is considered to be free to vary around the central atom. This fluxional behavior will be discussed in more detail in Section 6.4.

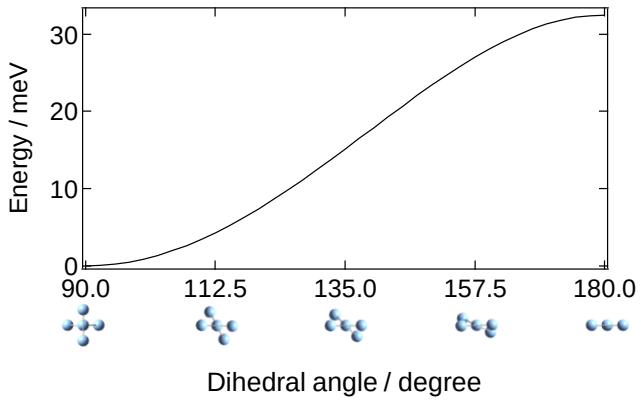

Figure 6.2. The energy of the X-shaped cationic silver pentamer as a function of its dihedral angle.

Ag_6^+. A planar structure was identified to be the most stable geometry in this study, which was ruled out both by previous experiments [29, 35] and by previous calculations [30–32]. They all reported a bicapped tetrahedron as a possible geometry of Ag_6^+. However, the present optimization resulted in a C_s geometry (see Figure 6.8 (b)) when it started from a bicapped tetrahedron as an initial structure; the C_s geometry possibly coexists with the planar structure in the present ion trap as will be mentioned in Section 6.4.

Ag_7^+. A D_{5h} pentagonal bipyramid structure (see Figure 6.9 (d)) has been reported as the most possible structure of Ag_7^+ by previous reports [29–32, 35]. In the calculation by Weis et al., a D_{6h} hexagonal planar structure was obtained as a metastable structure but was ruled out due to its total energy higher than that of the pentagonal bipyramid [29]. Van der Tol et al. obtained a hexagonal structure where the central atom is slightly out of the molecular plane, which was also ruled out because their infrared multiple photon dissociation spectrum of $Ag_7Ar_{1,2}^+$ was not reproduced by the geometry [35]. In the present calculation, the D_{6h} planar structure was not obtained as a stable geometry, as was not the case also in Ito's reports [30, 31]; instead, it was relaxed into the nonplanar D_{3d} structure shown in Figure 6.1, where the atoms at the rim of the molecular frame are located out of the plane alternately. The D_{5h} structure was energetically less stable than the D_{3d} structure by 0.30 eV in the present optimization, which possibly coexists in the present ion trap as described in Section 6.4.

Ag_8^+. The well-established pentagonal bipyramid with an adatom [29–31, 35] was obtained in the present calculation as well.

Ag_9^+. A D_{3h} tricapped trigonal prism structure was obtained as the most stable one, which coincides with the previous report of Weis et al. [29]. Some researchers

reported a C_{2v} pentagonal bipyramid with two adatoms (see Figure 6.10 (b)) is more stable than the tricapped trigonal prism by 0.01–1.26 eV depending on the basis sets and functionals [30–32]. In the present calculation, the pentagonal bipyramid was also obtained as an isomer with a total energy higher than that of the tricapped trigonal prism by 0.02 eV. Therefore, the isomers possibly coexist in the present ion trap. The coexistence will be reviewed in Section 6.4.

Ag_{10}^+. A D_{2d} pentagonal bipyramid with three adatoms was obtained as the most stable one in the present calculation, which coincides with the previous reports [30, 31, 35]. A C_s metastable geometry (see Figure 6.11 (b)) was also obtained, which was less stable than the pentagonal bipyramid by 0.04 eV. Weis et al. reported the C_s structure cannot be ruled out experimentally [29], while other reports did not consider it. Therefore, the two isomers should be considered to explain the experimental result, which will be reviewed in Section 6.4.

Ag_{11}^+. A D_{3h} pentacapped trigonal prism was obtained in the present calculation, which was in line with the previous report of Weis et al. [29]. A C_{3h} structure similar to the D_{3h} structure was also reported by van der Tol et al. [35]. A motif of the pentacapped trigonal prism was concluded to be possible.

Ag_{19}^+. There are few studies for cluster sizes above 12. The trapped-ion-electron-diffraction study by Blom et al. is the only report on the geometry of Ag_{19}^+, which revealed that Ag_{19}^+ has three experimentally indistinguishable icosahedral-type structures, i.e., a D_{5h} double icosahedron sharing a common pentagon and two types of C_s icosahedra with a group of six adatoms at different sites [42] (see Figure 6.3). The former icosahedra were reported to be isoenergetic within ~0.1 eV and more stable than the latter by ~0.4–0.6 eV. The present calculation reproduced the previous result

approximately. One of the C_s structures shown in Figure 6.1 is more stable than the other by 0.09 eV. The D_{5h} structure was less stable by 0.7 eV than the one in Figure 6.1.

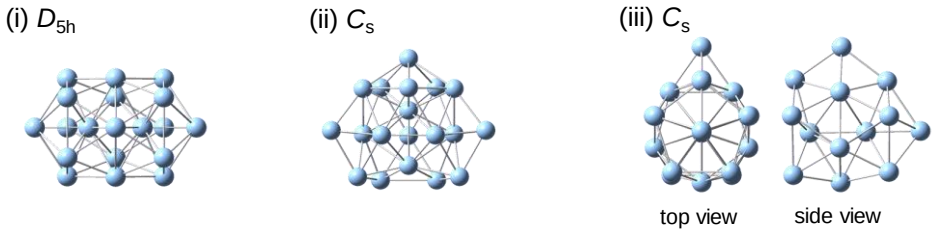

Figure 6.3. Geometries obtained by Blom et al. [42].

Ag_{38}^+. Blom et al. studied the geometric structure of Ag_{38}^+ previously [42]. They obtained four types of stable geometries, i.e., a C_1 incomplete truncated decahedron, two C_1 incomplete icosahedra, and a truncated octahedron. They ruled out the truncated octahedron and concluded that a mixture of the decahedron and icosahedra or a very flexible structure was observed, which is consistent with the previous report by Xing et al. [43]. An C_s incomplete truncated decahedron similar to that obtained by Blom et al. was obtained as the most stable geometry also in the present calculation.

6.4. Spectral simulation

Simulated absorption spectra are shown in Figure 6.4, where the geometric structures in Figure 6.1 were employed. To convert the oscillator strengths theoretically obtained to absorption cross sections, a Gaussian profile

$$\sigma(E) = \sigma_0 \exp\left(-4\ln 2 \left(\frac{E - E_0}{E_w} \right)^2 \right) \tag{6.9}$$

is assumed for each transition, where E is the photon energy, E_0 the resonance energy, σ_0

the maximum absorption cross section, E_w the full width at half maximum (FWHM). By substituting this profile into Equation (5.9), Equation (6.10) is derived, which determines the relation among the oscillator strength f, the maximum cross section σ_0, and FWHM E_w:

$$f = 0.970(\sigma_0/\text{Å}^2)(E_w/\text{eV}). \quad (6.10)$$

E_w was set to 0.2 eV for all sizes, which corresponds to that of the Gaussian-like absorption band of the silver trimer cation. In this section, the theoretical results are shown in comparison with the experimental results to confirm reliability of the theoretical spectra prior to the analysis that follows. The descriptions focus mainly on clusters of which experimental spectra were reproduced by the calculation.

Ag_2^+. Two major transitions were obtained in the simulation at 3.03 and 3.73 eV, respectively. The former, the first dipole-allowed transition, reproduces the photon energy of the band observed experimentally, while, as for its oscillator strength, the experimental result of 0.1041 is about 55% of the theoretical value of 0.1798. One of the well-known theoretical studies on the optical absorption of the dimer cation was reported by Bonačić-Koutecký et al. [33]. In the present experimental spectral range of 2.8–5.0 eV, two excitations were found at 3.15 and 3.85 eV in their report. The oscillator strengths of the excitations were 0.08 and 0.17, respectively. The excitation energy was consistent with the present calculation. On the other hand, the oscillator strength at the lower energy was about 45% of the present calculation, which rather coincides with the present experiment.

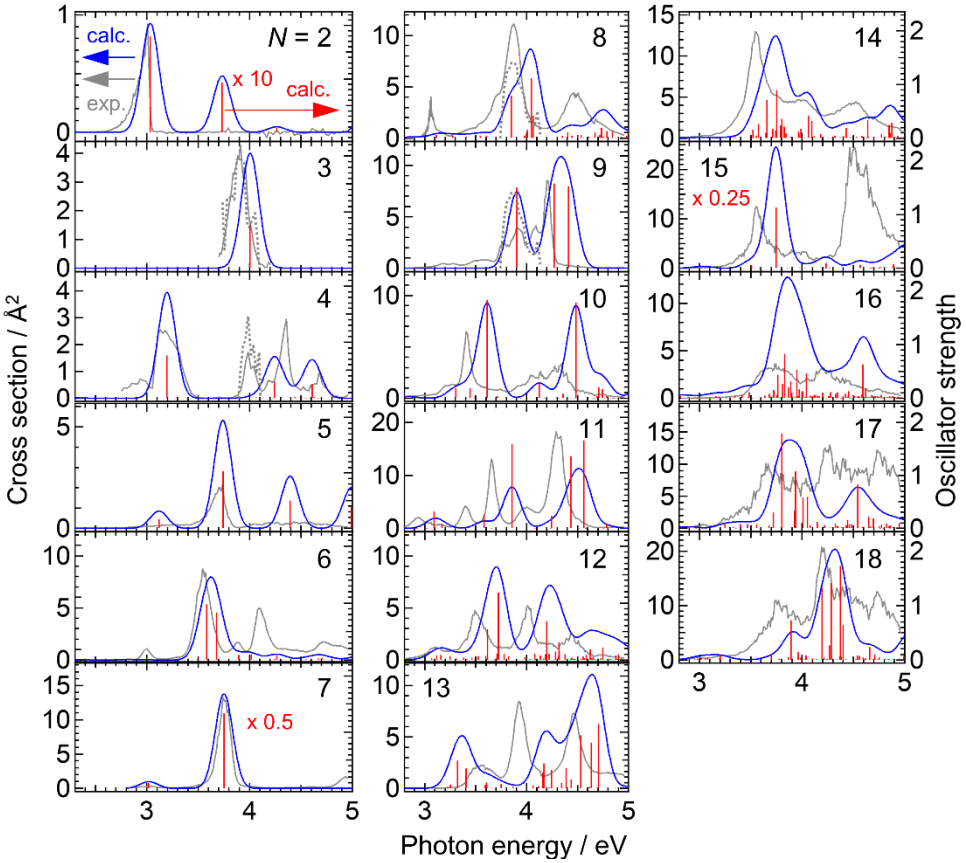

Figure 6.4. The results of spectral simulation for silver cluster cations, Ag_N^+ (N = 2–18). Red sticks (|): oscillator strengths obtained by the present calculation. Blue solid curves (—): absorption spectra simulated by assuming Gaussian profiles with full width at half maximum of 0.2 eV for each transition. Gray solid curves (—): the present photodissociation spectra. Gray dashed curves (- - -): the present photoabsorption spectra. The oscillator strengths of N = 2, 7, and 15 and the experimental results of N = 15, 17, and 18 are scaled for visibility.

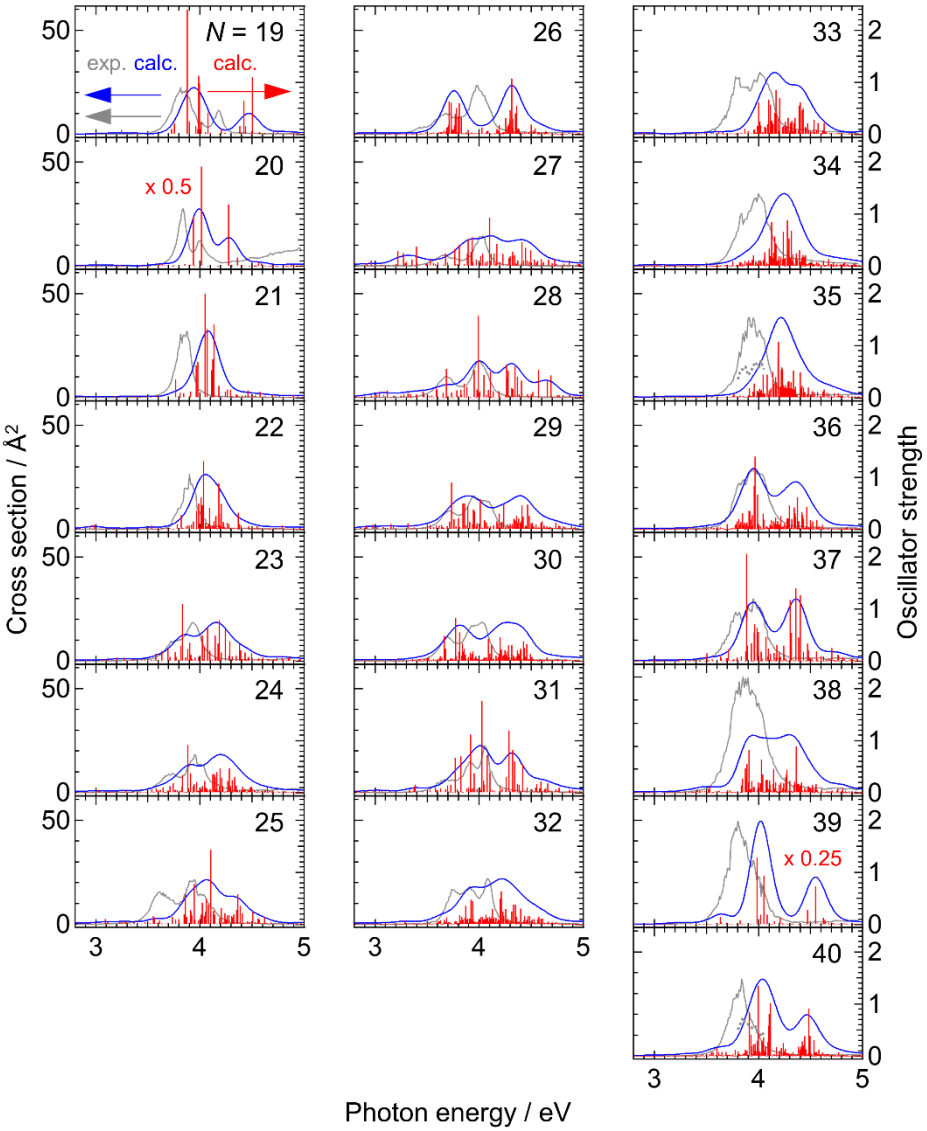

Figure 6.4 (cont.) The results of spectral simulation for silver cluster cations, Ag_N^+ (N = 19–40). All the photodissociation spectra are scaled to match the maxima of experimental normalized dissociation yield and the simulated absorption cross section for visibility.

Another discrepancy between the present theoretical and experimental data is the transition theoretically predicted at 3.73 eV. It is reported for Na_2^+ that absorption leading to a bound excited state exhibits an extremely low photodissociation cross section

[44]. In this context, a potential energy surface of the second dipole-allowed excited state at the photon energy of 3.73 eV was simulated as well as those of the ground and first dipole-allowed excited states. As shown in Figure 6.5 (a), the second excited state at 3.73 eV is a bound state, which is explained by an energy diagram for molecular orbitals of the dimer depicted in Figure 6.5 (b); the second dipole-allowed excited state is dominated by the transition from beta d σ_u to beta s σ_g to strengthen the bond. Internal conversion does not happen because there is no vibrational level in the ground state to interact with the bonding state. In addition, probably, there is no upper level resonant to the photon energy of 3.73 eV upon multi-photon absorption. Therefore, the corresponding absorption was not detected in the present photodissociation spectroscopy. On the other hand, the transition between alpha s σ_g to alpha s σ_u is dominant in the first dipole-allowed excited state, which results in a dissociative potential surface leading to dissociation without internal conversion.

Ag_3^+. Only one transition was obtained in the simulation. It comes from a doubly degenerate excitation with an oscillator strength of 0.78 in total, where the transition densities of the two excitations are orthogonal to each other in the molecular plane. The energy approximately coincides with the experimental value. The cross sections are also identical.

Theoretical prediction of the trimer was also carried out by Bonačić-Koutecký et al. [33]. Their result exhibited doubly degenerate excitations at 4.11 eV with an oscillator strength of 0.80 in total inside the present experimental spectral range, which coincides with the present calculation.

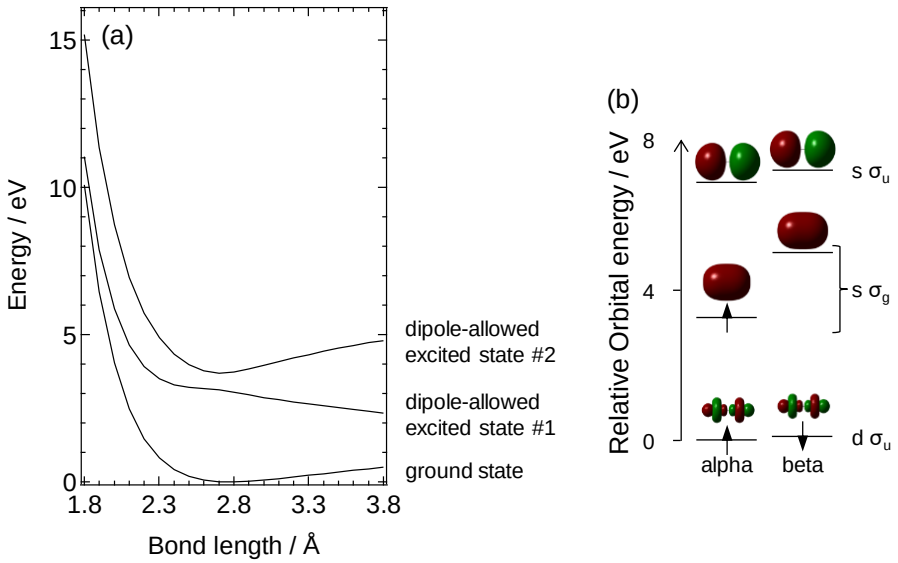

Figure 6.5. (a) The potential energy curves of the silver dimer cation. The ordinate corresponds to the energy with respect to the ground state with a bond length of 2.80 Å. (b) An energy diagram for molecular orbitals of the dimer. Only orbitals relevant to excitations of interest are shown.

Ag_4^+. The assignment is difficult for this size. Experimentally, five bands were observed at 2.97, 3.14, ~4.0, 4.35, and 4.68 eV. Among them, those at 3.14, 4.35, and 4.68 eV were reproduced by the theoretical transitions of the most stable D_{2h} geometry at 3.20, 4.24, and 4.61 eV, respectively. Spectral simulation was also performed for the metastable C_{2v} Y-shaped structure found in the present study as shown in Figure 6.6. The theoretical transitions at 3.08 and 4.08 eV are likely to contribute to the experimental bands at 2.97 and ~4.0 eV, respectively. The C_{2v} geometry is less stable than the D_{2h} geometry by ΔE = 0.13 eV. If the Boltzmann distribution holds, the population of the C_{2v} geometry relative to that of the D_{2h} geometry is $\exp\left(-\frac{\Delta E}{k_B T}\right)$ ~ 1% at the temperature T of 300 K, where k_B is the Boltzmann constant. The reason why

such an energetically minor isomer was detected may be as follows: the clusters initially energized are cooled during cluster generation to be trapped at local minima of the potential energy surface, where they cannot obtain a sufficient activation energy to overcome potential barriers to transform their geometries.

The present calculation was also compared with the previous study by Bonačić-Koutecký et al. [33, 45]. For the D_{2h} planar structure, three intense excitations were found in their report at 3.25, 4.26, and 4.67 eV in the spectral range of 2.8–5.0 eV, which were replicated by the present calculation. On the other hand, their spectral simulation for the C_{2v} Y-shaped structure showed an absorption spectrum similar to that of the planar structure; the transition at 4.26 eV loses its oscillator strength to result in two transitions in the spectral range of interest without a significant energy shift. Therefore, the simulated spectra in the present study reproduce the experimental data better than the previous simulation.

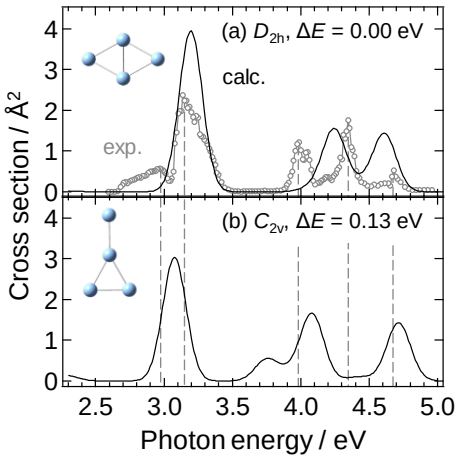

Figure 6.6. The experimental and theorical absorption spectra of Ag_4^+ for the most stable and metastable geometries. The point groups, the energy ΔE relative to the most stable geometry, and the geometric structures are also shown.

Ag_5^+. An intense band was observed experimentally at 3.73 eV, which was accompanied by weaker humps located above 3.9 eV. The experimental feature was not reproduced by the simulated absorption spectrum of the most stable D_{2d} structure. As mentioned in Section 6.3, two Ag_3 planes can rotate around the central atom easily. The spectral simulation was carried out as a function of dihedral angle between the two Ag_3 planes with constant bond lengths as shown in Figure 6.7. In panel (b), the angle of 90°, i.e., the D_{2d} structure, yielded a multi-modal profile. The maximum at 3.12 eV originates from doubly degenerate transition densities, where dipolar transition densities exist in each Ag_2 unit. The most intense maximum at 3.74 eV corresponds to the electron oscillation along the symmetry axis, while that at 4.39 eV originates from doubly degenerate transition densities, where dipolar electron oscillation in one of the Ag_2 units contributes. By rotating one of the Ag_3 planes by 45°, i.e., the D_2 structure in panel (d), the maximum at 3.12 eV is split into two maxima; the one at the lower energy shows a quadrupolar transition density, which results in an extremely low oscillator strength. On the other hand, in-phase superposition of the dipolar transition densities in each Ag_2 unit at 3.12 eV shifts the transition to 3.51 eV. The maximum observed for the D_{2d} structure at 3.74 eV stays as it is at the angle of 45°. The maximum of the D_{2d} structure located at 4.39 eV is split into two maxima due to interaction between the doubly degenerate transition densities. At the planar structure in panel (f), the quadrupolar transition density observed for the D_2 structure loses all the oscillator strength. Therefore, the corresponding maximum completely vanishes. The most intense maximum originates from doubly pseudo degenerate transitions: one is the electron oscillation in the molecular plane, while the other originates in the oscillation along the symmetry axis. The maxima at 4.06 and 4.88 eV are caused by the dipolar and quadrupolar transition densities,

respectively; the latter has no oscillator strength because it is dipole forbidden. To summarize the spectral features as a function of dihedral angle, the most intense maximum around 3.7 eV is not affected by the angle, while the maximum at the lower-energy side is weakened as the geometry becomes planar. The maximum at the higher-energy side splits as the structure changes closer to planar. The resonance energy varies depending on the dihedral angle. The overall absorption cross section $\sigma_{\mathrm{abs}}^{\mathrm{tot}}$ becomes

$$\sigma_{\mathrm{abs}}^{\mathrm{tot}}(E) = \int_0^{2\pi} \mathrm{d}\theta \; p(\theta)\sigma_{\mathrm{abs}}(E,\theta), \tag{6.11}$$

where $\sigma_{\mathrm{abs}}(E, \theta)$ is the absorption cross section at a photon energy of E for the geometry with the dihedral angle θ found with the probability of $p(\theta)$. Because it is not realistic to simulate absorption spectra for all geometries, the equation is approximated by

$$\begin{aligned}
\sigma_{\mathrm{abs}}^{\mathrm{tot}}(E) \sim\; & p(90^\circ)\sigma_{\mathrm{abs}}(E,90^\circ) + p(112.5^\circ)\sigma_{\mathrm{abs}}(E,112.5^\circ) \\
& + p(135^\circ)\sigma_{\mathrm{abs}}(E,135^\circ) + p(157.5^\circ)\sigma_{\mathrm{abs}}(E,157.5^\circ) \\
& + p(180^\circ)\sigma_{\mathrm{abs}}(E,180^\circ), \\
p(\theta) = & \frac{g(\theta)\exp\left(-\dfrac{\Delta E(\theta)}{k_{\mathrm{B}}T}\right)}{\sum g(\theta)\exp\left(-\dfrac{\Delta E(\theta)}{k_{\mathrm{B}}T}\right)}, \; g(\theta) = \begin{cases} 1 & (\theta = 90^\circ, 180^\circ) \\ 2 & (\text{otherwise}) \end{cases}.
\end{aligned} \tag{6.12}$$

where $g(\theta)$ is the degeneracy factor and $\Delta E(\theta)$ the energy relative to that at $\theta = 90°$. The total absorption spectrum reproduced the experimental spectrum as shown in panel (a); especially, the structureless experimental band at the larger energy side is explained as multiple excitations originating from the internally rotating molecule. It is concluded that the twisted X-shaped heptamer rotated around the symmetry axis in the present ion trap, which resulted in the experimental photodissociation spectrum. This is the first identification of such isomers; they were experimentally undistinguishable by the previous ion mobility measurements [29].

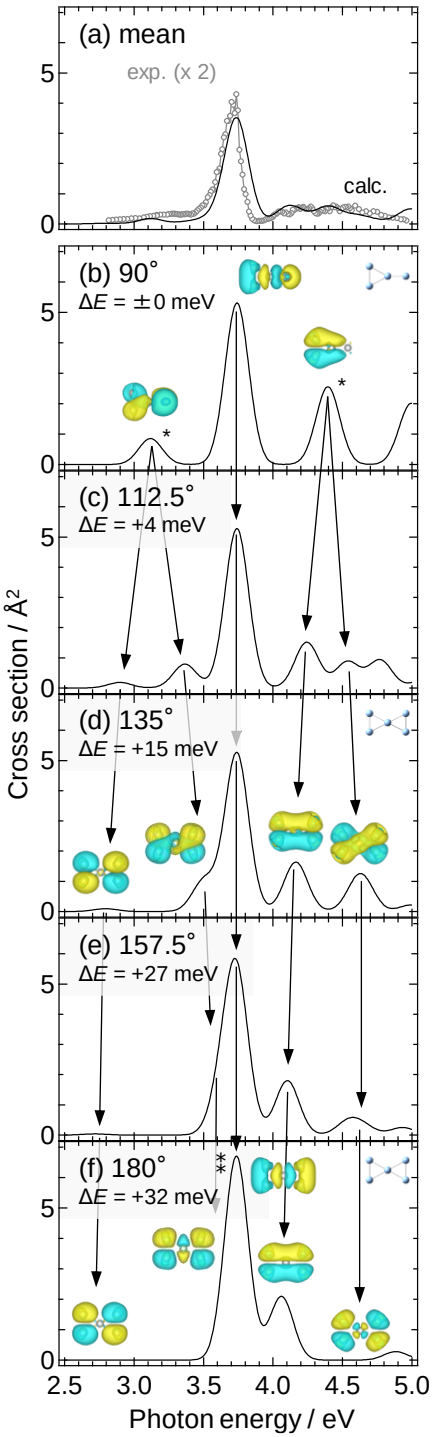

Figure 6.7. The experimental and theorical absorption spectra of Ag_5^+ as a function of dihedral angle. The former is multiplied by two for visibility. Transition densities are depicted adjacent to corresponding excitations. *Doubly degenerate. **Doubly pseudo degenerate.

Ag_6^+. A multi-modal profile was observed experimentally, where the bands were located at 3.00, 3.54, 3.89, 4.09, and 4.71 eV. Only the band at 3.54 eV was reproduced by the most stable C_{2v} geometry. Two metastable geometries were found in the present calculation. The experimental bands at 4.09 and 4.71 eV were reproduced by the C_s geometry, while that at 3.00 eV was replicated by the C_{2v} geometry as shown in Figure 6.8.

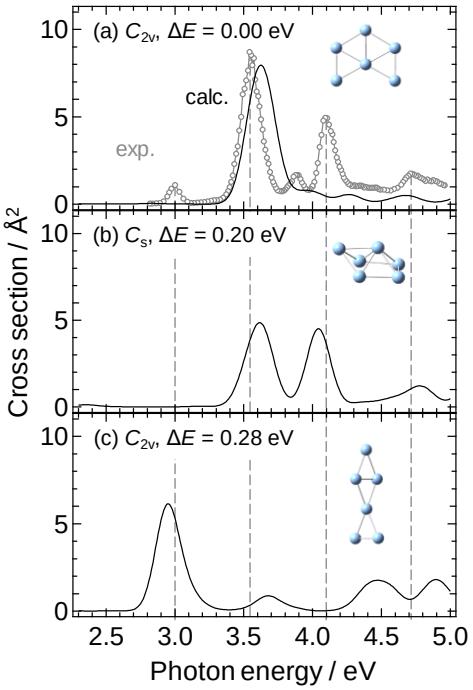

Figure 6.8. The experimental and theorical absorption spectra of Ag_6^+ for the most stable and metastable geometries.

Ag_7^+. The most stable D_{3d} geometry reproduced the main band located at 3.75 eV in the experimental result, while the absorption band experimentally observed at 4.93 eV was not reproduced by this geometry. Additional calculations for metastable

geometries shown in Figure 6.9 imply their contributions to the absorption band at 4.93 eV; all of the three metastable geometries exhibit transitions corresponding to the experimental main band at 3.75 eV. The C_{2v} geometry in panel (c) is excluded because the predicted satellite transition at 4.05 eV is not observed experimentally. The C_{2v} geometry in panel (b) and the D_{5h} geometry in panel (d) show weak transitions at 4.71 and 4.74 eV, respectively, which might correspond to the experimental band at 4.93 eV. Therefore, these structures probably coexist in the present ion trap.

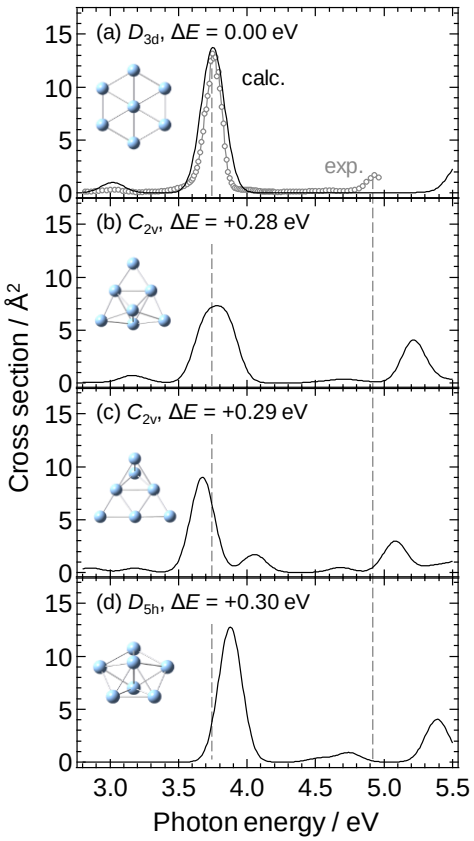

Figure 6.9. The experimental and theorical absorption spectra of Ag_7^+ for the most stable and metastable geometries.

Ag_8^+. The most stable geometry reproduced the experimental result.

Ag_9^+. The experimental bands at 3.90 and 4.21 eV were reproduced by the theoretical maxima at 3.90 and 4.34 eV, respectively. Other bands observed in photodissociation spectroscopy are explained by the metastable geometry with C_{2v} symmetry. The result of additional calculation for the C_{2v} geometry is shown in Figure 6.10 as well as that of the most stable D_{3h} geometry. The experimental bands at ~3.2, 3.60, and 4.10 eV were reproduced only by the C_{2v} geometry. In a previous report on a photodissociation spectrum of Ag_9^+ in comparison with theoretical calculation [30], the experimental spectrum was reproduced by two isomers, which have the same geometries as those in this study. The difference between the present study and the previous report is the relative energy of the geometries; the D_{3h} geometry was reported to be less stable than the C_{2v} geometry by 13.7 meV because of the basis set employed in Ref. [30], i.e., LanL2DZ modified by Couty et al. [46]. The energy difference between the D_{3h} and C_{2v} geometries are so small that it should be natural to expect that the isomers coexist in the ion trap.

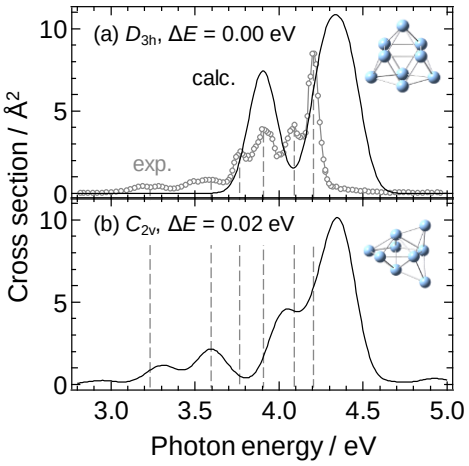

Figure 6.10. The experimental and theorical absorption spectra of Ag_9^+ for the most stable and metastable geometries.

Ag_{10}^+. The simulated spectrum of the D_{2d} pentagonal bipyramid partially reproduced the experimental spectrum; the theoretical maximum at 3.61 eV corresponds to the experimental band at 3.41 eV, while the intense maximum predicted at 4.48 eV was not observed experimentally. Instead, a broad absorption band was located at 3.8–4.5 eV, which was replicated rather by the simulation employing a C_s structure as shown in Figure 6.11. Therefore, the two isomers would have coexisted in the present ion trap.

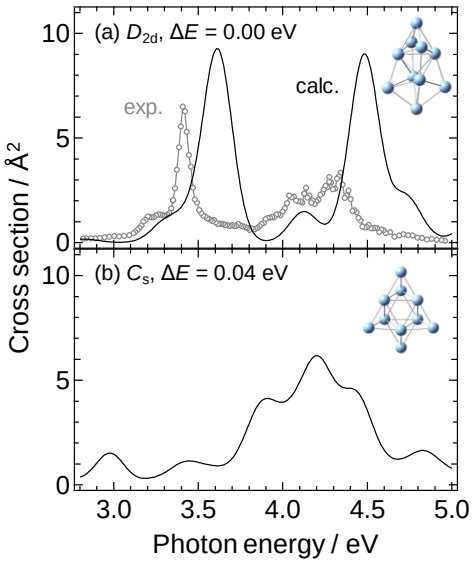

Figure 6.11. The experimental and theorical absorption spectra of Ag_{10}^+ for the most stable and metastable geometries.

Ag_{11}^+. Five bands were observed in the present photodissociation spectroscopy, which are located at 2.93, 3.40, 3.66, 4.00, and 4.29 eV. Among them, those at 2.93, 3.66, and 4.29 eV were replicated by the simulation employing the most stable D_{3h} structure, which predicts the corresponding maxima at 3.11, 3.86, and 4.51 eV, respectively. On the other hand, the bands experimentally observed at 3.40 and 4.00 eV

were not predicted. Theoretical prediction of the absorption spectrum of a metastable C_{2v} structure was performed additionally as shown in Figure 6.12. The predicted peaks at 3.48 and 4.27 eV seem to correspond to the experimental bands at 3.40 and 4.00 eV, respectively. Therefore, the two isomers would have coexisted in the present ion trap.

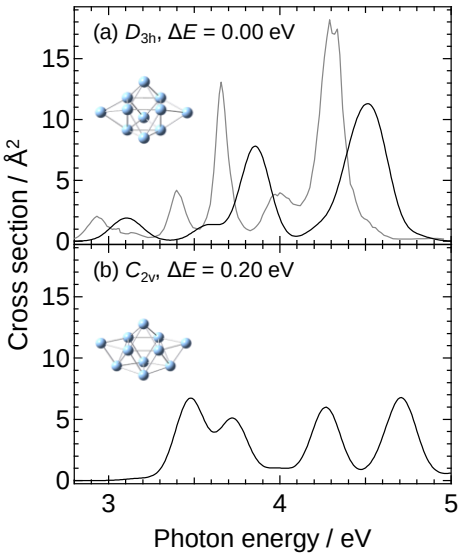

Figure 6.12. The experimental and theorical absorption spectra of Ag_{11}^+ for the most stable and metastable geometries.

$Ag_{12,\ 13}^+$. Four/three absorption bands were observed experimentally for Ag_{12}^+/Ag_{13}^+, which were reproduced by the theoretical calculation.

Ag_{14}^+. The experimental and theorical spectra coincided well with respect to the resonance energy, the spectral profile, and cross sections.

$Ag_{15–18}^+$. The predicted absorption spectra showed intense bands with the maximum cross sections of 14–25 Å^2. In Figure 6.4, the present photodissociation spectra are superimposed for comparison, which is scaled by a factor of 10 for visibility.

The predicted absorption cross sections were extremely higher than those measured by photodissociation spectroscopy, especially for $Ag_{15,17,18}^+$, where one-photon and two-photon dissociation processes take place at the same time; the contribution of one/two-photon dissociation depends on the wavelength of the incident laser. Because the photodissociation cross sections are calculated on the assumption that all the clusters dissociated upon one-photon absorption, the experimental cross sections at lower energies should be underestimated for clusters dissociating upon two-photon absorption.

Ag_{16}^+ also showed small absorption cross sections experimentally, despite of dissociation upon one-photon absorption. The laser power required for Ag_{16}^+ to dissociate is so weak that the irradiation might not induce two-photon absorption because of its large absorption cross section (estimated to be max. 13 $Å^2$ in the present calculation) and a low dissociation energy (reported to be 2.05 eV, which is lower than those of $Ag_{15,17,18}^+$ by 0.3–0.5 eV [47]). The photodissociation cross sections lower than those predicted by the calculation might be due to deexcitation by collision with a buffer helium gas that competes with dissociation as discussed in Chapter 4.

$Ag_{19–24,29,30,34,35,37}^+$. Photodissociation cross sections could not be determined experimentally due to the two-photon process; the photodissociation spectra cannot be compared with theoretical counterparts quantitatively. On the other hand, spectral shapes of the photodissociation spectra are meaningful. The spectral profiles were reproduced by the theory: single-band profiles for $Ag_{21,22,34,35,37}^+$ and bimodal profiles for $Ag_{19,20,23,24,29,30}^+$ are recognized in both the present photodissociation and theoretical spectra. Especially, the present photoabsorption spectrum of Ag_{35}^+ matches with the theoretical counterpart by considering the large systematic error in the experimental data which originates from uncertainty in the density of the parent ions.

The others. The theoretical spectral profiles of $Ag_{25–28,31–33,36,38–40}^{+}$ did not agree with the experimental spectra. This is because the geometric structures theoretically obtained would be different from those in the experiment. For example, Ag_{39}^{+} exhibited a single absorption peak experimentally. From Equation (4.29) according to Schmidt et al., the single-peak profile indicates a spherical geometry. On the other hand, the geometry obtained theoretically was rather oblate. By solving Equation (4.36) for the C_{5v} structure of Ag_{39}^{+} in Figure 6.2, the geometry is approximated by an oblate spheroid with $r_x = r_y = 6.1$ Å and $r_z = 4.3$ Å, i.e., an aspect ratio of 0.70. In this case, the two major peaks predicted theoretically originate from electron oscillations along the longer and shorter axes, which was confirmed by calculating their transition densities.

Comparison with neutral silver clusters. It is difficult to compare absorption spectra of clusters with different charge states. Therefore, the result of the comparison is described briefly here. Many groups have been reported theoretical photoabsorption spectra of neutral silver clusters [33, 48, 56, 49]. In the reports of Bonačić-Koutecký et al. [33, 45], possible geometries of neutral silver clusters with the sizes of 2–4 are a linear structure with a shorter bond length than that of the cationic counterpart, a C_{2v} triangle due to the Jahn–Teller effect, and a D_{2h} planer rhombic structure, respectively: they all have geometries similar to the cationic counterparts. On the other hand, spectral profiles, excitation energies, and oscillator strengths are different between predicted spectra for the neutrals and cations in their reports. Harb et al. reported remarkable results of theorical calculation for Ag_N (N = 4–20), which reproduced their experimental absorption spectra [48]. The simulated spectra are generally different from those obtained in the present simulation because of the differences in the charge state and geometry. A few

exceptions are N = 14, 20, and 22, where both the geometries and simulated absorption spectra were similar to each other between the present and previous studies. This is probably because the difference in the charge state does not affect geometries and electronic states of clusters significantly above N = 14. The same trend was recognized from comparison with other previous reports on Ag_{20} [49–54], Ag_{22} [51, 54, 55], Ag_{35} [52, 56], and their cationic counterparts. On the other hand, the absorption spectrum of Ag_{38}^{+} predicted in the present study did not match with that of its neutral counterpart reported by Schira et al. [56]. The difference originates from the geometric structures employed in the calculation; oblate in the present study, while spherical in the previous study. Schira et al. obtained the structure by geometry optimization employing a O_h structure previously obtained by Chen et al. [21]; however, the O_h structure was found to be at a saddle point of the potential energy surface in the present study.

To summarize this section, the experimental spectra of the clusters were explained well by theoretical predictions, especially for the sizes of 2–14, 19–24, 29, 30, 34, and 35. The following analysis was performed by focusing on these sizes with the most stable geometries in Figure 6.1 and predicted excitations in Figure 6.4.

6.5. Collectivity indices and oscillator strengths of eigenstates

In the third step of the present computational work, collectivity indices are evaluated for each cluster. For smaller clusters, the situation is simple; there are only several excitations in the spectra. For larger clusters, in contrast, a large number of excitations contribute to the absorption spectra. Therefore, the collectivity indices distribute in a wide energy range, which makes the analysis complicated. To simplify the analysis, the author defines the averaged collectivity index weighted by oscillator

strengths f_i:

$$\left\langle n^* \right\rangle = \frac{\sum_i f_i n_i^*}{\sum_i f_i}, \tag{6.13}$$

where the subscript i identifies each excitation. The summation was performed over the spectral range where major excitations are covered as shown in Table 6.1. The averaged collectivity index is depicted as a function of cluster size in Figure 6.13 (a) as red open circles. The theoretical result indicates that the collectivity index has an increasing trend as the cluster grows into larger sizes. Oscillator strengths and their concentration were also evaluated; here the author defines a total oscillator strength, f_{total}, an average energy, E_{average}, and an effective spectral width, d, as follows:

$$\begin{aligned} f_{\text{total}} &= \sum_i f_i, \\ E_{\text{average}} &= \frac{\sum_i E_i f_i}{\sum_i f_i}, \\ d^2 &= \frac{\sum_i \left(E_i - E_{\text{average}} \right)^2 f_i}{\sum_i f_i}, \end{aligned} \tag{6.14}$$

where the summation was performed over the same spectral range as shown in Table 6.1. The result is depicted in Figure 6.14, where the corresponding result in Figure 5.5 is superimposed for comparison. The total oscillator strength showed an increasing trend and replicated the experimental result except for $N = 35$ where the experimental data have large uncertainty originating from evaluation of an ion density. The effective width reproduced qualitatively the experimental result as well; the theoretical widths were systematically smaller than those in the experimental data because broadening of spectral widths due to, e.g., thermal broadening is not considered in the calculation. Especially, a local minimum at $N = 21$ and a decreasing trend toward $N = 40$ reminds us of spherical

structures of silver cluster cations predicted by the Clemenger–Nilsson model discussed in Chapter 4 (see Figure 4.13), which results in local maxima of the density of oscillator strengths, f_{total}/d, in Figure 6.14 (c) corresponding to collective excitation of electrons.

Table 6.1. The excitations considered for evaluating averaged collective indices.

Cluster size	Energy range / eV	Cluster size	Energy range / eV
2	3.03*	19	3.6–4.6
3	4.01‡	20	3.8–4.5
4	3.1–4.8	21	3.7–4.4
6	3.5–3.8	22	3.8–4.5
7	2.9–3.9	23	3.5–4.7
8	3.7–4.9	24	3.4–4.8
9	3.8–4.5	29	3.5–5.0
12	3.0–5.0	30	3.6–4.7
13	3.1–4.8	34	3.7–4.6
14	3.4–5.0	35	3.9–4.6
16	3.6–5.0		

*Only one eigenstate exists in the energy range. ‡Doubly degenerate eigenstates exist in the energy range.

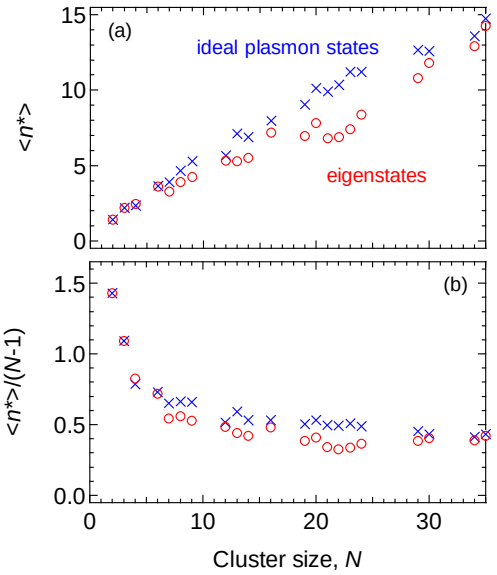

Figure 6.13. (a) The averaged collectivity index $\langle n^* \rangle$ and (b) that normalized by the number of 5s electrons, $N - 1$, as a function of cluster size.

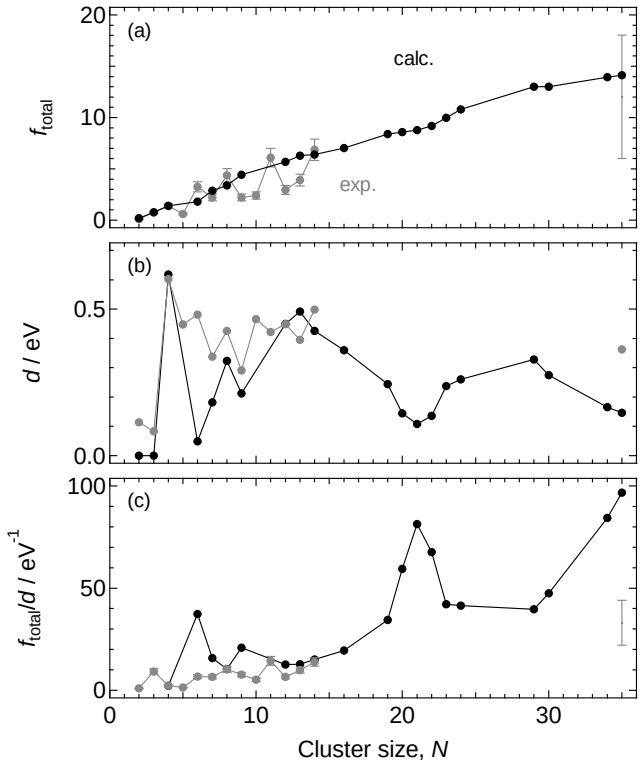

Figure 6.14. The total oscillator strength, f_{total}, the effective spectral width, d, and the density of oscillator strengths, f_{total}/d as a function of cluster size, N. The error bars denote systematic errors in the experiments.

6.6. Collectivity indices and transition densities of ideal plasmon states

Similar to Equation (6.13), one can consider the ideal plasmon state (IPS) [57] as a way to assign a single collectivity index to a group of excited states that constitute a single band at low energy resolution. The ideal plasmon state is defined as the product of the dipole operator and the ground-state wave function $|\Psi_0\rangle$. For example,

$$\left|z\text{-IPS}\right\rangle = \left(-e\right) z \left|\Psi_0\right\rangle = \sum_i \left|\Psi_i\right\rangle\left\langle\Psi_i\right| \left(-e\right) z \left|\Psi_0\right\rangle = \sum_i \mu_{z,i} \left|\Psi_i\right\rangle, \tag{6.15}$$

where $|z\text{-IPS}\rangle$ is the wavefunction of the ideal plasmon state along the z-axis, $|\Psi_0\rangle$ that of the ground state, $|\Psi_i\rangle$ that of the excited eigenstates, and $\mu_{z,i} = \langle\Psi_i|(-e)z|\Psi_0\rangle$ the transition moment. The subscript z indicates the direction; $|x\text{-IPS}\rangle$ and $|y\text{-IPS}\rangle$ are defined by $\mu_{x,i}$ and $\mu_{y,i}$, respectively, in the same way. Although the summation should run over all the exited states in principle, here the ideal plasmon state was constructed by summation over a limited energy range, where transition moments are concentrated to form an absorption band under a low energy resolution. The ideal plasmon state was thus calculated for each absorption band to compare the experimental spectra with theoretical ones.

Since the electron density of a given electronic state is has no nodal plane and each silver atom has the fully-filled d orbitals, the transition density from the ground state $|\Psi_0\rangle$ to the ideal plasmon state becomes a simple function with one nodal plane. In this case, the contribution of orbitals that introduce complicated nodal planes into the transition density in the vicinity of each atom is expected to be small; only contribution of s electrons is anticipated to survive, while that of d electrons are canceled out for the case of silver clusters. The normalization condition $\langle z\text{-IPS}|z\text{-IPS}\rangle = 1$ gives the complete representation of the ideal plasmon state as

$$\left|z\text{-IPS}\right\rangle = \frac{\sum_i \mu_{z,i} \left|\Psi_i\right\rangle}{\sqrt{\sum_i \mu_{z,i}^2}}, \tag{6.16}$$

The transition moment of the ideal plasmon state is

$$\left\langle z\text{-IPS}\middle|z\middle|\Psi_0\right\rangle = \sqrt{\sum_i \mu_{z,i}^2}. \tag{6.17}$$

Because the ideal plasmon state does not have an eigenenergy, the author defines its energy as an expectation value

$$E_{\text{IPS}} = \frac{\sum_i \mu_{z,i}^2 E_i}{\sum_i \mu_{z,i}^2}, \tag{6.18}$$

where E_i is the energy of the i-th excited eigenstate. An oscillator strength of the ideal plasmon state is thus expressed as

$$f_{\text{IPS}} = \frac{8\pi^2 m_{\text{e}}}{3h^2 e^2}\left\langle z\text{-IPS}\middle|z\middle|\Psi_0\right\rangle^2 E_{\text{IPS}} = \frac{8\pi^2 m_{\text{e}}}{3h^2 e^2}\sum_i \mu_{z,i}^2 E_i. \tag{6.19}$$

By substituting the 2018 CODATA recommended values [58, 59],

$$f_{\text{IPS}} = 0.024\sum_i \left(\mu_{z,i}/ea_0\right)^2 \left(E_i/\text{eV}\right), \tag{6.20}$$

where π is the circle ratio, m_{e} the electron mass, h the Plank constant, e the elementary charge, and a_0 the Bohr radius.

Collectivity indices calculated by Equation (6.6) for the ideal plasmon states of each cluster size are listed in Table 6.2. The summation in Equation (6.16) was performed over the same range as listed in Table 6.1. To compare these collectivity indices with those for eigenstates depicted in Figure 6.13 (a), the indices for x-, y-, and z-ideal plasmon states are averaged as follows:

$$\left\langle n^* \right\rangle = \frac{\left(\sum_i \mu_{x,i}^2\right)^2 n_x^* + \left(\sum_i \mu_{y,i}^2\right)^2 n_y^* + \left(\sum_i \mu_{z,i}^2\right)^2 n_z^*}{\left(\sum_i \mu_{x,i}^2\right)^2 + \left(\sum_i \mu_{y,i}^2\right)^2 + \left(\sum_i \mu_{z,i}^2\right)^2}. \quad (6.21)$$

The result is superimposed in Figure 6.13 (a) as blue crosses. Since the ideal plasmon states has the physical meaning of a wave-packet generated at the moment of the pulsed-laser irradiation, the collectivity indices calculated for the ideal plasmon states are expected to reflect the electron dynamics of the system as a measure of the collectivity in the electronic excitations. The collectivity index of the ideal plasmon states show an increasing trend similar to that of the eigenstates. This result is in contrast to ordinary molecules where only two electrons contribute to the excitation [60, 61], which confirms the remarkable optical property, i.e., collective excitation of electrons, in silver clusters. In addition, a normalized collectivity index was calculated, which is defined by the collectivity index of the ideal plasmon states divided by the number of the valence s electrons, $\langle n^* \rangle/(N-1)$; $\langle n^* \rangle/(N-1) = 1$ means that all the s electrons contribute to the ideal plasmon state. The normalized collectivity index thus defined is depicted in Figure 6.13 (b) as a function of cluster size N, which shows no significant size-dependence above $N \sim 12$, where about 40–50% of the valence s electrons are collectivity excited. It would be interesting to compare silver clusters with other metal clusters. Casanova et al. reported for Al_{13}^- cluster that an index called a transition inverse participation ratio, which corresponds to the present collectivity index, is 7.1 for the most intense electron transition at 10.5 eV with an oscillator strength of 3.11 [27], which implies that about 35% of valence electrons contributes to the excitation. The present result indicates that electronic excitations in the UV-VIS energy range in silver cluster cations is as collective as that of Al_{13}^-.

Table 6.2. Information on the ideal plasmon states (IPS) for Ag_N^+ (N = 2–30). The energy ranges, where eigenstates are considered for constructing the ideal plasmon states, are listed in the second column from the left.

N	Range / eV	x-IPS		y-IPS		z-IPS	
		n^*	f_{IPS}	n^*	f_{IPS}	n^*	f_{IPS}
2	3.03	-	0	-	0	1.4	0.18
3	4.01	2.2	0.39	2.2	0.39	-	0
4	3.1–4.8	3.1	0.03	3.3	0.56	2.1	0.80
6	3.5–3.8	-	0	3.0	0.83	4.1	0.97
7	2.9–3.9	3.9	1.43	3.9	1.43	-	0
8	3.7–4.9	5.5	0.81	3.9	1.27	5.2	1.31
9	3.8–4.5	5.3	1.48	5.3	1.49	5.3	1.46
12	3.0–5.0	4.8	2.47	7.0	1.85	7.2	1.37
13	3.1–3.5	6.5	2.12	7.7	2.04	7.3	2.13
14	3.4–5.0	7.8	1.92	6.7	2.10	6.5	2.89
16	3.6–5.0	7.2	2.69	8.0	2.58	10.1	1.76
19	3.6–4.2	8.5	3.06	11.4	2.20	8.5	3.14
20	3.8–4.1	9.9	3.06	9.9	3.06	10.8	2.45
21	3.7–4.4	9.5	3.10	9.9	2.82	10.4	2.84
22	3.8–4.5	9.9	3.20	11.4	2.65	10.0	3.33
23	3.5–4.7	10.7	3.93	11.7	3.19	11.5	2.85
24	3.4–4.8	9.9	4.12	11.6	3.52	12.8	3.16
29	3.5–5.0	11.7	4.87	12.7	4.24	14.2	3.89
30	3.6–4.7	11.4	5.03	12.9	4.25	14.3	3.73

Table 6.2 (cont.) Information on the ideal plasmon states (IPS) for Ag_N^+ (N = 34, 35).

N	Range / eV	x-IPS		y-IPS		z-IPS	
		n^*	f_{IPS}	n^*	f_{IPS}	n^*	f_{IPS}
34	3.7–4.6	15.3	4.43	12.8	4.93	13.0	4.57
35	3.9–4.6	13.8	4.93	14.9	4.81	15.8	4.40

Furthermore, transition densities of the IPSs for $Ag_{19,21,23}^+$ were calculated as shown in Figure 6.15 (a), (b), and (c), respectively. As expected from the Clemenger–Nilsson model (see Figure 4.13 in Chapter 4), $Ag_{21,35}^+$ were spherical: r_x = 4.6 Å, r_y = 4.3 Å, and r_z = 4.2 Å for Ag_{21}^+ from the geometric structure in Figure 6.1 and Equation (4.36). Transition densities of x-, y-, and z-IPS for Ag_{21}^+ are certainly in direction of each axis. Their energies are also close to each other. On the other hand, Ag_{19}^+, which is expected to be oblate from the Clemenger–Nilsson model, has radii of r_x = 4.5 Å, r_y = 3.4 Å, and r_z = 4.8 Å, which resulted in an energy of the y-IPS oscillating along the shorter axis higher than those of the others. Because the excitations at the lower energy are nearly degenerate, its absorption spectrum shows a double-band profile with a weak band at higher energy. For a case of Ag_{29}^+, which is predicted to be prolate by the model, r_x = 5.4 Å, r_y = 4.1 Å, and r_z = 4.2 Å. The situation is opposite to that of Ag_{19}^+; the x-IPS along the longer axis has a lower energy than those of the others. y- and z-IPS are peudo degenerate to result in a more intense band at the higher energy than that of y-IPS. This is a theoretical explanation of the correspondence between geometric structures and spectral profiles found in the present photodissociation-spectroscopic study in Chapter 4.

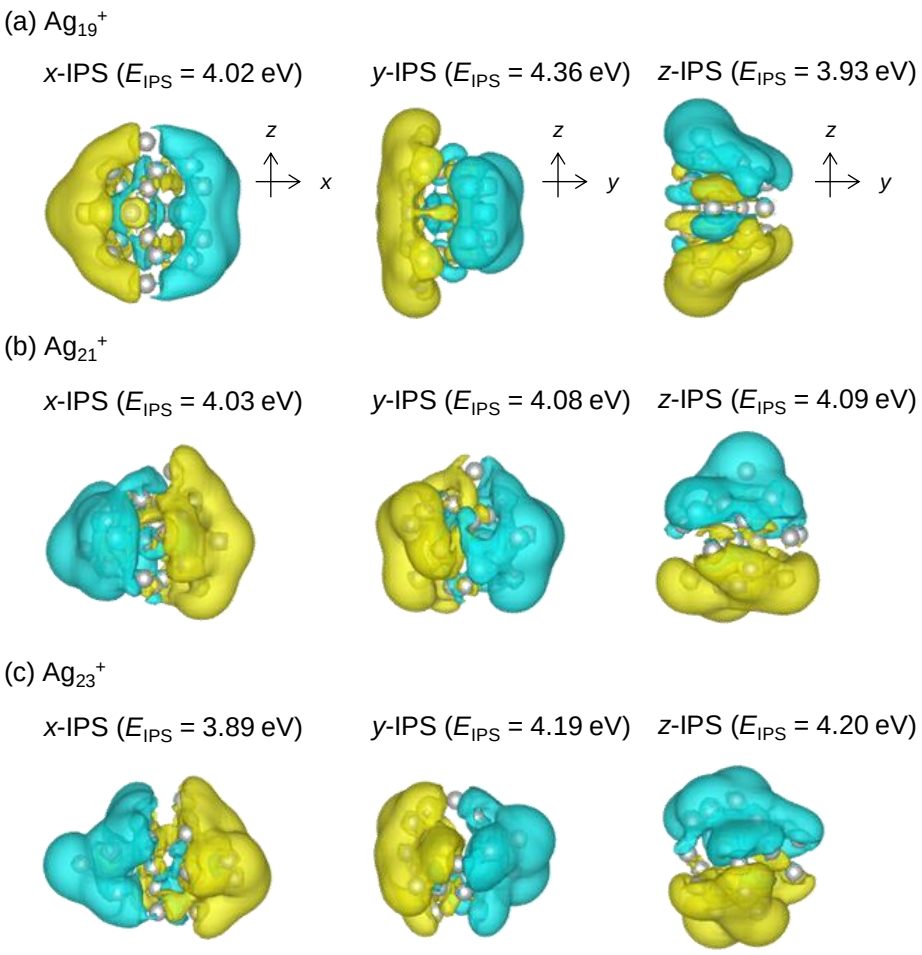

Figure 6.15. The transition densities of ideal plasmon states (IPS) of (a) Ag_{19}^+, (b) Ag_{21}^+, and (c) Ag_{23}^+.

6.7. Summary

A theoretical analysis on the collectivity of electrons in electronic excitations was performed for silver cluster cations, Ag_N^+ (N = 2–40). Firstly, geometric structures of the clusters were obtained by geometry optimization based on the density-functional theory. Secondly, absorption spectra were predicted by the linear-response density-functional theory employing the geometries obtained by the present optimization. The experimental spectra were reproduced by the theoretical predictions for N = 2–14, 19–24, 29, 30, 34, 35 from a point of view of the cross sections, resonance energies, and spectral profiles. Finally, a collectivity index, representing the effective number of individual excitations contributing to excitations, was evaluated by employing ideal plasmon states, which are defined as wave-packet generated at the moment of laser irradiation. The index exhibited an increasing trend as the cluster grows. At larger sizes, the normalized collectivity index revealed that about 40–50% of the valence s electrons are excited collectively. This result indicates the emergence of the collective excitation of electrons in silver cluster cations, which should be contrasted to ordinary molecules where only two electrons contribute to the excitation. Such intense and highly collective excitations were observed in the UV-VIS region (~3–5 eV) is characteristic to silver cluster cations. In addition, transition densities of the ideal plasmon states explained the correspondence between geometric structures of silver cluster cations and spectral profiles found in Chapter 4.

References

[1] C. M. Aikens, S. Li, G. C. Schatz, *J. Phys. Chem. C* **2008**, *112*, 11272.

[2] E. B. Guidez, C. M. Aikens, *Nanoscale* **2014**, *6*, 11512.

[3] C. Yannouleas, R. A. Broglia, M. Brack, P. F. Bortignon, *Phys. Rev. Lett.* **1989**, *63*, 255.

[4] C. Yannouleas, R. A. Broglia, *Phys. Rev. A* **1991**, *44*, 5793.

[5] M. Bernath, C. Yannouleas, R. A. Broglia, *Phys. Lett. A* **1991**, *156*, 307.

[6] C. Yannouleas, E. Vigezzi, *Phys. Rev. B* **1993**, *47*, 9849.

[7] J. Yan, Z. Yuan, S. Gao, *Phys. Rev. Lett.* **2007**, *98*, 216602.

[8] J. Yan and S. Gao, *Phys. Rev. B* **2008**, *78*, 235413.

[9] T. Yasuike, K. Nobusada, M. Hayashi, *Phys. Rev. A* **2011**, *83*, 013201.

[10] E. B. Guidez, C. M. Aikens, *J. Phys. Chem.* C **2013**, *117*, 21466.

[11] E. B. Guidez, C. M. Aikens, *Phys. Chem. Chem. Phys.* **2014**, *16*, 15501.

[12] E. B. Guidez, C. M. Aikens, *J. Phys. Chem. C* **2013**, *117*, 12325.

[13] E. B. Guidez, PhD thesis, Kansas State University (USA), **2014**.

[14] Gaussian 16, Revision A.03, M. J. Frisch, G. W. Trucks, H. B. Schlegel, G. E. Scuseria, M. A. Robb, J. R. Cheeseman, G. Scalmani, V. Barone, G. A. Petersson, H. Nakatsuji, X. Li, M. Caricato, A. V. Marenich, J. Bloino, B. G. Janesko, R. Gomperts, B. Mennucci, H. P. Hratchian, J. V. Ortiz, A. F. Izmaylov, J. L. Sonnenberg, D. Williams-Young, F. Ding, F. Lipparini, F. Egidi, J. Goings, B. Peng, A. Petrone, T. Henderson, D. Ranasinghe, V. G. Zakrzewski, J. Gao, N. Rega, G. Zheng, W. Liang, M. Hada, M. Ehara, K. Toyota, R. Fukuda, J. Hasegawa, M. Ishida, T. Nakajima, Y. Honda, O. Kitao, H. Nakai, T. Vreven, K. Throssell, J. A. Montgomery, Jr., J. E. Peralta, F. Ogliaro, M. J. Bearpark, J. J. Heyd, E. N. Brothers, K. N. Kudin, V. N. Staroverov, T. A. Keith, R. Kobayashi, J.

Normand, K. Raghavachari, A. P. Rendell, J. C. Burant, S. S. Iyengar, J. Tomasi, M. Cossi, J. M. Millam, M. Klene, C. Adamo, R. Cammi, J. W. Ochterski, R. L. Martin, K. Morokuma, O. Farkas, J. B. Foresman, and D. J. Fox, Gaussian, Inc., Wallingford CT, **2016**.

[15] P. Hohenberg, W. Kohn, *Phys. Rev.* **1964**, *136*, B864.

[16] W. Kohn, L. J. Sham, *Phys. Rev.* **1965**, *140*, A1133.

[17] A. D. Becke, *J. Chem. Phys.* **1993**, 98, 5648.

[18] C. Lee, W. Yang, R. G. Parr, *Phys. Rev. B* **1988**, *37*, 785.

[19] P. J. Hay, W. R. Wadt, *J. Chem. Phys.* **1985**, *82*, 299.

[20] M. L. McKee, A. Samokhvalov, *J. Phys. Chem. A* **2017**, *121*, 5018.

[21] M. Chen, J. E. Dyer, K. Ki, D. A. Dixon, *J. Phys. Chem. A* **2013**, *117*, 8298.

[22] M. E. Casida in Recent Advances in Density Functional Methods, Recent Advances in Computational Chemistry Vol. 1, Part II (Ed.: D. P. Chong), World Scientific, Singapore, **1995**, p. 155.

[23] T. Yanai, D. P. Tew, N. C. Handy, *Chem. Phys. Lett.* **2004**, *393*, 51.

[24] A. V. Luzanov, A. A. Sukhorukov, V. É. Umanskii, *Theor. Exp. Chem.* **1976**, *10*, 354.

[25] R. L. Martin, *J. Chem. Phys.* **2003**, *118*, 4775.

[26] A. V. Luzanov, V. É. Umanskii, *Theor. Exp. Chem.* **1977**, *13*, 162.

[27] D. Casanova, J. M. Matxain, J. M. Ugalde, *J. Phys. Chem. C* **2016**, *120*, 12742.

[28] K. Momma and F. Izumi, *J. Appl. Crystallogr.* **2011**, *44*, 1272.

[29] P. Weis, T. Bierweiler, S. Gilb, M. M. Kappes, *Chem. Phys. Lett.* **2002**, *355*, 355.

[30] T. Ito, PhD Thesis, Kyushu University (Japan), **2015**.

[31] T. Ito, Y. Taniguchi, M. Arakawa, A. Terasaki, *Z. Phys. Chem.* **2019**, *233*, 759.

[32] V. Bonačić-Koutecký, L. Češpiva, P. Fantucci, J. Koutecký, *J. Chem. Phys.* **1993**, *98*,

7981.

[33] V. Bonačić-Koutecký, J. Pittner, M. Boiron, P. Fantucci, *J. Chem. Phys.* **1999**, *110*, 3876.

[34] A. Shayeghi, R. L. Johnston, D. M. Rayner, R. Schäfer, A. Fielicke, *Angew. Chem., Int. Ed.* **2015**, *54*, 10675.

[35] J. van der Tol, D. Jia, Y. Li, V. Chernyy, J. M. Bakker, M. T. Nguyen, P. Lievens, E. Janssens, *Phys. Chem. Chem. Phys.* **2017**, *19*, 19360.

[36] E. M. Fernández, J. M. Soler, I. L. Garzón, L. C. Balbás, *Phys. Rev. B* **2004**, *70*, 165403.

[37] A. Shayeghi, R. L. Johnston, R. Schäfer, *Phys. Chem. Chem. Phys.* **2013**, *15*, 19715.

[38] P. Weis, O. Welz, E. Vollmer, M. M. Kappes, *J. Chem. Phys.* **2004**, *120*, 677.

[39] D. Schooss, S. Gilb, J. Kaller, M. M. Kappes, F. Furche, A. Köhn, K. May, R. Ahlrichs, *J. Chem. Phys.* **2000**, *113*, 5361.

[40] A. Terasaki, S. Minemoto, M. Iseda, T. Kondow, *Eur. Phys. J. D* **1999**, *9*, 163.

[41] A. Terasaki, *J. Phys. Chem. A* **2007**, *111*, 7671.

[42] M. N. Blom, D. Schooss, J. Stairs, M. M. Kappes, *J. Chem. Phys.* **2006**, *124*, 244308.

[43] X. Xing, R. M. Danell, I. L. Garzón, K. Michaelian, M. N. Blom, M. M. Burns, J. H. Parks, *Phys. Rev. B* **2005**, *72*, 081405.

[44] C. Ellert, M. Schmidt, T. Reiners, H. Haberland, *Z. Phys. D* **1997**, *39*, 317.

[45] V. Bonačić-Koutecký, M. Boiron, J. Pittner, P. Fantucci, J. Koutecký, *Eur. Phys. J. D* **1999**, *9*, 183.

[46] M. Couty, M. B. Hall, *J. Comp. Chem.* **1996**, *17*, 1359.

[47] S. Krückeberg, G. Dietrich, K. Lüzenkirchen, L. Schweikhard, C. Walther, J. Ziegler, *J. Chem. Phys.* **1999**, *110*, 7216.

[48] M. Harb, F. Rabilloud, D. Simon, A. Rydlo, S. Lecoultre, F. Conus, V. Rodrigues, C. Félix, *J. Chem. Phys.* **2008**, *129*, 194108.

[49] F. Rabilloud, *J. Chem. Phys.* **2014**, *141*, 144302.

[50] R. Schira, F. Rabilloud, *J. Phys. Chem. C* **2018**, *122*, 27656.

[51] F. Rabilloud, *Eur. Phys. J. D* **2013**, *67*, 18.

[52] C. Yu, R. Schira, H. Brune, B. von Issendorff, F. Rabilloud, W. Harbich, *Nanoscale* **2018**, *10*, 20821.

[53] B. Anak, M. Bencharif, F. Rabilloud, *RSC Adv.* **2014**, *4*, 13001.

[54] M. Harb, F. Rabilloud, D. Simon, *Chem. Phys. Lett.* **2009**, *476*, 186.

[55] F. Rabilloud, *J. Phys. Chem. A* **2013**, *117*, 4267.

[56] R. Schira, F. Rabilloud, *J. Phys. Chem.* **2019**, *123*, 6205.

[57] T. Yasuike, private communication.

[58] E. Tiesinga, P. J. Mohr, D. B. Newell, B. N. Taylor, *Rev. Mod. Phys.* **2021**, *93*, 025010.

[59] E. Tiesinga, P. J. Mohr, D. B. Newell, B. N. Taylor, *J. Phys. Chem. Ref. Data*, **2021**, *50*, 033105.

[60] A. Dreuw, M. Head-Gordon, *Chem. Rev.* **2005**, *105*, 4009.

[61] E. R. Batista, R. L. Martin, *J. Phys. Chem. A* **2005**, *109*, 3128.

7. Concluding Remarks

In the present study, geometric structures and electronic excitations of silver cluster cations, Ag_N^+, were investigated by photodissociation action spectroscopy, cavity ring-down spectroscopy, and theoretical analysis based on density-functional and linear-response density-functional theories.

The experimental setup was described in Chapter 2. Silver cluster cations were generated, size-selected, stored, and irradiated by a pulsed laser. In photodissociation spectroscopy, dissociation yields are measured to obtain photodissociation spectra. In cavity ring-down spectroscopy, a pair of high-reflectivity mirrors were placed in such that the ion trap was enclosed in a Fabry−Perot optical cavity. A photoabsorption cross section is obtained from the exponential decay of the output laser pulse from the cavity.

Prior to the spectroscopic studies, the cluster-growth process in a magnetron-sputtering cluster-ion source was investigated for optimizing operation conditions to generate cluster sizes of interest efficiently as described in Chapter 3. Optical emission spectroscopy was employed in combination with mass spectrometry; light emission from plasma generated in the magnetron was analyzed to obtain emission spectra as a function of discharge power of the magnetron, while mass spectra of the generated clusters were measured at the same time. The number of sputtered silver atoms was evaluated from the intensity of the emission spectra for comparison with the average cluster size, which is expected to be proportional to the density of the sputtered atoms based on a statistical model proposed in the present study. As a result of the analysis, it was implied that the effective volume of the cluster-growth region was enlarged at higher discharge power, which leads to rarefaction of the sputtered atoms and suppression of cluster growth.

Moreover, the mass spectra were reproduced by multiple Poisson distributions with several different average sizes rather than a single distribution. This is consistent with the well-known inhomogeneous density profile of the sputtered atoms; larger clusters are supposed to be generated in a high-density region and vice versa. The insight into the cluster-growth process gained in the present study proposes a possibility to enhance intensity of even larger clusters, e.g., by preventing rarefaction of sputtered atoms by decreasing their kinetic energies by collision with a buffer gas. This cluster-growth analysis was important for covering the very broad size range up to $N = 92$ as studied in the present experiments.

In Chapter 4, photodissociation action spectroscopy was performed on size-selected free silver cluster cations by employing an ion trap. This is the first systematic study covering almost every size of the clusters up to $N = 92$. The action spectra showed multi-modal profiles at $N \leq 14$, while almost all of the clusters with sizes above 19 exhibited single- or double-band profiles in a specific spectral range. Such a trend in spectral profiles and condensed features of absorption bands indicate emergence of collective excitations of electrons in silver cluster cations above $N = 19$. Especially, the single- or double-band profiles were interpreted by geometries of the clusters; spherical clusters are expected to show three-fold degenerate collective excitation modes, which results in a single-band profile. On the other hand, the degeneracy is lifted in prolate clusters to generate two types of excitations: two-fold degenerate collective excitation along the shorter axis and a single collective excitation along the longer axis. Such a change in the geometry is consistent with the prediction based on the Clemenger–Nilsson model up to $N = 46$, while the geometries of the larger clusters could not be explained by the model because the packing effect becomes dominant in the larger clusters.

Geometric structures of larger clusters with $N \geq 47$ were predicted from the present spectral profiles; such a systematic study on geometric structures of silver cluster cations were performed for the first time. Moreover, the redshift of the absorption band from N = 55 to 92 was observed. These trends are in line with collective excitation of electrons in nanoparticles/nanorods. The result presented in Chapter 4 implies emergence of collective excitation of electrons in silver cluster cations above N = 19. However, photodissociation cross sections were not measured for larger clusters with $N \geq 19$ because of multi-photon dissociation processes. It is necessary to measure the absorption cross sections without relying on photodissociation.

In this context, cavity ring-down spectroscopy was performed in Chapter 5. Photoabsorption (instead of photodissociation) spectra of Ag_N^+ (N = 3, 4, 8, 9, 35, 40, 45, 50, 55, 60, 65, 70, 71, 81, and 92) were presented for the first time after previous reports limited to N = 2 and 9. To obtain quantitative absorption cross sections, the density profile of the trapped ions was measured prior to the spectroscopic experiment. Cavity mirrors were arranged carefully to maximize overlap between the spatial distribution of the trapped ions and the cavity mode of the laser. To characterize concentration of oscillator strengths, the density of oscillator strengths in an effective spectral region was evaluated as a function of cluster size. The density of oscillator strengths thus evaluated showed an increasing trend, which implies oscillator strengths are concentrated as the cluster grows.

Finally, the collectivity in silver cluster cations was analyzed theoretically as described in Chapter 6. The present calculation consists of three steps: geometry optimization based on the density-functional theory, spectral simulation based on the linear-response density-functional theory, and evaluation of collectivity indices that

represent the effective number of individual excitations contributing to the eigenstates in the Casida equation. The experimental spectra were reproduced by the calculation for N = 2–14, 19–24, 29, 30, 34, and 35 in the aspects of cross sections, resonance energies, and spectral profiles. To calculate collectivity indices for excited states generated upon a pulsed excitation, ideal plasmon states were constructed, which carries all the transition moments of which eigenstates contribute to the excitation. Collectivity indices of the ideal plasmon states showed an increasing trend. Especially, it was elucidated that about 40–50% of valence electrons contribute to the excitations at larger sizes, which was regarded as emergence of collectivity in electronic excitations.

In this thesis, a systematic and extensive study was presented on geometric structures and electronic excitations of size-selected free silver cluster cations. Based on the present experimental and theoretical results, the author concludes that silver cluster cations show collective excitations in electrons above N = 19. The collective excitation modes manifested in the spectral profiles are associated with geometric structures of the clusters in the same way as plasmonic excitation in nanoparticles/nanorods. Due to limitation of photodissociation spectroscopy and lack data of photoabsorption spectra, N = 15, 17 and 18 might also show the collective excitation. Additional cavity ring-down measurements are demanded for these sizes. In addition, there are still open questions about mechanisms of collective excitation. For example, gold nanoparticles consisting of more than hundreds of atoms are known to exhibit plasmonic excitation, while it is theoretically predicted that the plasmonic excitation loses its dipole moment by strong coupling with d-electron excitations as reported for the gold octamer [T. Yasuike et al., *Phys. Chem. Chem. Phys.* **2013**, *15*, 5424]; it remains to be elucidated how such d-electron coupling is reduced as a small cluster grows toward a nanoparticle. In addition,

there is no systematic experimental study on photoabsorption of free gold clusters although ligand-protected ones have been studied well. In this context, the present methodology provides us with an opportunity of size-dependence studies on oscillator strengths experimentally and on collectivity theoretically; the analysis of the d-electron coupling described above is applicable as well to exploring size-dependent effects of d electrons. Not only gold but also copper and even aluminum clusters would be of great interest for future studies. The author believes that the present study paves the way to elucidate the origin of electronic excitations in metal clusters and to bridge the gap between molecular/cluster science and nanoscience.

List of Publications

[1] **S. Kono**, M. Arakawa, A. Terasaki

Analysis of Cluster Growth in Magnetron-sputtering Metal-cluster Source by Optical Emission Spectroscopy

Chem. Lett. **2019**, *48*, 1537.

[2] **S. Kono**, T. Ito, M. Arakawa, T. Horio, A. Terasaki

Photodissociation of Silver Cluster Cations in an Ion Trap: One-photon vs. Multi-Photon Processes Studied by Experiment and Statistical RRK Theory

Manuscript in preparation

[3] **S. Kono**, S. Kawamura, S. Fujimoto, Y. Kiyomura, K. Tobita, T. Ito, M. Arakawa, T. Horio, T. Yasuike, A. Terasaki

Evolution of Geometric Structures of Silver Cluster Cations Investigated by Photodissociation Action Spectroscopy and Theoretical Calculations

Manuscript in preparation

[4] **S. Kono**, S. Kawamura, S. Fujimoto, Y. Kiyomura, K. Tobita, M. Arakawa, T. Horio, T. Yasuike, A. Terasaki

Emergence of Collective Excitation of Electrons in Silver Cluster Cations: Quantitative Measurement of Oscillator Strengths by Cavity Ring-Down Optical Absorption Spectroscopy and Theoretical Analysis on Collectivity

Manuscript in preparation

[5] M. Arakawa, D. Okada, **S. Kono**, A. Terasaki

Preadsorption Effect of Carbon Monoxide on Reactivity of Cobalt Cluster Cations toward Hydrogen

J. Phys. Chem. A **2020**, *124*, 9751. **(Not part of the Thesis)**

[6] T. Hayakawa, M. Arakawa, **S. Kono**, T. Handa, N. Hayashi, K. Minamikawa, T. Horio, A. Terasaki

X-ray absorption spectroscopy of small copper-oxide cluster ions for analyses of Cu oxidation state and Ar complexation: $CuOAr^+$ and $Cu_2O_2^+$

Z. Phys. Chem. **2021**, *235*, 213. **(Not part of the Thesis)**

[7] S. Kawamura, M. Yamaguchi, **S. Kono**, M. Arakawa, T. Yasuike, T. Horio, A. Terasaki

Photodestruction Action Spectroscopy of Silver Cluster Anions, Ag_N^- (N = 3–19), with a Linear Ion Trap: Observation of Bound Excited States above the Photodetachment Threshold

J. Phys. Chem. A **2023**, *127*, 6063. **(Not part of the Thesis)**

[8] M. Arakawa, **S. Kono**, Y. Sekine, A. Terasaki

Reaction of Size-Selected Iron-Oxide Cluster Cations with Methane: A Model Study of Rapid Methane Loss in the Mars' Atmosphere

Manuscript in preparation **(Not part of the Thesis)**

Acknowledgements

I would like to thank my supervisor, Professor Akira Terasaki (Kyushu University), for his support on my research. Since I joined his laboratory, he has been giving me advice on my study. The advice from the specialist of spectroscopy as well as cluster science was great help to propel my research. He also taught me about an attitude toward research that a scientist should have. All of his words are treasure for me. In addition, thankfully, he was patiently waiting until I overcame obstacles in my study and my life when I got stuck. I don't have a vocabulary enough to express my gratitude to him. My study would not have been finished without his help.

Dr. Takuya Horio (Associate Professor at Kyushu University) gave me advice on my study as well. In addition, I learned an attitude toward science from him; significance in the research, a plan of experiments organized to the goal, etc. Discussion with him was really valuable; I gained a deep insight into chemical processes especially relevant to my study such as photodissociation and internal conversion. His preparation of the cavity mirrors helped my study to reveal the entire spectral shapes for the larger clusters. I would like to express my heartfelt gratitude to him.

Dr. Masashi Arakawa (Assistant Professor at Kyushu University) has been my dear neighbor in this laboratory for a long time. I would like to thank him for preparation of necessaries in my experiments and troubleshooting my setup, which helped perform the experiments smoothly. His mental support as well as scientific advice assisted me very much; I would not graduate without him.

Professor Tomokazu Yasuike (The Open University of Japan) helped my study from a theoretical point of view. His knowledge specialized in the theoretical background of the collective excitation of electrons helped me greatly understand and

investigate the optical processes presented in this thesis. Thankfully, he patiently supported me and reviewed the manuscript of this thesis between his hard work. I would like to acknowledge his favor.

I also would like to thank Professor Haruyuki Nakano and Associate Professor Kazuhiko Ohashi for reviewing my thesis.

I would like to express my sincere appreciation to the former and current members of the Quantum Chemistry Laboratory in Kyushu University. Especially, initiation of my research by Mr. Shuhei Fujimoto and experiments with him are my precious memories. He taught me how to operate the experiments and attentiveness to the experiments, which formed my attitude to science. Sometimes the experiments were performed overnight, but I never minded because we did pretty good jobs thanks to him. He pleasantly discussed with me even after he graduated. I really thanks to his favor. Mr. Shun Kawamura and Mr. Kensuke Morishita supported my study; their patient work was essential to finish my research. Dr. Kota Ando (currently at SPring-8/JASRI) is also essential to my life in the laboratory because he inspired me to join this laboratory and go to the doctoral course. Several years have passed since his graduation, but he still gives advice to me when I wish to consult him thankfully. Mr. Takuya Yoshioka supported me as well; I would not overcome difficulties in my life without his support. Mrs. Tamami Kawai and Mrs. Setsuko Shigematsu, former and present secretaries of this laboratory, respectively, supported me in office work. I would like to thank all the other colleagues in this laboratory.

Dr. Tetsuichiro Hayakawa (Toyota Central R&D Labs., Inc.) also taught me a stance to science. In the collaborate research with him, I learned importance of planning experiments especially operated in limited time and carefulness during the experiments.

He also cheered me when I was in trouble. I will never forget all things what he taught me.

Finally, I would like to express my heartfelt appreciation to my family for supporting me financially and mentally.

This work was supported by JSPS KAKENHI Grant Numbers JP18H03901, JP21J12060, and JP22H00317. The computation was carried out using the computer resource offered under the category of General Projects by Research Institute for Information Technology, Kyushu University.